Universiteit Antwerpen

Faculteit Wetenschappen

Departement Fysica

First-principles electronic structure calculations of $Cu(In,Ga)Se_2$ photovoltaic absorber materials

Jonas Bekaert

Promotor: Prof. Dr. B. Partoens
Copromotor: Dr. R. Saniz Balderrama

Proefschrift ter verkrijging van de graad van Master in de Fysica

Academiejaar 2012-2013

Abstract - English

The chalcopyrite material $Cu(In,Ga)Se_2$ is a direct band gap semiconductor with associated high optical absorption. As a result, $Cu(In,Ga)Se_2$ absorber layers are used in thin film photovoltaic cells. Cells based on polycrystalline $Cu(In,Ga)Se_2$ hold to date the record efficiency in this category. In this thesis, $Cu(In,Ga)Se_2$ is studied in the framework of density functional theory. The Perdew-Burke-Ernzerhof exchange-correlation functional, widely used in density functional theory, turns out to be insufficient, due to the band gap problem in density functional theory. We find that the Heyd-Scuseria-Ernzerhof functional, which includes an amount of exchange from the Hartree-Fock method, yields much better agreement with the experimental band gaps. First, the main characteristics of the crystal structure and electronic structure of $Cu(In,Ga)Se_2$ compounds are discussed. In this discussion, the varying Ga-to-In ratio of the compounds plays a prominent role. For instance, the band gap of $Cu(In,Ga)Se_2$, ranging between 1.0 and 1.7 eV, is determined by this ratio. Regarding alloying properties of the compound, we do not find a tendency for phase segregation at room temperature. We also study the mutual band alignment of $Cu(In,Ga)Se_2$ materials, comparing two essentially different methods. On one hand, the alignment is performed based on the calculation of the branch-point energy, for which only the bulk band structure is needed. It is compared to the alignment with respect to the vacuum level, obtained from a calculation on a slab. We demonstrate that the band alignments that follow from these two methods are consistent. We furthermore review electrical conductivity of $Cu(In,Ga)Se_2$ materials due to lattice defects, important for the application in photovoltaic cells. For this purpose, the formation energy of a selection of point defects is calculated, both intrinsic defects and Na and C impurities. Spurious interaction between point defects is minimized by selecting sufficiently large supercells. We can identify intrinsic Cu vacancy defects as plausibly the main contribution to p-type conductivity in $Cu(In,Ga)Se_2$ compounds. We also show that the formation of $NaInSe_2$ does not result in an effective hole barrier at the grain boundaries, contrary to what has previously been assumed. Finally, we have found that C defects do not easily form in $Cu(In,Ga)Se_2$. As a result, we expect that C is expelled from the absorber, thus not affecting the electrical conductivity. This is relevant in view of novel nonvacuum growth methods.

Abstract - Nederlands

Het chalcopyriet-materiaal Cu(In,Ga)Se_2 is een halfgeleider met een directe bandkloof, gekenmerkt door sterke optische absorptie. Hierom wordt Cu(In,Ga)Se_2 als absorptiemateriaal in dunne-film fotovoltaïsche cellen gebruikt. Het blijkt dat cellen die polykristallijn Cu(In,Ga)Se_2 bevatten, de hoogste efficiëntie hebben binnen de categorie van dunne-film cellen. In deze thesis wordt Cu(In,Ga)Se_2 bestudeerd gebruik makend van dichtheidsfunctionaaltheorie. De courante Perdew-Burke-Ernzerhof exchange-correlatiefunctionaal is ontoereikend, omwille van het bandkloofprobleem. De Heyd-Scuseria-Ernzerhof functionaal, die een hoeveelheid Hartree-Fock exchange-interactie bevat, leidt tot een veel betere overeenkomst met de experimentele bandkloven. Om te beginnen worden de belangrijkste eigenschappen van de kristalstructuur en de elektronische structuur van Cu(In,Ga)Se_2 besproken. Hierin speelt de variabele Ga-In verhouding een belangrijke rol. De bandkloof van Cu(In,Ga)Se_2, die varieert tussen 1.0 en 1.7 eV, hangt bijvoorbeeld van deze verhouding af. Wat de eigenschappen van de legering betreft, treedt er volgens onze berekeningen geen fasesegregatie op bij kamertemperatuur. We bestuderen ook de alignering van de banden van Cu(In,Ga)Se_2 materialen, waarbij we twee essentieel verschillende methoden vergelijken. Enerzijds wordt er een alignering uitgevoerd die gebaseerd is op de 'branch-point' energie. Deze kan berekend worden uit louter de bandenstructuur in bulk. We vergelijken met een alignering ten opzichte van het vacuüumniveau, verkregen uit een berekening met een 'slab' (plaat). Het blijkt dat de aligneringen via de twee verschillende methoden consistent zijn. Verder bekijken we de elektrische geleiding in Cu(In,Ga)Se_2 ten gevolge van roosterdefecten, die erg van belang is voor toepassingen in fotovoltaïsche cellen. Hiertoe wordt de vormingsenergie van een reeks van puntdefecten, zowel intrinsieke defecten als Na- en C-onzuiverheden, berekend. Ongewenste interactie tussen deze puntdefecten wordt geminimaliseerd door het gebruik van voldoende grote supercellen. Zo kunnen we intrinsieke Cu-vacatures identificeren als waarschijnlijk de hoofdoorzaak van p-type geleiding in Cu(In,Ga)Se_2 materialen. We tonen ook aan dat de vorming van $NaInSe_2$ aan de korrelgrenzen niet leidt tot een effectieve barrière voor gaten, in tegenstelling tot wat in sommige publicaties wordt gesteld. Ten slotte hebben we ontdekt dat C-defecten niet eenvoudig tot stand komen in Cu(In,Ga)Se_2. Daarom verwachten we dat C uit de absorptielaag gestoten wordt en dus de elektrische geleiding niet beïnvloedt. Dit is relevant met het oog op nieuwe groeitechnieken voor Cu(In,Ga)Se_2 die geen vacuümcondities behoeven.

Acknowledgement

In the first place, I would like to express my gratitude to my promotor Prof. Bart Partoens and my copromotor Dr. Rolando Saniz for their help and advice. I highly value their guidance through the entire process, from the selection of the topic to the final revision of the text, and all fruitful discussions along the way. I would also like to thank the Condensed Matter Theory (CMT) research group as a whole. I have thoroughly enjoyed being part of the group and I appreciate the help I received from various members. Among them, I want to thank Stephan Vercauteren in particular for his help in technical matters and for stimulating talks. I would also like to acknowledge Prof. Susanne Siebentritt of the University of Luxembourg for her visit on June 13 (2013), which gave me an opportunity to talk through my results with an expert in the field of photovoltaics. Furthermore, the computational infrastructure I could use, has equally been essential to carry out my research. This includes the computer cluster 'Seastar', hosted by CMT and the computer cluster 'Turing', hosted by CalcUA, a division of the Flemish Supercomputer Centre VSC, supported financially by the Hercules foundation and the Flemish Government (EWI Department). I want to thank all that are involved. Additionally, I have been thrilled to run calculations on the new tier-1 computer cluster nicknamed 'Muk', also hosted by VSC. It is a true supercomputer that, since its launch in the fall of 2012, has occupied a place on the Top500 list of supercomputers around the world. Finally, I am grateful to my parents, as they have enabled me to pursue the career of my choice, in physics.

Preface

This Master thesis bundles the research I have carried out as part of the Master in Physics program at the University of Antwerp, mainly in the academic year 2012-2013. The research is situated in the field of theoretical and computational solid state physics. It is focused on a first-principles study of the photovoltaic absorber material Cu(In,Ga)Se_2, generally abbreviated as 'CIGS'. In particular, the electronic structure of CIGS is discussed, both in pure form and containing point defects.

In Chapter 1, the space symmetry of CIGS, the chalcopyrite structure, is introduced; this is followed by an overview of the application of CIGS in photovoltaic cells and of growth methods for CIGS layers. At the end of Chapter 1, the goal of this thesis is formulated in more detail. Chapter 2 treats the method used for the electronic structure calculations in this thesis, namely density functional theory (DFT). The discussion starts from the general quantum mechanical many-body problem and leads all the way to the practical implementation of DFT and the software package VASP. Chapter 2 also incorporates post-DFT methods, notably the hybrid method that mixes Hartree-Fock exchange interaction into DFT to correct for the band gap problem. The hybrid method is widely used in this thesis. Then, in Chapter 3, the methods for electronic structure calculations are applied to CIGS. This leads to a wide discussion of the structural and electronic properties of pure CIGS, stressing the effect of the varying Ga-to-In ratio. At the end of Chapter 3, optical properties of CIGS are also discussed, based on the dielectric function. The study of the band structures of pure CIGS is deepened in Chapter 4, where the band alignment of CIGS compounds is reviewed. Subsequently, in Chapter 5 the effect of lattice defects is studied. This comprises both intrinsic defects (Cu vacancies) and doping (with Na and C). At the end of the thesis, a conclusion and outlook in both English and Dutch is offered, followed by the bibliography.

Throughout the thesis mostly the electronvolt (eV) is used as the unit of energy and the Ångström (Å) is used as the unit of distance. The reason is that these comply well with the atomic and electronic scale. In Chapter 2 however, atomic units are selected to simplify the appearance of the equations. Furthermore, for vectors the convention is adopted that they are printed in bold, while operators are indicated by a hat.

I hope the reader will find this thesis interesting and enjoyable.

Jonas Bekaert
August 2013, Wilrijk.

Contents

Abbreviations

AM	air mass
BO	Born-Oppenheimer
BPE	branch-point energy
BZ	Brillouin Zone
CBM	conduction band minimum
CGA	conjugate gradient algorithm
CGS	$CuGaSe_2$
CIGS	$Cu(In,Ga)Se_2$
CIS	$CuInSe_2$
DFT	density functional theory
DOS	density of states
FF	fill factor
GB	grain barrier
GGA	generalized gradient approximation
GI	grain interior
HF	Hartree-Fock
HK	Hohenberg-Kohn
HSE	Heyd-Scuseria-Ernzerhof
IBZ	irreducible Brillouin zone
KS	Kohn-Sham
LDA	local density approximation
NIS	$NaInSe_2$
PAW	projector augmented wave
PBE	Perdew-Burke-Ernzerhof
PDOS	projected density of states

PP	pseudopotential
PV	photovoltaic
SC	self-consistent
SEM	scanning electron microscopy
SOC	spin-orbit coupling
VASP	Vienna Ab-initio Simulation Package
VBM	valence band maximum
XC	exchange-correlation

Chapter 1

Introduction to CIGS and CIGS photovoltaic cells

1.1 CIGS: a chalcopyrite semiconductor material

$Cu(In,Ga)Se_2$ or equivalently $CuIn_{1-x}Ga_xSe_2$ (CIGS) is a I-III-VI_2 semiconductor compound, where $0 \leq x \leq 1$ denotes the relative amount of Ga. It can thus be considered a solid solution of $CuInSe_2$ (CIS, x=0) and $CuGaSe_2$ (CGS, x=1). They adopt the chalcopyrite structure ABX_2 with body-centered tetragonal (BCT) space group $I\bar{4}2d$ (No. 122) [1]. This space group is non-symmorphic (since a d-glide plane is present in the symbol) and non-centrosymmetric. In the chemical formula ABX_2 of the chalcopyrite structure, A (copper: Cu) and B (indium: In and gallium: Ga) are the cations and X (selenium: Se) the anions. The conventional unit cell of the chalcopyrite structure is shown in Figure 1.1. It is body-centered tetragonal and contains 16 atoms. All atoms in the chalcopyrite structure have tetrahedral coordination. Other chalcopyrite materials include $CuIn_{1-x}Ga_xS_2$.

The chalcopyrite structure derives from the diamond cubic structure, following the *Grimm-Sommerfeld rule*. This rule states that the average number of valence electrons per atom must be 4 to achieve tetrahedral bonding [2]. The diamond cubic structure of e.g. Si is a combination of 2 face-centered cubic lattices. If these lattices are filled with a different type of atom, the zincblende structure is obtained. An example of the zincblende structure is the II-VI binary compound ZnS, where Zn is the cation and S the

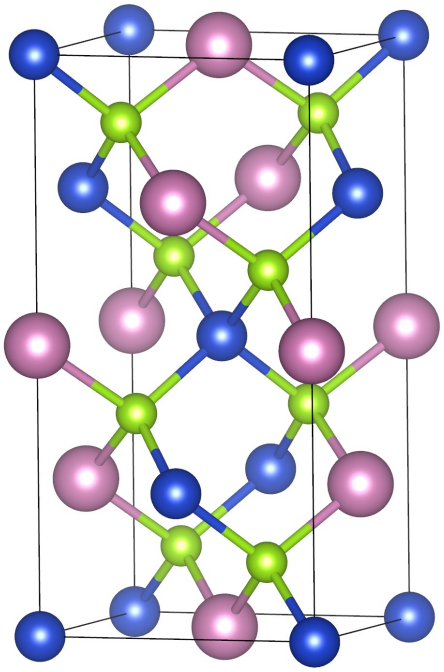

FIGURE 1.1: *The conventional unit cell of the chalcopyrite structure, specifically* $CuInSe_2$*, which contains 4 Cu atoms (blue), 4 In atoms (pink) and 8 Se atoms (green). The Cu-Se and In-Se bonds are shown schematically.*

anion. Replacing half of the cations in the zincblende structure by cation A (e.g. Cu) and the others by B (e.g. In) in the fashion shown in Figure 1.1, yields the chalcopyrite structure. The cubic symmetry of the zincblende structure is lost in CIGS due to tetragonal distortion. This is expressed by the *tetragonal distortion parameter* $\eta = \frac{c}{2a} \neq 1$, where a and c are the lattice parameters. The tetragonal distortion parameter denotes to which extent the tetragonal structure is deformed w.r.t. the related zincblende structure. A set of primitive lattice vectors can be constructed as follows:

$$\begin{cases} \mathbf{a}_1 = a \cdot (1,0,0) \\ \mathbf{a}_2 = a \cdot (0,1,0) \\ \mathbf{a}_3 = a \cdot \left(\frac{1}{2}, \frac{1}{2}, \eta\right) \ . \end{cases} \tag{1.1}$$

The volume of the primitive unit cell is $\frac{a^2 c}{2}$ and it contains 8 atoms, while the conventional unit cell contains 16 atoms. The Cartesian coordinates of the atoms in the general ABX_2 chalcopyrite structure are summed up in Table 1.1 [3] [1]. The anions are characterized by a degree of freedom, called the *anion displacement* u.

[1] The article by J. E. Jaffe and A. Zunger we refer to contains an error, namely in the Cartesian coordinates presented in this article u should be replaced by $u - \frac{1}{4}$.

Atom	Cartesian coordinate
A_1	$0, 0, 0$
A_2	$0, \frac{a}{2}, \frac{c}{4}$
B_1	$\frac{a}{2}, \frac{a}{2}, 0$
B_2	$\frac{a}{2}, 0, \frac{c}{4}$
X_1	$ua, \frac{a}{4}, \frac{c}{8}$
X_2	$(1-u)a, \frac{3a}{4}, \frac{c}{8}$
X_3	$\frac{a}{4}, (\frac{1}{2}+u)a, \frac{3c}{8}$
X_4	$\frac{3a}{4}, (\frac{1}{2}-u)a, \frac{3c}{8}$

TABLE 1.1: *The Cartesian coordinates of the atoms in the chalcopyrite primitive unit cell.*

In CIGS, the cation 'A' is Cu and cation 'B' is either In or Ga, while the anion 'X' is Se. Formally, in the chemical bonds in CIGS, Cu carries oxidation +1, In and Ga oxidation +3 and Se -2. In Chapter 3, Section 3.3.3, we present an extensive analysis of the character of the chemical bonds in $CuIn_{1-x}Ga_xSe_2$.

From the Cartesian coordinates, applying elementary geometry, the nearest neighbor distances R_{AX} and R_{BX} can be calculated to be:

$$R_{\mathrm{AX}} = a \cdot \left[u^2 + (1+\eta^2)/16\right]^{\frac{1}{2}} \tag{1.2}$$

and

$$R_{\mathrm{BX}} = a \cdot \left[\left(u - \frac{1}{2}\right)^2 + (1+\eta^2)/16\right]^{\frac{1}{2}} . \tag{1.3}$$

The so-called *bond mismatch* is:

$$R_{\mathrm{AX}}^2 - R_{\mathrm{BX}}^2 = a^2 \cdot \left(u - \frac{1}{4}\right) . \tag{1.4}$$

The mismatch vanishes for $u = \frac{1}{4}$; if in addition $\eta = 1$ and atoms A and B are the same element, the zincblende structure is retrieved.

1.2 CIGS photovoltaic cells

The principal application of CIGS materials is situated in the field of photovoltaic (PV) devices, where it is used as an absorber material. We will start this section by reviewing the fundamentals of PV devices. Subsequently, we focus on CIGS PV cells, more specifically the cell composition and functioning and common deposition methods for the CIGS layer. The relevance of these subjects for our theoretical study is natural. The topics that are investigated in this thesis are often inspired by the photovoltaic practice and a comparison to experimental data is made whenever possible.

1.2.1 Fundamentals of photovoltaic devices

Excellent references we have consulted for this section and advise for further reading are [4, 5]. On a fundamental level, every PV device functions based on the following subsequent steps:

I. A light absorption process in the absorber material causes a transition to an excited state.

II. The excited state is converted to a free pair of opposite charge carriers (in practice electrons and holes).

III. A discriminating transport mechanism forces the opposite charge carriers to move in different directions, namely the negative charge carrier to the cathode and the positive charge carrier to the anode.

IV. After work has been done at the load, the charge carrier pair returns to the ground state by recombining.

The first step is (usually) achieved in a semiconductor material. In a metal immediate recombination due to thermal relaxation occurs, while in an insulator the excitation requires an excessive amount of energy. The distinction between steps I and II is to be made in case initially an exciton (a *bound* charge carrier pair) is generated. The conversion of the exciton to a free pair is in practice produced by the mechanism behind step III, that 'pulls apart' the exciton. This discriminating transport mechanism can be

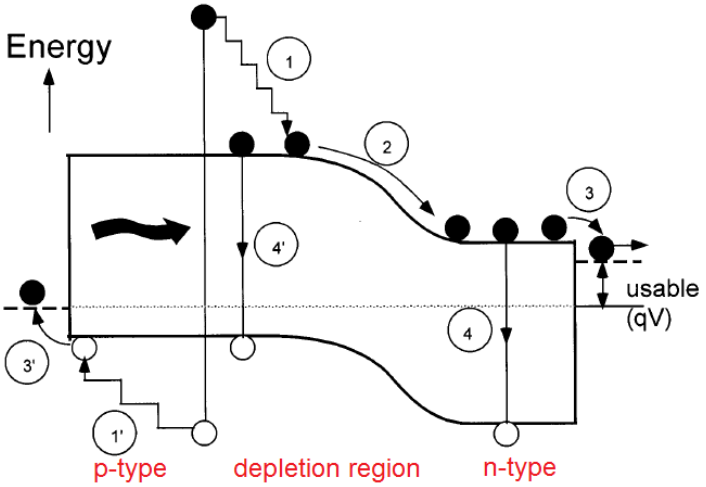

FIGURE 1.2: *Energy band scheme at a junction of a p-type and n-type semiconductor. The band bending is a result of the electric field built in the junction by diffusion of charge carriers along their concentration gradient. Also, the main loss mechanisms are indicated. They are (1) thermal relaxation of charge carriers, (2) energy loss traversing the junction, (3) energy loss at the contacts and (4) recombination of electrons and holes. [5]*

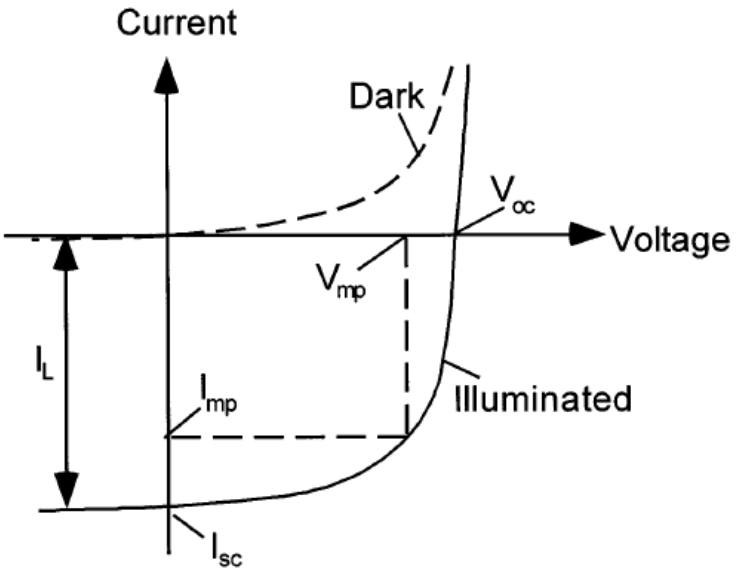

FIGURE 1.3: *The I-V characteristic of the dark (dashed curve) and illuminated (full curve) PV cell. Relevant quantities, like the open circuit voltage, short circuit current and maximum power point are indicated. [5]*

realized in a p-n homojunction or heterojunction - respectively interfaces between two similar and two dissimilar semiconductors. A p-type (n-type) semiconductor possesses an acceptor (donor) level originating from a lattice defect that gives rise to conductivity via holes (electrons). As the concentration of free electrons is higher in the n-type semiconductor, these electrons *diffuse* towards the p-type region and vice versa for the

free holes in the p-type semiconductor. The result is a build-up of negative charge in the p-type region and positive charge in the n-type region. This creates an electric field according to Poisson's equation in electrostatics. The charges in the region around the junction are not free, since they are bound to the lattice defects. In other words, the free charge carriers are depleted, leading to the name *depletion region*. The equilibrium that is attained (ideally) prevents any further diffusion of charge carriers across the depletion region. The electric field leads to band bending in the depletion region, shown in Figure 1.2. Let us now suppose a p-type absorber material, e.g. CIGS (the case of an n-type absorber material is completely analogous). Photogenerated electrons - minority charge carriers in the p-type material - arrive at the depletion region after random motion in the absorber layer [2]. Due to the band bending they can drift towards the n-type layer, yet the holes cannot. The result is a net electric current. An alternative mechanism for step III consists of a Schottky barrier, i.e. a barrier due to band bending at a metal-semiconductor interface.

The current-voltage plot, the so-called *I-V characteristic*, of a PV cell is shown in Figure 1.3. Naturally, it matches the diode characteristic, since a PV cell is in fact a junction diode. In case the PV cell is not illuminated, the curve is located in the first and third quadrant and thus the power $P = I \cdot V$ is always positive. Following the common sign convention in electric circuits, this means that power is consumed by the cell. No current flows unless an *external* potential is applied. Upon illumination, the characteristic is shifted to the fourth quadrant and as a result the cell supplies power. The characteristic of the PV is mainly described by a few special points. The *open circuit voltage*, V_{oc}, is the voltage across the cell in case the circuit is open and no current flows between cathode and anode. The *short circuit current*, I_{sc}, is the current that flows through the circuit in the limit of negligible resistance, so no voltage is produced. The *maximum power point* is the point (V_{mp}, I_{mp}) for which the output power, $P_{OUT}^{max} = I_{mp} \cdot V_{mp}$, is maximal. This leads to the definition of the *efficiency*, η, of the device:

$$\eta = \frac{P_{OUT}^{max}}{P_{IN}} \ , \tag{1.5}$$

the ratio of the maximal attainable output energy P_{OUT}^{max} and the *total* energy of the photon spectrum impinging on the cell, P_{IN}. This spectrum has to be specified to

[2] This is the case for thick absorber layers; in thin layers the electric field in the depletion layer may extend into most of the absorber layer.

report meaningful efficiencies. Naturally, the solar spectrum is often selected as the reference spectrum. In this case, the *air mass* (AM) coefficient is used to further specify the spectrum. It marks the optical path length the photons have traveled through the atmosphere. This is relevant because of absorption and scattering processes. In the AM0 spectrum, the photons have not entered the atmosphere, so it is selected for solar panels of e.g. communication satellites. The AM1 spectrum is defined by a path length of once the thickness of the atmosphere. This is obtained at a zenith angle of 0°, i.e. if the sun is directly overhead at the equator. The most common reference is the AM1.5 spectrum with a path length amounting to 1.5 times the thickness of the atmosphere corresponding to the sun positioned at a zenith angle of 48.19° [6]. Finally, the *fill factor*, FF, measures the deviation of the I-V characteristic from the ideal rectangular form:

$$FF = \frac{P_{OUT}^{max}}{I_{sc} \cdot V_{oc}} = \frac{I_{mp} \cdot V_{mp}}{I_{sc} \cdot V_{oc}} \leq 1 \ . \tag{1.6}$$

The efficiency of the photovoltaic device is limited by a series of loss mechanisms that account for the difference between P_{IN} and P_{OUT}^{max}. The five principal mechanisms of energy loss in PV cells based on a p-n junction are:

0. The energy absorption threshold of the device, equal to the optical band gap of the semiconductor absorber material.

1. Thermal relaxation of the photogenerated charge carriers; the electrons relax to the conduction band minimum (CBM) and the holes to the valence band maximum (VBM).

2. Energy loss from traversing the junction, caused by the band bending in the depletion region.

3. Energy loss at the electric contacts.

4. Premature recombination of charge carrier pairs.

These mechanisms are shown schematically in Figure 1.2. A practical measure for the tendency to recombine is the *diffusion length*, the average distance a carrier can travel until recombination. Impurities and, in polycrystalline absorber materials, grain boundaries often act as recombination centers. It has been demonstrated by W. Shockley and

H. J. Queisser that loss mechanism 4, recombination of charge carriers, is a result of a detailed balance [7]. This detailed balance connects the photogeneration of free charge carrier pairs to the reverse process, recombination. Therefore, recombination is inherent to the PV device. The radiation that results from this recombination is partially emitted by the cell, the rest can be re-absorbed. Their study of the detailed balance between photogeneration and recombination of free charge carriers, has led Schockley and Queisser to calculate a theoretical limit for the efficiency of a single-junction PV cell, the *Shockley-Queisser limit*. Along with recombination, other loss mechanisms should be taken into account. A compromise has to be sought between the absorption threshold (0) and thermal relaxation (1). Reducing the band gap leads to a decrease of the loss due to the absorption threshold. Yet, it effects an increase of the loss due to thermal relaxation, since the photogenerated charge carriers relax maximally, to the CBM and VBM. Taking into account mechanisms 0, 1 and 4, the efficiency as a function of the band gap for 2 spectra - AM0 and AM1.5 - is displayed in Figure 1.4 [3]. The maximum attainable voltage in case of the AM0 spectrum is $\sim$ 30.5 % at a band gap of $\sim$ 1.25 eV. Using the AM1.5 spectrum, relevant for terrestrial devices, the maximum efficiency that follows from the Shockley-Queisser limit is $\sim$ 33.5 % for band gaps of either $\sim$ 1.10 eV and $\sim$ 1.35 eV. The first value corresponds more or less to the band gap of Si (yet Si has the disadvantage of having an indirect gap). It should be noted that although the *efficiency* is lower at AM0 in comparison with AM1.5, the total power output, P_{OUT}, is of course higher since the intensity of the solar radiation is higher outside of the atmosphere. Losses at the junction (2) and the contacts (3) are not included, since they are highly material-dependent. They limit the maximum attainable efficiency further. The limit on the efficiency of *single-junction* PV cells can be overcome by *multi-junction* PV cells (among other techniques). These contain several p-n junctions, all tuned to different photon wavelengths.

[3] The figure originates from the website http://pveducation.org. The website is highly recommended, since it offers a thorough discussion of the basic working principles of PV devices. It is hosted by C. Honsberg and S. Bowden, researchers at the Arizona State University.

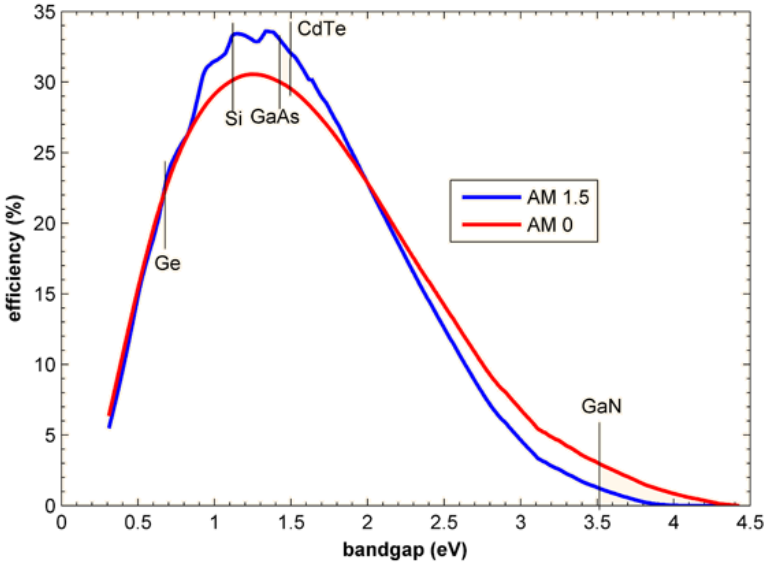

FIGURE 1.4: *The efficiency of single-junction PV cells as a function of the band gap of the absorber material, demonstrating the Shockley-Queisser limit. The absorption threshold, thermal relaxation and recombination (detailed balance) are taken into account for both the AM0 and AM1.5 spectrum. The maximum attainable efficiency of* ~ 33.5 *% using the AM1.5 spectrum as a reference can be achieved at band gaps measuring either* ~ 1.10 *eV and* ~ 1.35 *eV.*

1.2.2 Composition and operation of CIGS photovoltaic cells

Our discussion is primarily based on a recent and very extensive review article by U. P. Singh and S. P. Patra addressing progress in polycrystalline, thin film CIGS photovoltaic cells [8]. Indeed, we focus on polycrystalline CIGS cells since to date they yield the highest cell efficiencies.

The principal advantage of CIGS absorber materials is their high absorption coefficient in the relevant range of photon energies (> 1 eV). The absorption coefficients of a wide range of absorber materials are displayed in Figure 1.5. The absorption coefficient of CIS is $\sim 10^5$ cm^{-1} for 1.5 eV photons, compared with $\sim 10^3$ cm^{-1} of crystalline Si. The high absorption coefficient is related to the fact that CIGS compounds have direct band gaps, contrary to Si, currently the most widely used absorber material. Absorption in a material with a direct band gap relies solely on the probability of the electronic transitions, that follows from Fermi's golden rule. On the other hand, in a material with an indirect gap, the electronic transitions have to be assisted by phonons, placing an extra constraint on the absorption. Therefore, Si absorber layers have to be quite thick, in the order of several hundreds of µm. On the other hand, in CIGS PV cells, the

absorber layer is only ~ 1-2.5 μm. PV cells of this type are called *thin film PV cells*. Other materials with a high absorption coefficient include Ge, a-Si (amorphous Si) and CdTe; all three are direct band gap semiconductors [9]. Ge has a small band gap (~ 0.67 eV) and is thus not suited as an absorber material, according to the Shockley-Queisser plot in Figure 1.4. CdTe and a-Si are also used as absorber materials in thin film PV cells. Other types of thin film PV cells are based on polymers and fairly recently on the kesterite material Cu_2ZnSnS_4 (CZTS).

As a result of the elevated absorption rate, CIGS is one of the most performant absorber materials available. The very first report of a CIS PV cell, containing single-crystal CIS, was published in 1974 [10]. At present, the most efficient CIGS PV cells are grown on flexible polymer films, rather than on the traditional glas substrates [11]. A top lab efficiency of 20.4 % has been reached. It is also the record efficiency among all thin film PV cell technologies.

The composition of a generic CIGS PV cell is shown in Figure 1.6. Layer thickness estimates are given; it is found that the device (not including the substrate) is only a few

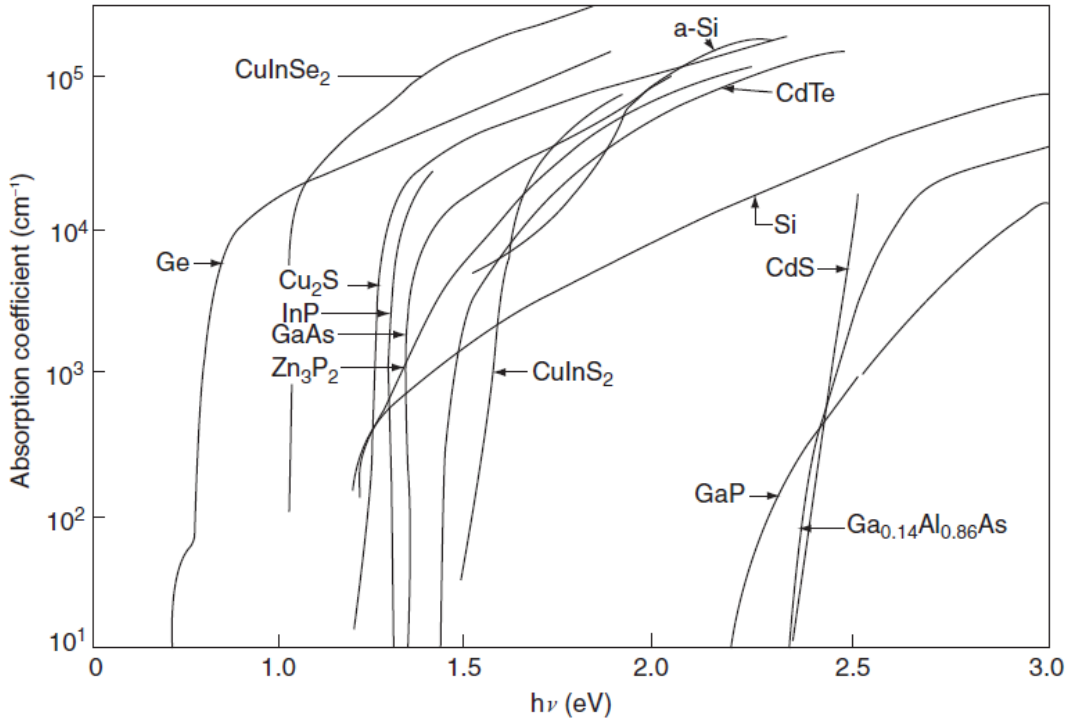

FIGURE 1.5: *The absorption coefficient of several absorber materials as a function of the energy of the impinging photons. Note that the vertical scale is logarithmic. The absorption coefficient of CIS is the highest of all values displayed for photon energies* > 1 *eV. [12]*

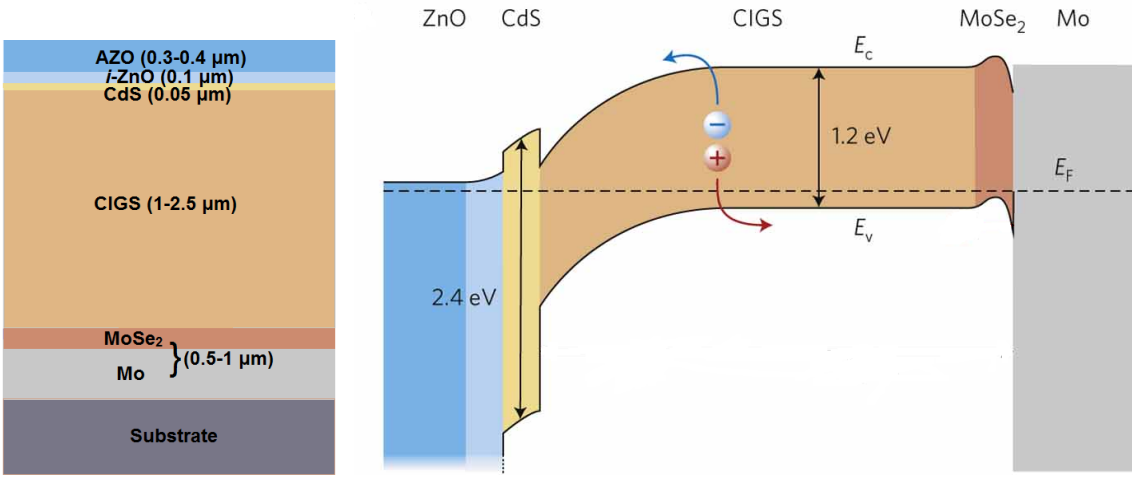

FIGURE 1.6: *(left) A typical layer structure for a CIGS PV cell, with layer thickness estimates. (right) The corresponding band structure. [11]*

µm thick. The substrate may either be made of glass, a metal or a polymer. The band structure of the device is also displayed. At the p-n junction between ZnO and CIGS, buffered by CdS, the charge carriers are separated, as is indicated. The electrons move to AZO, short for ZnO:Al, i.e. ZnO doped with Al, an n-type semiconductor material. The holes are forced in the opposite direction. As we have seen, this is the typical band alignment for a single p-n junction cell. We will discuss the main components and their role in the cell one by one.

Front contact. A combination of a layer of ~ 0.3-0.4 µm AZO and a thin layer of ~ 0.1 µm i-ZnO, intrinsic (undoped) ZnO, forms the front contact, in this case the cathode, of the cell. AZO is an n-type material that forms a heterojunction with the p-type material CIGS. ZnO is a transparent conducting oxide; it has a large band gap of ~ 3.3 eV and is thus mostly transparent, but it is also conducting. This makes it the ideal material of choice for the front contact. The inclusion of the i-ZnO layer yields consistently higher device efficiencies, although the mechanism behind this effect is not fully understood. The i-ZnO layer can be considered to contribute to the buffer between ZnO and CIGS. The front contact is usually grown by sputtering [4].

Buffer layer. The top efficiency devices contain a very thin layer, measuring ~ 0.05 µm, of weakly n-type [5] CdS, the so-called buffer layer. It acts as a buffer both mechanically

[4]This is a high vacuum technique, for which Ar ions are accelerated towards a target. Due to the collisions, the target material is sputtered onto a substrate.

[5]The n-type conductivity of CdS is generally attributed to S vacancy defects.

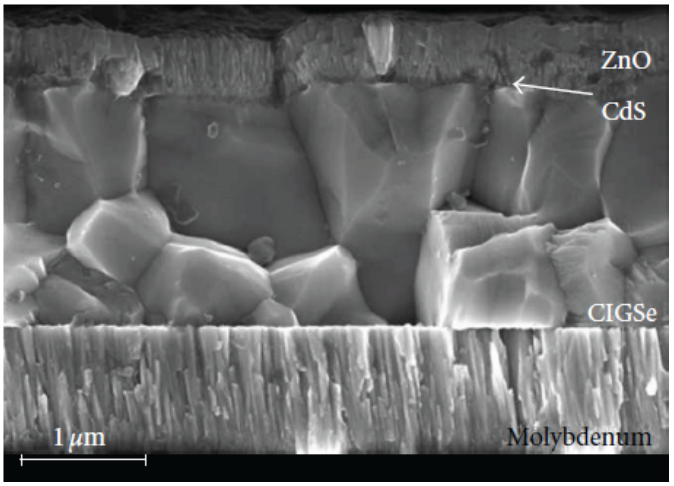

FIGURE 1.7: *SEM image of a cross section of a CIGS thin film cell, showing the polycrystalline CIGS absorber layer and the front and back contact and buffer. [9]*

and electrically. Its mechanical function is to protect the junction during ZnO deposition, in particular if this is achieved by sputtering. Electrically, it has a good band alignment with ZnO and CIGS. The band gap is large, ~ 2.4 eV, and so is the barrier for holes from CIGS to ZnO. The *moderate* potential ascent between CIGS and CdS is found to be beneficial, since it enlarges the energy difference between the VBM of the absorber and the CBM of the buffer. This reduces the chance of recombination of charge carriers at the interface between absorber and buffer. Moreover, the CdS buffer layer builds a sufficiently wide depletion layer that minimizes tunneling of holes in the direction towards ZnO. The CdS layer is commonly synthesized by chemical bath deposition.

Absorber layer. For the CIGS absorber generally a relative Ga amount of ~ 0.3 is chosen. This leads to a band gap of ~ 1.2 eV, close to the band gap needed to obtain the Shockley-Queisser maximum efficiency. The absorber layer is grown in Cu-deficient conditions, usually by ~ 10 % [13] [6]. Synthesis methods for CIGS layers will be discussed in the next section. The resulting vacancies effect p-type conductivity; we will demonstrate this by explicit defect calculations in Chapter 5. The absorber layer of the CIGS cells with top efficiency is polycrystalline. A scanning electron microscopy image that shows this polycrystal can be found in Figure 1.7. The grains of the polycrystal should be sufficiently large, because grain boundaries (GBs) typically act as recombination centers. It has been proposed theoretically by C. Persson and A. Zunger that there is an effect at the GBs of CIGS that counteracts this recombination [14]. This

[6] A Cu-deficiency of 10 % means that 1 out of 10 Cu lattice sites is not occupied by a Cu atom.

effect is a hole barrier from the grain interior (GI) to the grain boundary. The hole barrier is a decrease of the valence band (just as an increase of the conduction band acts as an electron barrier). This would mean the GB is electron-rich. Persson and Zunger state that the hole barrier can be achieved either by (i) reconstruction of the GB leading to substantial Cu-deficiency at the GB or (ii) extrinsic doping by e.g. Na that replaces Cu (Na_{Cu}). Experimentally, both positively and negatively charged GBs have been observed, even within the same sample [15]. The hole barrier model is only one of the theories composed to explain moderate incorporation of Na (typically $\sim$ 0.1 at.%) boosting the efficiency of the PV cell [16]. It leads to an increase of both the V_{oc} and the FF. Persson and Zunger also propose that owing to Na at the GB, phase segregation of $NaInSe_2$ (NIS) occurs. It has a larger band gap than CIS, which could explain the increase in V_{oc}. Other possible mechanisms take place in the GI, for instance Na on an In site (Na_{In}) acting as an acceptor and thus increasing the hole concentration. We will revisit Na doping in Chapter 5, focussing on Na on Cu sites and the formation of NIS. In practice, Na is supplied by diffusion from a sodium lime glas substrate or, in case of a flexible substrate, added explicitly.

Back contact. For the back contact, the anode, most commonly a layer of $\sim$ 0.5-1 μm of the metal molybdenum (Mo) is used. It is deposited by sputtering or electron gun evaporation [7]. There are several reasons why Mo is chosen for this purpose. First, CIGS is grown on top of the back contact and Mo is stable at the temperature of CIGS growth. Secondly, it does not form alloys with Cu, In or Ga. Finally, it has a low contact resistance to CIGS, thus reducing energy losses at the interface between the absorber layer and the back contact. Mo does tend to form a compound with Se, namely $MoSe_2$. The effect of $MoSe_2$ on the band structure of the PV cell is shown in Figure 1.6. Holes can pass through the $MoSe_2$ layer towards the Mo back contact. Electrons, on the other hand, experience a barrier due to the rise of the conduction band. This is called a *back surface field*. As a result, there is a better collection of the electrons, the minority carriers, at the cathode.

[7] This is a form of physical vapor deposition in which a target is bombarded with electrons. This causes the target material to transit to the gas phase, so it can deposit on a substrate.

1.2.3 Synthesis methods for CIGS layers

The most common synthesis methods that are used to form CIGS layers can be divided into two categories: coevaporation and sequential methods. To date, methods on the base of coevaporation lead to the most efficient PV cells. On the other hand, sequential methods are sought in order to produce on a larger scale. For both categories we will present several possible approaches. In case of the sequential methods, one can essentially distinguish between vacuum-based and nonvacuum-based processes. This section is also mainly based on the review article by U. P. Singh and S. P. Patra [8]. In addition, for the nonvacuum sequential deposition methods, a review article by A. N. Tiwari et al. has been consulted [17].

The formation of CIS and competing compounds can in general be represented in a phase diagram as function of the relative amount of Cu and the temperature during growth. The phase diagram is depicted in Figure 1.8. It shows a broad Cu amount and temperature range at which CIS in the chalcopyrite structure, the phase denoted 'α', can be formed. In the GIs of the grains in the PV absorber layer, only one phase, the α-phase, should be present. It is obtained even in conditions of 14 % Cu-deficiency (21.5 at.% Cu) around 600 °C. Although the chalcopyrite structure is formed over a wide range of Cu temperatures, the compound is likely to contain defect, such as Cu vacancies.

1.2.3.1 Coevaporation

The experimental set-up for coevaporation is shown in Figure 1.9. The elements Cu, In, Ga, Se are evaporated simultaneously from Knudsen effusion cells onto a heated substrate. The deposition chamber is pumped to high vacuum to avoid contaminations. The sticking coefficients of Cu, In and Ga are very high, so the growth rate is determined directly by the flux from the effusion cells. There are several possible processes, that mutually differ by the number of stages that are included.

The stationary process. This is the most simple possible approach to coevaporation. All fluxes are constant, as is the substrate temperature.

The bilayer process. This process consists of two stages. The first stage is Cu-rich and improves the mobility of In and Ga. In the second stage, the substrate temperature

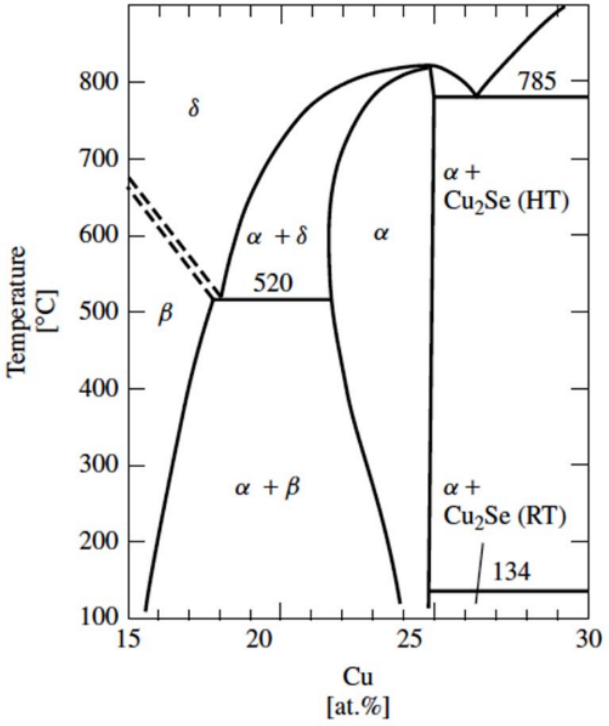

FIGURE 1.8: *The phase diagram of CIS and competing compounds as function of the relative amount of Cu, expressed in units of at.% and temperature during growth, in units of °C. The phase denoted 'α' is CIGS, 'β' is an ordered defect compound (ODC) and 'δ' is a sphalerite phase. The limit of the ODC in Cu-poor conditions is the compound In_2Se_3. In Cu-rich conditions, the Cu_2Se phase coexists with CIGS. [18]*

is elevated and the fluxes of In and Ga are increased. This method has been found to effect larger grain sizes than the stationary method.

The three-stage process. The stages of this process are schematically shown in Figure 1.10. During the first stage In, Ga and Se are deposited at a substrate temperature of ~ 350 °C. For the second stage, the temperature is elevated to ~ 550 °C and Cu and Se are evaporated. The third stage is more or less a repetition of the first stage, in which In, Ga and Se are deposited. The substrate is not kept at a constant temperature, but is left to cool down. Using the three-stage process, the number of defects at the junction is reduced. Also, it enables a more uniform deposition of the buffer layers than is attainable in the stationary or bilayer process. Therefore, the overall advantage is a smoother film morphology. This is why the three-stage coevaporation method, to date, leads to the most efficient PV cells.

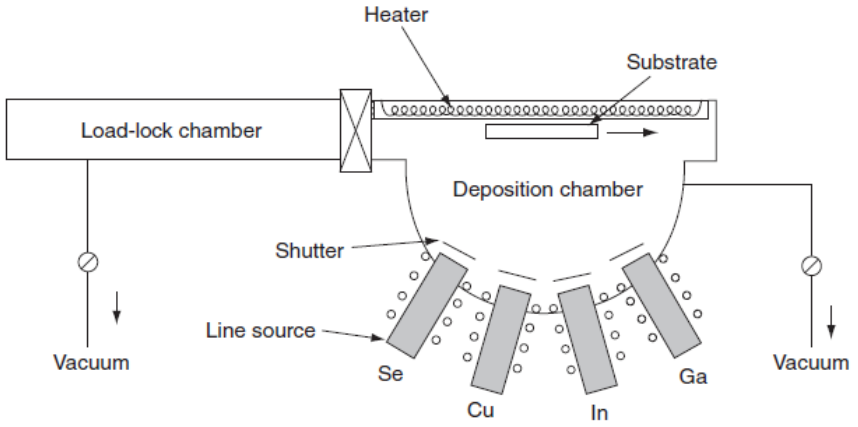

FIGURE 1.9: *The experimental set-up for CIGS synthesis using a coevaporation method. [12]*

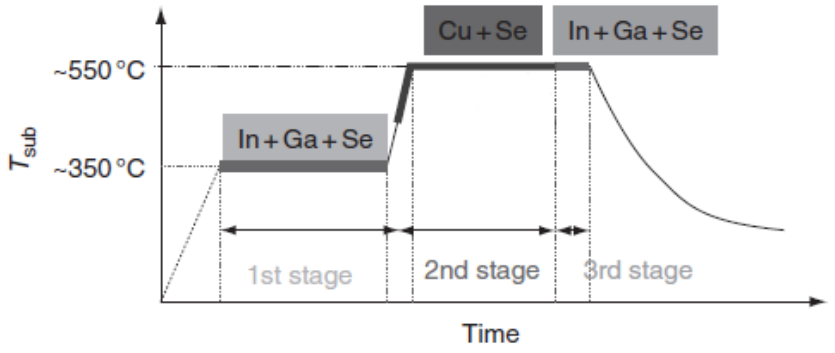

FIGURE 1.10: *Scheme of the stages in a three-stage coevaporation process, indicating the growth time and the temperature of the substrate, T_{sub}. [12]*

1.2.3.2 Sequential methods

In a sequential method, first, a precursor material is prepared. The precursor material then is deposited on a substrate and annealed either in a reactive or an inert environment, inducing the chalcogenization reaction. The main purpose of the development of sequential methods is to scale-up the production of CIGS absorber layers. Large-area films can be grown with a good control of the composition and thickness. Sequential processes are either vacuum-based or nonvacuum-based.

Vacuum-based methods. A basic scheme of this method is displayed in Figure 1.11. A precursor conataining Cu, In and Ga is prepared at temperatures of ~ 150-200 °C, either by sputtering or thermal evaporation. This precursor is subsequently exposed to Se, while at the same time it is annealed at ~ 400-500 °C. This stage is called *selenization*. Se can be supplied in elemental gas form or included in H_2Se.

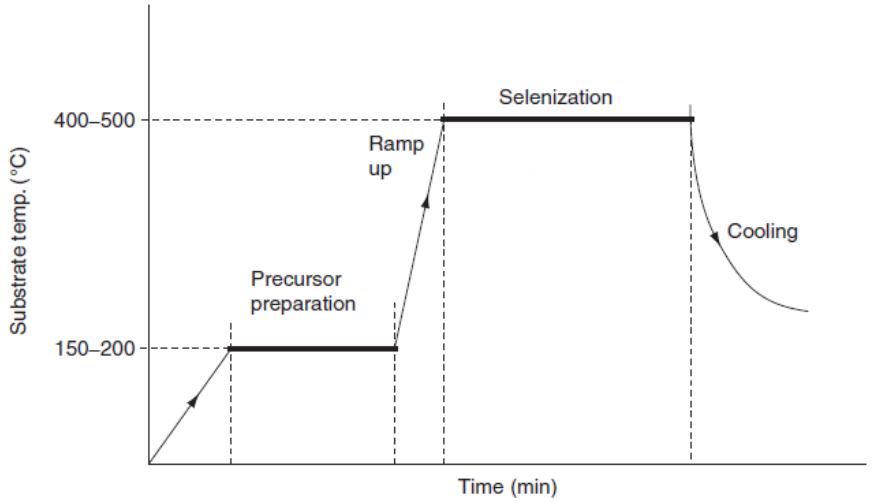

FIGURE 1.11: *Scheme of the sequential process for CIGS growth in vacuum conditions. [12]*

Nonvacuum-based methods. Vacuum-based methods are afflicted with several problems. First of all, material losses of 20 to 50 % are common [12]. The main cause is unintentional deposition of material on the vacuum chamber walls. Also, creating and maintaining a vacuum demands a high energy input. On top of this, vacuum-based methods tend to be relatively slow. To overcome these limitations, nonvacuum-based methods are gaining interest. They reduce the material losses to almost zero [17]. Overall they are also known as *wet methods*, as they often rely on the inclusion of the precursor material in a solution. Nonvacuum-based sequential methods can basically be divided in three categories, mutually different by the precursor material and deposition method. These categories are:

1. *Electrochemical reactions* in a solution, leading to coating of the substrate.
2. Processes coating a *molecular precursor solution* on the substrate by mechanical means, e.g. spraying.
3. *Particulate-based processes* in which solid nanoparticles are dispersed in an organic solvent, dubbed an 'ink', that is to be coated onto the substrate. The ink can be coated on the substrate by printing, spraying or spin coating [8].

We restrict ourselves to a discussion of the particulate-based processes, in connection to Chapter 5 of this thesis. There, we will study C defects that may be included in

[8] Spin-coating is spreading out a liquid on a spinning substrate as a result of the centrifugal force.

CIGS layers, due to the presence of organic solvents in the precursor ink. The precursor nanoparticles can be CIGS particulates, that are already equipped with the right stoichiometry. However, using this precursor, a problem arises: annealing is difficult because of the high melting point of CIGS. This causes cracks and voids in the absorber layer, thus severely affecting the PV cell efficiency. A better alternative is formed by particulates containing multiple phases of either oxides or selenides. The oxide phases have to be reduced to an Cu-In-Ga alloy using a H_2/N_2 gas mixture and subsequently selenized by H_2Se. Particulate containing (Cu,Se), (In,Se) and (Ga,Se) phases undergo a chalcogenization reaction upon annealing. Currently, the top efficiency achieved using particulate-based processes is 17.1 % (in comparison to 20.4 % in vacuum processes) [19].

1.3 Goal and outline of this thesis

As we have seen, owing to its high absorption coefficient (that exceeds the one of Si by approximately 100 times), CIGS can readily be used as an absorber material in thin film PV cells. Those cells based on CIGS have record efficiency in the category of thin film cells. There are other aspects of CIGS that attract attention. First, the band gap of the compound can be varied by altering the Ga-to-In ratio. As such, the band gap can be adapted to minimize losses (as given by the Shockley-Queisser limit) and to optimize the band alignment of the device. Also, contrary to what is found for most materials, CIGS polycrystalline absorber layers outperform their single-crystal counterparts. We focus our theoretical study on the CIGS absorber layer itself, rather than the complete device. Still, the topics we cover are inspired by the application of the absorber in a real device. In doing so, we do not restrict ourselves to the prevalent heterojunction device containing polycrystalline CIGS and grown by means of coevaporation. Other (often novel) types of cells - based on single-crystal CIGS, a CIGS homojunction or grown by an alternative nonvacuum method - are equally considered. Whenever possible, we try to compare results with experimental data.

The composition, growth conditions etc. of CIGS PV devices have for the most part been developed experimentally. An understanding of the device physics at an atomic level is the first major goal of this thesis. It can result in improvements and possibly innovations. For this purpose, first-principles calculations that rely solely on the fundamental laws

of quantum mechanical many-body theory, are well suited. Notably, calculations based on *density functional theory* (DFT) have been applied to CIGS compounds before; J. E. Jaffe and A. Zunger have published one of the early landmark articles presenting a study of CIGS employing DFT [3]. In standard DFT, however, a consistent underestimation of the band gap of semiconductors and insulators is inherent. This is called the *band gap problem*. We have selected a method that mixes a certain amount of Hartree-Fock interaction into DFT, a so-called *hybrid method*, to overcome this band gap problem. Numerical calculations within the hybrid method are computationally very expensive. Only recently, owing to increasing computational power, hybrid calculations have become feasible. Additionally, it is important to include semicore electrons in the calculation, i.a. in view of the importance of the hybridization between Cu-3d and Se-4p orbitals. An overview of standard DFT, hybrid methods and practical calculations is presented in Chapter 2.

We start our investigation of CIGS absorber layers by studying bulk CIGS, with a variable Ga-to-In ratio. This alloying is implemented in a suitable cell, a *supercell* of the primitive unit cell of the chalcopyrite structure. A practical DFT calculation requires, through the use of periodicity, an infinite repetition of this cell. As such, this treatment covers single-crystal layers and larger grains. We study the structural and electronic properties of the alloys in Chapter 3. Alloy properties are emphasised, viz. the influence of the Ga-to-In ratio on the crystal structure and the band gap are investigated, as well as the tendency for phase segregation. Furthermore, a lot of properties derived from the electronic structure are discussed, including the band mass, the character of the chemical bonds and optical properties via the dielectric function. All of these properties are important in a PV absorber layer. Results within a standard DFT method and a hybrid method are consistently compared in Chapter 3. This raises the other major goal of this thesis, namely to review and test present methods in the field of computational solid state physics using a particular material, CIGS, as a reference. A comparison between methods is also useful to assess the accuracy of the results.

In Chapter 4 the study of the electronic structure of the CIGS alloys is extended. The electronic structures obtained in our first-principles are not automatically set on a common energy scale, in other words not *aligned*. The mutual alignment of CIGS compounds (with varying Ga-to-In ratio) is important for the design of a suitable band structure for a PV device. Again, we compare essentially different methods, viz. (i) based on the

branch-point energy (BPE) and (ii) based on a *slab calculation*. The BPE is a notion originating from surface physics, yet it can be calculated from merely the bulk band structure. We calculate it in two ways, first as the zero of a Green's function and secondly as a Brillouin zone average of the band structure [20, 21]. A slab calculation, on the other hand, requires a supercell that contains the slab extending in two directions and an adequate amount of vacuum. Its main advantage is its absolute reference (the potential in vacuum), whereas the BPE method can only be used for a relative alignment. At the end of Chapter 4, the implications of the BPE on the electronic properties of the grain boundaries are briefly discussed.

As we have described in this introductory chapter, CIGS PV cells rely on a p-n junction between p-type CIGS and an n-type material (commonly the ZnO:Al). Therefore, in Chapter 5, we investigate a selection of *point defects* that may contribute to this conductivity. A point defect is an irregularity in the lattice of the order of magnitude of an atom. This can be a vacant site (vacancy defect), a substitution by an atom of another element (substitutional defect) or an additional atom in the interstitial space (interstitial defect). We study single point defects implemented in sufficiently large supercells to reduce the spurious interaction between defects. The electrical conductivity of the defect is studied by calculating the *formation energy* of the defect in several charge states. Based on this, we are able to identify whether the defect is likely to be formed, whether the defect is electrically active and which type of conductivity (p-type or n-type) it results in. Our selection of defects is made on the base of experimental evidence and current technological interest. In view of the Cu defiency during the growth of CIGS, Cu vacancies are first considered. Subsequently, the effect of Na doping - known to be beneficial for the performance of the device - is reviewed. Both Cu vacancies and Na doping in CIGS have been studied before, principally by Zunger and co-workers [22–24]. We attempt to improve on their results by (i) using a hybrid method to correct for the band gap problem in DFT and by (ii) selecting larger supercells to approach the single defect limit. Finally, we compute the formation energy of a series of C defects, both substitutional and interstitial defects. To our knowledge, no publications exist at present, reporting on the effect of C defects on the electronic properties of CIGS. C is present in particulate-based nonvacuum growth methods, which are being developed to produce CIGS layers more efficiently [17]. We aim to find out whether C defects are likely to form and what effect they have on the electrical conductivity.

Chapter 2

Density Functional Theory

2.1 Introduction

In this chapter, we explain the foundations of *Density Functional Theory* (DFT), a quantum mechanical method for the solution of many-body problems. The charge density is the central variable in DFT, since the energy is expressed as a functional (function with a function as variable) of the density. DFT is a so-called *first-principles* or *ab-initio* method, as it is based only on fundamental laws and constants and not on empirical input. To start with, the general many-body problem is introduced. Approximations to the many-problem, as the *Born-Oppenheimer* and *Hartree-Fock approximations* are also studied. Subsequently, the theoretical backbone of DFT, the *Hohenberg-Kohn* theorems and the *Kohn-Sham equations* are reviewed. Several functionals will be considered, most prominently the *hybrid functional*. Using the hybrid functional helps to overcome the intrinsic problem of more basic functionals: a significant underestimation of the band gap of insulators and semiconductors. In a further section practical methods for DFT are summed up. This includes the Bloch theorem, the basis set, k-point grid and pseudopotentials and PAWs. Ultimatelly, we discuss the *Vienna Ab-initio Software Package* (VASP), a package in which i.a. DFT is implemented and which has been used to obtain the results presented in Chapters 3-5. References that have regularly been consulted are [25–29], alternative references are listed explicitly.

2.2 The many-body problem in a solid

The quantum mechanical many-body problem in a solid is described by the time-independent Schrödinger equation:

$$\hat{H}\Psi\left(\mathbf{r}_1, \sigma_1, \mathbf{r}_2, \sigma_2, ..., \mathbf{R}_1, \mathbf{R}_2, ...\right) = E\Psi\left(\mathbf{r}_1, \sigma_1, \mathbf{r}_2, \sigma_2, ..., \mathbf{R}_1, \mathbf{R}_2, ...\right) \ , \tag{2.1}$$

where Ψ is the many-body wavefunction, dependent on the positions and spin of the electrons, $\mathbf{r}_i, \sigma_i$ and the positions of the nuclei, $\mathbf{R}_i$. In principle the wavefunction also depends on the spins of the nuclei, but this will be neglected. The reason is that we can treat the nuclei in a solid as classical particles within the Born-Oppenheimer approximation (discussed in the next section). The Hamiltonian $\hat{H}$ of the system of electrons and nuclei is:

$$\begin{aligned}\hat{H} = &-\sum_i \frac{\hbar^2}{2m_e}\boldsymbol{\nabla}_i^2 - \sum_I \frac{\hbar^2}{2M_I}\boldsymbol{\nabla}_I^2 - \frac{1}{4\pi\epsilon_0}\sum_{i,I}\frac{Z_I e^2}{|\mathbf{r}_i - \mathbf{R}_I|} \\ &+\frac{1}{2}\ \frac{1}{4\pi\epsilon_0}\sum_{i\neq j}\frac{e^2}{|\mathbf{r}_i - \mathbf{r}_j|} + \frac{1}{2}\ \frac{1}{4\pi\epsilon_0}\sum_{I\neq J}\frac{Z_I Z_J e^2}{|\mathbf{R}_i - \mathbf{R}_j|} \ ,\end{aligned} \tag{2.2}$$

where m_e and M_I are the masses of electrons and nuclei, Z_I are the atomic numbers of the nuclei and ϵ_0 is the vacuum permittivity. The five terms of the Hamiltonian can be denoted as:

$$\hat{H} = \hat{T}_e + \hat{T}_n + \hat{V}_{ext} + \hat{V}_{int} + \hat{V}_n \ . \tag{2.3}$$

In this Hamiltonian, $\hat{T}_e$ and $\hat{T}_n$ are the kinetic energy operators of the electrons and nuclei respectively. $\hat{V}_{ext}$, $\hat{V}_{int}$ and $\hat{V}_n$ represent the electron-nucleus, electron-electron and nucleus-nucleus Coulomb interactions. To simplify the notation, we proceed by using atomic units, i.e. $\hbar = e = m_e = 4\pi\epsilon_0 = 1$.

2.2.1 Born-Oppenheimer approximation

The many-body problem cannot be solved analytically for any system more complicated than the dihydrogen cation (H_2^+) and thus approximations have to be made. A first one is the *Born-Oppenheimer approximation* (BO), considering the electrons to move in the field of fixed nuclei. The justification of the BO approximation is the fact that the nuclei are much heavier than the electrons, the ratio of their masses being ~1800 for the

lighest element, H. In the BO approximation, the operators $\hat{T}_n$ and $\hat{V}_n$ are reduced to classical energies T_n and V_n. The direct consequence of BO is the decomposition of the many-body wavefunction into an electronic wavefunction ψ and a nuclear wavefunction χ:

$$\Psi\left(\mathbf{r}_1, \sigma_1, \mathbf{r}_2, \sigma_2, ..., \mathbf{R}_1, \mathbf{R}_2, ...\right) = \psi\left(\mathbf{r}_1, \sigma_1, \mathbf{r}_2, \sigma_2, ...; \mathbf{R}_1, \mathbf{R}_2, ...\right) \cdot \chi\left(\mathbf{R}_1, \mathbf{R}_2, ...\right) \ . \quad (2.4)$$

The electronic wavefunction depends on the nuclear positions as parameters and not as variables, since the electrons rearrange immediately as the nuclear positions are altered. In relation to the Pauli exclusion principle for fermions, the electronic wavefunction is antisymmetric under the interchange of two electrons. Filling in wavefunction 2.4 into the Schrödinger equation (2.3), the following electronic eigenvalue equation is obtained:

$$\hat{H}_{BO}\psi\left(\mathbf{r}_1, \sigma_1, \mathbf{r}_2, \sigma_2, ...; \mathbf{R}_1, \mathbf{R}_2, ...\right) = E_e\left(\mathbf{R}_1, \mathbf{R}_2, ...\right)\psi\left(\mathbf{r}_1, \sigma_1, \mathbf{r}_2, \sigma_2, ...; \mathbf{R}_1, \mathbf{R}_2, ...\right) \ . \quad (2.5)$$

The BO Hamiltonian contains only those terms of the general Hamiltonian 2.3 involving electrons:

$$\hat{H}_{BO} = \hat{T}_e + \hat{V}_{ext} + \hat{V}_{int} \quad (2.6)$$

and the associated energy $E_e(\mathbf{R}_1, \mathbf{R}_2, ...)$ only depends on the nuclear coordinates and not on the electronic coordinates. The total energy of the many-body system in the BO approximation is:

$$E_{tot} = E_e + T_n + E_n \ , \quad (2.7)$$

where the last two terms represent the classical kinetic energy and the classical electrostatic energy. The BO approximation is implied in the rest of the chapter.

2.2.2 Hartree-Fock approximation

A second approximation that can be applied, is the *Hartree-Fock approximation* (HF). In the HF approximation the electronic wavefunction ψ, introduced in the BO approximation, is rewritten as an antisymmetric product of one-particle wavefunctions $\phi_i(\mathbf{r}_i, \sigma_i)$:

$$\psi(\mathbf{r}_1, \sigma_2, \mathbf{r}_2, \sigma_2, ...) = \frac{1}{\sqrt{N!}} \sum_{p}^{N!} (-1)^p \hat{P}\left[\phi_1(\mathbf{r}_1, \sigma_1) \cdot \phi_2(\mathbf{r}_2, \sigma_2) \cdot ... \cdot \phi_N(\mathbf{r}_N, \sigma_N)\right] \ , \quad (2.8)$$

where N is the number of electrons and $\hat{P}$ is the permutation operator yielding $N!$ permutations. Each of these is characterized by a number of elementary permutations of two electrons, p. As such, the wavefunction can be rewritten as a determinant, the so-called *Slater determinant*:

$$\begin{aligned}\psi(\mathbf{r}_1,\sigma_2,\mathbf{r}_2,\sigma_2,...) &= \frac{1}{\sqrt{N!}}\begin{vmatrix} \phi_1(\mathbf{r}_1,\sigma_1) & \phi_2(\mathbf{r}_1,\sigma_1) & . & . & . & \phi_N(\mathbf{r}_1,\sigma_1) \\ \phi_1(\mathbf{r}_2,\sigma_2) & \phi_2(\mathbf{r}_2,\sigma_2) & . & . & . & \phi_N(\mathbf{r}_2,\sigma_2) \\ . & . & & & & . \\ . & . & & & & . \\ . & . & & & & . \\ \phi_1(\mathbf{r}_N,\sigma_N) & \phi_2(\mathbf{r}_N,\sigma_N) & . & . & . & \phi_N(\mathbf{r}_N,\sigma_N) \end{vmatrix} \\ &\equiv \frac{1}{\sqrt{N!}}\left|\phi_1,\phi_2,...,\phi_N\right| \ .\end{aligned} \tag{2.9}$$

An equation for the one-particle orbitals ϕ_i can be derived by making use of the *variational principle* of quantum mechanics. It states that the energy corresponding with a variational wavefunction $\tilde{\psi}$ always exceeds the ground state energy E_0:

$$E_0 \leq \frac{\langle\tilde{\psi}|\hat{H}|\tilde{\psi}\rangle}{\langle\tilde{\psi}|\tilde{\psi}\rangle} \ . \tag{2.10}$$

Orthonormalization of the one-electron orbitals, $\langle\phi_i|\phi_j\rangle = \delta_{ij}$, is imposed by using Lagrange multipliers. Since the derivation of the HF equation is lengthy, it will not be presented here [1].

The result of the HF approximation is the HF equation for the one-electron orbitals $\phi_i(\mathbf{r}_1)$. The Hamiltonian consists of a one-electron operator, $\hat{h}_1$ and two two-electron operators, $\hat{J}$ and $\hat{K}$:

$$\left[\hat{h}_1 + \hat{J} - \hat{K}\right]\phi_i(\mathbf{r}_1) = \varepsilon_i\phi_i(\mathbf{r}_1) \ . \tag{2.11}$$

The one-electron operator is:

$$\hat{h}_1 = -\frac{1}{2}\boldsymbol{\nabla}_1^2 - \sum_I \frac{Z_I}{r_{1I}} \ , \tag{2.12}$$

where $r_{1I} = |\mathbf{r}_1 - \mathbf{R}_I|$. The first term represents the kinetic energy of the electrons and the second term is the operator of the Coulomb interaction between electrons and nuclei.

[1] It can be found in i.a. Ref. [25].

The first two-electron operator, $\hat{J}$, is the *direct* operator. It is given by:

$$\hat{J} = \sum_j \int \phi_j^*(\mathbf{r}_2) \frac{1}{r_{12}} \phi_j(\mathbf{r}_2) d\mathbf{r}_2 \ , \tag{2.13}$$

with $r_{12} = |\mathbf{r}_1 - \mathbf{r}_2|$. The second two-electron operator, $\hat{K}$, is the *exchange* operator:

$$\hat{K} = \sum_{j \| i} \int \frac{\phi_i^*(\mathbf{r}_1)\phi_j^*(\mathbf{r}_2)(1/r_{12})\phi_j(\mathbf{r}_1)\phi_i(\mathbf{r}_2)}{\phi_i^*(\mathbf{r}_1)\phi_i(\mathbf{r}_1)} d\mathbf{r}_2 \ . \tag{2.14}$$

The summation over $j \parallel i$ runs over all electrons with spin parallel to the spin of particle i.

Some important conclusions can be drawn about the HF approximation. First, an exchange density is substracted and accordingly electrons with spin parallel to that of electron i are located outside a region around i. This region is called the *Fermi exchange hole*. Also, due to the presence of the exchange operator, the self-interaction of the electrons cancels in the HF approximation. In the historical predecessor of the HF approximation, the Hartree approximation, the antisymmetrization of the wavefunction is not carried out. As a result, there is no exchange term within the Hartree approximation. Therefore, the Hartree approximation does suffer from self-interaction. We have mentioned that the HF equation is derived using the variational principle. This is why the energy obtained from the HF approximation E_{HF} is always an upper bound of the true ground state energy E_0. The energy difference is called the *correlation energy*: $E_C = E_{HF} - E_0$. The second consequence is that one can systematically improve the accuracy of the approximation in post-HF methods. One of the post-HF methods is the *configuration interaction method* using a linear combination of Slater determinants. The HF equation can be solved in practice by expanding the orbitals in a basis set, e.g. a plane wave basis. The plane wave basis is a complete basis set, yet for practical calculations, a finite number of basis functions, M, is selected. The computational cost of the integral evaluation scales as M^4 in the HF method.

2.3 The fundamentals of Density Functional Theory

In Density Functional Theory (DFT) the electron density $n(\mathbf{r})$ is the principal quantity. The aim of DFT is to reformulate the quantum mechanical theory in terms of the

density instead of the wavefunction. As such, the historical predecessor of DFT is the Thomas-Fermi approach (1927-1928). The electron density $n(\mathbf{r})$ can be calculated from the electron wavefunction as follows:

$$n(\mathbf{r}) = \sum_{i=1}^{N} \int ... \int \psi^*(\mathbf{r}_1, ..., \mathbf{r}_N)\delta(\mathbf{r} - \mathbf{r}_i)\psi(\mathbf{r}_1, ..., \mathbf{r}_N)d\mathbf{r}_1...d\mathbf{r}_N \ , \tag{2.15}$$

where N is the number of electrons.

A *functional* is a function with another function as a variable, denoted $F[f]$. For instance, in DFT, the energy is written as a functional of the density, $E[n]$. The *functional derivative* is defined as:

$$\frac{\delta}{\delta f(x)} F[f] = \lim_{\epsilon \to 0} \frac{F[f(x) + \epsilon\delta(x - x')] - F[f(x)]}{\epsilon} \ . \tag{2.16}$$

Important properties of functional derivation include (without proof):

$$\frac{\delta}{\delta f(x)} \left(\int F[f] \ dx \right) = \frac{\partial F[f]}{\partial f(x)} \ , \tag{2.17}$$

$$\frac{\delta}{\delta f(x)} \left(\int F[f] \ f(x) \ dx \right) = \frac{\partial F[f]}{\partial f(x)} \ f(x) + F[f(x)] \ , \tag{2.18}$$

$$\frac{\delta}{\delta f(x)} \left(\frac{1}{2} \iint g(x, x') \ f(x) \ f(x') \ dx \ dx' \right) = \int g(x, x') \ f(x') \ dx' \ . \tag{2.19}$$

2.3.1 The Hohenberg-Kohn theorems

The Hohenberg-Kohn theorems (HK), have been formulated in 1964 by P. Hohenberg and W. Kohn [30]. The HK theorems form the foundation of DFT. The first HK theorem states that:

> *For any system of interacting particles in an external potential $V_{ext}(\boldsymbol{r})$, this potential is determined uniquely - except for a constant - by the ground state density $n_0(\boldsymbol{r})$.*

The first HK theorem can be proven by reductio ad absurdum. Suppose there exist two Hamiltonians:

$$\begin{cases} \hat{H}_1 = -\frac{1}{2}\sum_{i=1}^{N} \boldsymbol{\nabla}_i^2 + \hat{V}_{int} + \hat{V}_{ext}^{(1)} \\ \hat{H}_2 = -\frac{1}{2}\sum_{i=1}^{N} \boldsymbol{\nabla}_i^2 + \hat{V}_{int} + \hat{V}_{ext}^{(2)} \end{cases} \tag{2.20}$$

with $\hat{V}_{ext}^{(1)}$ and $\hat{V}_{ext}^{(2)}$ differing by more than a constant. This is combined with the following set of Schrödinger equations:

$$\begin{cases} \hat{H}_1\Psi_1 = E_1\Psi_1 \\ \hat{H}_2\Psi_2 = E_1\Psi_2 \ . \end{cases} \tag{2.21}$$

In this expression $\Psi_1 \neq \Psi_2$. To prove this lemma, suppose that $\Psi_1 = \Psi_2 = \Psi$, then substracting the equations in 2.21 produces:

$$\left(\hat{V}_{ext}^{(1)} - \hat{V}_{ext}^{(2)}\right)\Psi = (E_1 - E_2)\Psi \ . \tag{2.22}$$

The energy difference $E_1 - E_2$ is a constant shift and so $\hat{V}_{ext}^{(1)}$ and $\hat{V}_{ext}^{(2)}$ also differ by merely a constant. This contradicts our previous assumption and thus $\Psi_1 \neq \Psi_2$. However, both wave functions lead to the same electron density. Returning to the main proof, one uses the variational principle to obtain:

$$E_1 < \langle\Psi_2|\hat{H}_1|\Psi_2\rangle = \langle\Psi_2|\hat{H}_1 - \hat{H}_2 + \hat{H}_2|\Psi_2\rangle \ . \tag{2.23}$$

Using Equations 2.20 and 2.21 results in:

$$\begin{aligned} \langle\Psi_2|\hat{H}_1 - \hat{H}_2 + \hat{H}_2|\Psi_2\rangle &= \langle\Psi_2|\hat{V}_{ext}^{(1)} - \hat{V}_{ext}^{(2)}|\Psi_2\rangle + E_2 \\ &= \int n_0(\mathbf{r})\left(V_{ext}^{(1)}(\mathbf{r}) - V_{ext}^{(2)}(\mathbf{r})\right)d\mathbf{r} + E_2 \end{aligned} \tag{2.24}$$

and combining Equations 2.23 and 2.24 gives:

$$E_1 - E_2 < \int n_0(\mathbf{r})\left(V_{ext}^{(1)}(\mathbf{r}) - V_{ext}^{(2)}(\mathbf{r})\right)d\mathbf{r} \ . \tag{2.25}$$

An analogous derivation starting from:

$$E_2 < \langle\Psi_1|\hat{H}_2|\Psi_1\rangle \tag{2.26}$$

produces:

$$E_1 - E_2 > \int n_0(\mathbf{r}) \left(V_{ext}^{(1)}(\mathbf{r}) - V_{ext}^{(2)}(\mathbf{r}) \right) d\mathbf{r} \ . \tag{2.27}$$

Since the inequalities are strict, Equations 2.25 and 2.27 cannot both be true and therefore the assumption that the external potentials differ by more than a constant does not hold. This proves the first HK theorem.

The second HK theorem states:

> *A universal functional for the energy $E[n]$ in terms of the density $n(\boldsymbol{r})$ can be defined, valid for any external potential $V_{ext}(\boldsymbol{r})$. The exact ground state energy of the system is the global minimum of this functional and the density that minimizes the functional is the exact ground state density $n_0(\boldsymbol{r})$.*

The first part of this theorem follows immediately from the first HK theorem, upon fixing the possible constant shift in the potential. The functional $E[n]$ takes the form:

$$E[n] = T[n] + E_{int}[n] + E_{ext}[n] \ , \tag{2.28}$$

determined uniquely by the density. The second part of the theorem provides a method for the determination of the ground state density.

The proof follows directly from the variational principle. The ground state energy is:

$$E_0 = \langle \Psi_0 | \hat{H} | \Psi_0 \rangle \ , \tag{2.29}$$

Ψ_0 being the true ground state wave function. The variational principle then reads:

$$E = \min_{\Psi} \langle \Psi | \hat{H} | \Psi \rangle \ . \tag{2.30}$$

This minimization over Ψ produces the correct ground state density n_0, since $n \neq n_0$ corresponds to a wavefunction different from Ψ_0. Therefore, the ground state density minimizes the energy functional, leading to the ground state energy:

$$E_0 = E[n_0] = \min_{\Psi \to n_0} \langle \Psi | \hat{H} | \Psi \rangle \ . \tag{2.31}$$

This proves the second HK theorem.

In the proofs of the HK theorems we have used that two different wavefunctions cannot both minimize the expectation value of the Hamiltonian. This means that non-degenerate states are implied. The HK theorems can be extended to include degenerate states, in the Levy-Lieb formulation. Moreover, we have only considered the ground state energy of the many-body system in the HK theorems. Thus, it is implied that the system is described at zero temperature. In standard DFT, this is always the case.

2.3.2 The Kohn-Sham equations

The HK theorems provide a formal framework to find the ground state density and the ground state energy of a many-body system. Yet, so far, we do not have a method to simplify the many-body problem within DFT. The most widely method for this purpose has been established by W. Kohn and L. J. Sham [31]. The essence of the *Kohn-Sham approach* (KS) is rewriting the many-body problem as an auxiliary system of non-interacting electrons moving in an effective potential. The constraint is that this auxiliary system should lead to the same electron density as the real system (i.e. n must be 'V-representable'). The functional of the real system is:

$$E\left[n\right] = T\left[n\right] + E_{int}\left[n\right] + E_{ext}\left[n\right] \ . \tag{2.32}$$

We can rewrite $E_{int}\left[n\right]$ as:

$$\begin{aligned} E_{int}\left[n\right] &= \frac{1}{2}\iint \frac{n(\mathbf{r})\ n(\mathbf{r}')}{|\mathbf{r}-\mathbf{r}'|} d\mathbf{r}\ d\mathbf{r}' + E'_{XC} \\ &= E_H + E'_{XC} \ , \end{aligned} \tag{2.33}$$

where the first term is the *Hartree energy*, the classical Coulomb interaction energy in the electron gas, while E'_{XC} is the correction due to quantum mechanical *exchange and correlation* (XC). Functional derivation to n, using Equations 2.17 and 2.19 yields:

$$\frac{\delta E\left[n\right]}{\delta n} = \frac{\delta T}{\delta n} + V_H(\mathbf{r}) + \frac{\delta E'_{XC}}{\delta n} + V_{ext}(\mathbf{r}) = \mu \ . \tag{2.34}$$

In this expression

$$V_H(\mathbf{r}) = \int \frac{n(\mathbf{r}')}{|\mathbf{r}-\mathbf{r}'|} d\mathbf{r}' \tag{2.35}$$

is the the Hartree potential and μ is the chemical potential. The functional of the auxiliary system of non-interacting electrons contains an effective potential $V_{KS}(\mathbf{r})$ replacing the interaction. The functional reads:

$$E\left[n\right] = T_0\left[n\right] + \int V_{KS}(\mathbf{r})\ n(\mathbf{r})\ d\mathbf{r}\ . \tag{2.36}$$

Functional derivation using Equation 2.17 leads to:

$$\frac{\delta E\left[n\right]}{\delta n} = \frac{\delta T_0}{\delta n} + V_{KS}(\mathbf{r}) = \mu\ . \tag{2.37}$$

From the equality the chemical potential in Equations 2.34 and 2.37, the effective KS potential can be specified:

$$V_{KS}(\mathbf{r}) = \frac{\delta T}{\delta n} - \frac{\delta T_0}{\delta n} + \frac{\delta E'_{XC}}{\delta n} + V_H(\mathbf{r}) + V_{ext}(\mathbf{r})\ . \tag{2.38}$$

Here the first three terms can be combined to:

$$\frac{\delta T}{\delta n} - \frac{\delta T_0}{\delta n} + \frac{\delta E'_{XC}}{\delta n} = \frac{\delta E_{XC}}{\delta n} = V_{XC}\ , \tag{2.39}$$

an XC-type potential. As such, the KS potential is:

$$V_{KS}(\mathbf{r}) = V_{XC} + V_H(\mathbf{r}) + V_{ext}(\mathbf{r})\ . \tag{2.40}$$

The corresponding Hamiltonian of the non-interacting system is:

$$\hat{H} = \sum_{i=1}^{N}\left(-\frac{1}{2}\boldsymbol{\nabla}_i^2 + V_{KS}(\mathbf{r}_i)\right) = \sum_{i=1}^{N}\hat{h}_{KS}(i)\ . \tag{2.41}$$

The solution of the Schrödinger equation:

$$\hat{H}\Psi = E\Psi \tag{2.42}$$

is - since there are no interactions - a Slater determinant:

$$\Psi = |\phi_1, \phi_2, ..., \phi_N|\ , \tag{2.43}$$

leading to the KS equations:

$$\hat{h}_{KS}(i)\phi_i(\mathbf{r}) = \varepsilon_i\phi_i(\mathbf{r}) \ , \tag{2.44}$$

where $\phi_i(\mathbf{r})$ are the KS orbitals and ε_i are the KS eigenvalues. The ground state density follows from the KS orbitals through:

$$n_0(\mathbf{r}) = \sum_i |\phi_i(\mathbf{r})|^2 \ . \tag{2.45}$$

The challenge in the KS approach is to find suitable approximations for the XC functional:

$$E_{XC}[n] = T[n] - T_0[n] + E_{int}[n] - E_H[n] \ . \tag{2.46}$$

This will be the subject of the next section, in which several functionals will be discussed. In the Hartree energy $E_H[n]$, the electron in the KS orbital under study is included in $n(\mathbf{r})$. Consequently, as the XC energy is approximated, the self-interaction does not fully cancel in the KS approach. The generalization of the KS approach to allow for spin-polarization is straightforward. KS equations for both spin components can be established.

We will now derive an expression for the total electronic energy in the KS method. The total energy functional reads, using Equation 2.46:

$$\begin{aligned} E[n] &= T[n] + E_{int}[n] + E_{ext}[n] \\ &= T_0[n] + E_H[n] + E_{XC}[n] + E_{ext}[n] \ . \end{aligned} \tag{2.47}$$

We can rewrite $T_0[n]$, making use of the KS equations:

$$T_0[n] = \sum_{i=1}^{N} \varepsilon_i - \int V_{KS}(\mathbf{r})\ n(\mathbf{r})\ d\mathbf{r} \tag{2.48}$$

and fill in $V_{KS}(\mathbf{r})$ as given in Equation 2.40 to obtain:

$$\begin{aligned} T_0[n] &= \sum_{i=1}^{N} \varepsilon_i - \int V_{KS}(\mathbf{r})\ n(\mathbf{r})\ d\mathbf{r} \\ &= \sum_{i=1}^{N} \varepsilon_i - \int \left(V_{XC} + V_H(\mathbf{r}) + V_{ext}(\mathbf{r})\right)\ n(\mathbf{r})\ d\mathbf{r} \\ &= \sum_{i=1}^{N} \varepsilon_i - \int V_{XC}\ n(\mathbf{r})\ d\mathbf{r} - 2E_H[n] - V_{ext}[n] \ . \end{aligned} \tag{2.49}$$

Combining this with Equation 2.47 produces:

$$E\left[n\right] = \sum_{i=1}^{N} \varepsilon_i - E_H\left[n\right] + E_{XC}\left[n\right] - \int V_{XC}\; n(\mathbf{r})\; d\mathbf{r}\;. \tag{2.50}$$

It is thus found that the total electronic energy is not simply a summation of the KS eigenvalues ε_i. The functional $E_{XC}\left[n\right]$ can be written as:

$$E_{XC}\left[n\right] = \int \varepsilon_{XC}(n(\mathbf{r}))\; n(\mathbf{r})\; d\mathbf{r}\;. \tag{2.51}$$

From Equation 2.19 for functional derivation it follows that:

$$V_{XC}\left[n\right] = \frac{\delta E_{XC}\left[n\right]}{\delta n(\mathbf{r})} = \varepsilon_{XC}(n(\mathbf{r})) + \frac{\partial \varepsilon_{XC}\left[n\right]}{\partial n(\mathbf{r})}\; n(\mathbf{r})\;. \tag{2.52}$$

Therefore, the total energy reads:

$$E\left[n\right] = \sum_{i=1}^{N} \varepsilon_i - E_H\left[n\right] - \int \frac{\partial \varepsilon_{XC}\left[n\right]}{\partial n(\mathbf{r})}\; n(\mathbf{r})\; d\mathbf{r}\;. \tag{2.53}$$

Contrary to the HF method, the total energy in the KS approach is not necessarily an upper bound of the true total energy. The reason is that the KS equations have not been derived from the variational principle.

The KS equations can be solved *self-consistently*. This is shown schematically in Figure 2.1. The iteration starts with an initial (trial) value for the electron density $n(\mathbf{r})$. Given an XC functional, the KS potential $V_{KS}(\mathbf{r})$ follows from the initial density. Now the KS equations can be solved, yielding the KS orbitals $\phi_i(\mathbf{r})$. They lead to a new electron density $n(\mathbf{r})$ and a total energy. The density is fed as input to the iteration and this is repeated until self-consistency is reached. In practice, this self-consistency is assessed in terms of the convergence of the total energy. If subsequent values of the total energy differ less than the convergence criterion that has been selected, the total energy, forces, stresses etc. can be output.

2.4 Exchange-correlation functionals

We will review several widely used exchange-correlation (XC) approximations: LDA, GGA and hybrid functionals.

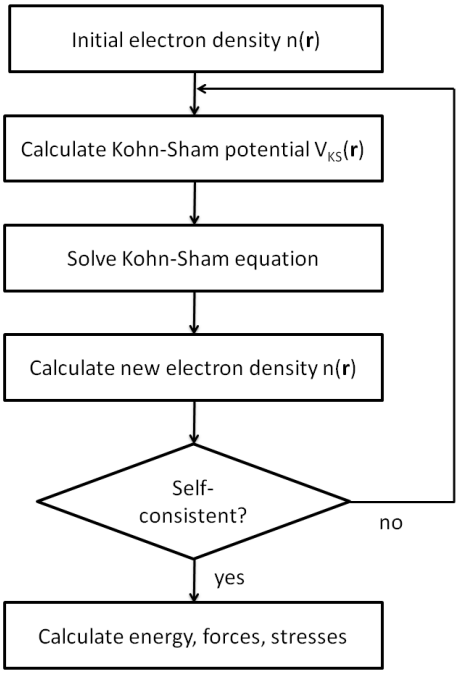

FIGURE 2.1: *Scheme of the self-consistent solution of the Kohn-Sham equations.*

2.4.1 Local density approximation

The *local density approximation* (LDA) is the most simple XC functional, defined as:

$$E_{XC}^{LDA}[n] = \int \varepsilon_{XC}^{UEG}(n(\mathbf{r}))\; n(\mathbf{r})\; d\mathbf{r}\;, \tag{2.54}$$

where $\varepsilon_{XC}^{UEG}(n(\mathbf{r}))$ is the XC energy of an electron in a uniform electron gas (UEG) of density $n(\mathbf{r})$. It depends solely on the local density at point $\mathbf{r}$. The XC energy per electron can be split into the X and the C contribution:

$$\varepsilon_{XC}^{UEG}[n] = \varepsilon_{X}^{UEG}[n] + \varepsilon_{C}^{UEG}[n]\;\;. \tag{2.55}$$

The X energy of an electron in a uniform electron gas has the following analytic form:

$$\varepsilon_{X}^{UEG}[n] = -\frac{3}{4\pi}\left(3\pi^2 n(\mathbf{r})\right)^{1/3}\;\;, \tag{2.56}$$

which in the LDA functional is to be evaluated pointwise. There are, on the other hand, no exact analytic expressions available for $\varepsilon_{C}^{UEG}[n]$ (except in the high- and low-density limit). Approximations can be obtained from quantum Monte-Carlo simulations, as introduced by D. M. Ceperley and B. J. Alder [32].

2.4.2 Generalized gradient approximation

The LDA approximation can be improved on, taking into account the spatial change in the local density by including (powers of) the gradient in the XC functional. This approach is called the *generalized gradient approximation* (GGA). It is important to note that the GGA is still a local approximation, since only the gradient at the same coordinate is taken into account. The XC functional thus takes the form:

$$E_{XC}^{GGA}[n] = \int \varepsilon_{XC}\left(n(\mathbf{r}), |\boldsymbol{\nabla} n(\mathbf{r})|, \boldsymbol{\nabla}^2 n(\mathbf{r}), ...\right)\ n(\mathbf{r})\ d\mathbf{r}\ , \tag{2.57}$$

A commonly used GGA functional is the *Perdew-Burke-Ernzerhof* (PBE) functional [33].

2.4.3 The band gap problem in local approximations

LDA and GGA functionals are meritful in predicting lattice parameters and atomic positions within 1-5 % of the experimental values. Also, the electronic structure of metals is reasonably well described. It is however important to realize that the KS eigenvalues do not necessarily agree with the real energy spectrum. In the derivation of the KS equations, we have only required that the density of the KS system coincides with the real density. Accordingly, the excitation energies are not accurately described by DFT in local approximations like LDA and DFT. As a consequence, the band gaps of insulators and semiconductors are systematically underestimated. This can be understood by carefully studying the KS spectrum. The KS band gap is determined in terms of the N-electron eigenvalues:

$$E_g^{KS} = \varepsilon_{N+1}(N) - \varepsilon_N(N)\ , \tag{2.58}$$

while the real band gap is given by:

$$E_g = \varepsilon_{N+1}(N+1) - \varepsilon_N(N)\ . \tag{2.59}$$

The deviation between both band gaps corresponds to a difference of XC potentials [34]:

$$\begin{aligned} E_g - E_g^{KS} \equiv \Delta_{XC} &= \varepsilon_{N+1}(N+1) - \varepsilon_{N+1}(N) \\ &= \lim_{\eta \to 0} \left[\left(\frac{\delta E_{XC}[n]}{\delta n(\mathbf{r})} \right)_{N+\eta} - \left(\frac{\delta E_{XC}[n]}{\delta n(\mathbf{r})} \right)_{N-\eta} \right]\ , \end{aligned} \tag{2.60}$$

where η is a fractional number of electrons. Δ_{XC} describes the discontinuity of the functional derivative of $E_{XC}[n]$ around N. This discontinuity is not captured by the local functionals and consequently, in LDA and GGA, $\Delta_{XC} = 0$. The resulting band gap is the pure KS band gap, leading to a consistent underestimation of the band gap. This is illustrated in Figure 2.2 for a wide range of semiconductor and insulator materials [35]. The LDA band gaps are compared to the band gaps in the GW approximation (GWA) and the experimental gaps.

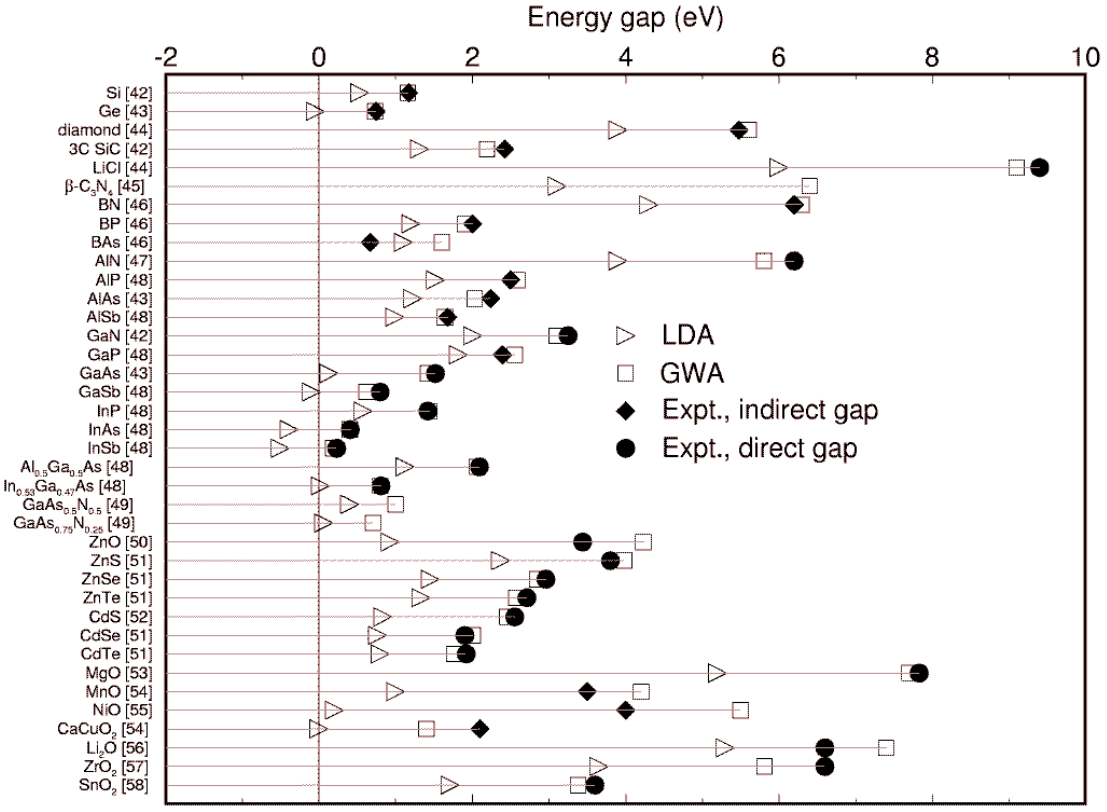

FIGURE 2.2: *Comparison of LDA, GWA and experimental band gaps of insulator and semiconductor materials. It is apparent that LDA consistently leads to an underestimation of the band gap. [35]*

2.4.4 Hybrid functionals

Solving the band gap problem in DFT can be attempted by so-called post-DFT methods. A method first proposed by J. C. Slater is the *Xα method* [36]. It can be regarded as a local-density approximation to the Hartree-Fock equations. A similar approach to

tackle the band-gap problem in DFT is the so-called *LDA+U method*. The parameter U characterizes the direct HF-like interaction between electrons of different bands belonging to a single atom (on site interaction). The result is that in the short-range there is HF-like interaction, that cancels self-interaction arising in DFT [25]. Both the Xα and LDA+U methods can be considered historical predecessors of hybrid functionals. The latter have been first introduced in 1992 by A. D. Becke [37]. Several forms of hybrid functionals have afterwards been developed, e.g. B3LYP and HSE. HSE functionals were introduced by J. Heyd, G. E. Scuseria and M. Ernzerhof in 2003 [38]. Hybrid functionals present a more natural approach to HF mixing with DFT than previous methods.

The *Heyd-Scuseria-Ernzerhof* (HSE) hybrid functional is of the form:

$$E_{XC}^{HSE} = \alpha E_X^{HF,sr}(\mu) + (1-\alpha)E_X^{PBE,sr}(\mu) + E_X^{PBE,lr}(\mu) + E_C^{PBE} \ , \tag{2.61}$$

where lr and sr stand for 'long-range' and 'short-range'. The range of the interaction for the exchange contribution is determined by the parameter μ. The range separation parameter μ is of the order of 0.2 to 0.3 Å^{-1}. The hybrid exchange therefore includes highly unscreened interaction, i.e. molecular-like, at short distance due to mixing with HF. At longer distances the screening is described by the PBE functional, in other words metal-like. Exchange in the HF method has been elaborated in our previous discussion of the HF approximation, cfr. Equation 2.14 for the exchange operator. It is formulated in terms of the single-electron *orbitals* (KS orbitals in DFT), instead of the density and is therefore considered an *implicit* density functional. A common choice for the amount of HF mixing is $\alpha = 0.25$, corresponding with the so-called HSE06 functional. Both the range-separation parameter μ and the HF mixing parameter can be tuned to agree more closely with experimentally observed electronic properties, e.g. the band gap of a semiconductor material. Therefore, calculations with hybrid functionals cannot be considered purely first-principles calculations.

The Coulomb kernel, needed to calculate the exchange energy, is decomposed into a short-range and long-range part by means of error-functions:

$$\begin{aligned} \frac{1}{r} &= \left(\frac{1}{r}\right)^{sr} + \left(\frac{1}{r}\right)^{lr} \\ &= \frac{1}{r}\left(\text{erfc}(\mu r) + \text{erf}(\mu r)\right) \ . \end{aligned} \tag{2.62}$$

As such, at the characteristic distance of $2/\mu$ the short-range interaction becomes negligible. This range-separation is shown in Figure 2.3 for $\mu = 0.2$ Å^{-1}. The corresponding characteristic distance is $r = 2/\mu = 10$ Å. One notices that at this distance $\mathrm{erfc}(\mu r) \approx 0$ and $\mathrm{erf}(\mu r) \approx 1$, so the short-range interaction indeed has become negligible.

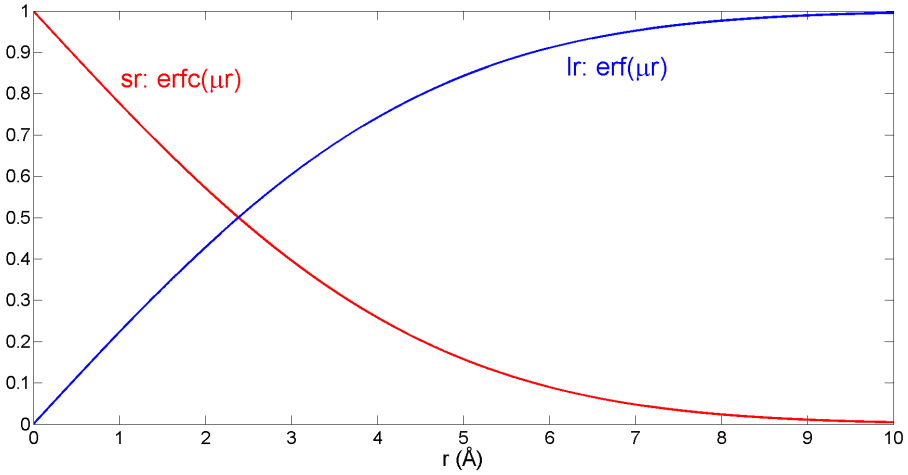

FIGURE 2.3: *Range separation in the hybrid functional by means of $erfc(\mu r)$ (short-range) and $erf(\mu r)$ (long-range).*

2.5 Geometry optimization using the Hellmann-Feynman theorem

The forces acting on the nuclei are obtained as the derivative of the total energy w.r.t. the atomic positions. In equilibrium, all forces are zero:

$$\mathbf{F}_I = -\frac{\partial E}{\partial \mathbf{R}_I} = 0 \ . \tag{2.63}$$

The derivative can be evaluated using the *Hellmann-Feynman theorem*. It is valid for an eigenvalue $E(\lambda)$ of the Hamiltonian $\hat{H}$, λ being a parameter, the derivative w.r.t. λ is found as:

$$\frac{\partial E}{\partial \lambda} = \langle \psi | \frac{\partial \hat{H}}{\partial \lambda} | \psi \rangle \ , \tag{2.64}$$

where $|\psi\rangle$ is an eigenstate of the Hamiltonian. The proof of the Hellmann-Feynman theorem requires a simple application of the product rule of derivation. In our case, the Hamiltonian is given by:

$$\hat{H} = \hat{T} + \hat{V}_{int} + \hat{V}_{ext} + \hat{H}_n \ . \tag{2.65}$$

Following the Born-Oppenheimer approximation the nuclear Hamiltonian $\hat{H}_n$ can be evaluated classically. Application of the Hellmann-Feynman theorem yields:

$$\begin{aligned}\mathbf{F}_I &= -\langle\psi_0|\frac{\partial\hat{H}}{\partial\mathbf{R}_I}|\psi_0\rangle \\ &= -\underbrace{\left\langle\frac{\partial\hat{T}}{\partial\mathbf{R}_I}\right\rangle}_{=0} - \underbrace{\left\langle\frac{\partial\hat{V}_{int}}{\partial\mathbf{R}_I}\right\rangle}_{=0} - \left\langle\frac{\partial\hat{V}_{ext}}{\partial\mathbf{R}_I}\right\rangle - \frac{\partial E_n}{\partial\mathbf{R}_I} \ .\end{aligned} \tag{2.66}$$

The first two terms vanish, since $\hat{T}$ and $\hat{V}_{int}$ do not depend explicitly on $\{\mathbf{R}_I\}$. We obtain that the forces can be calculated from:

$$\mathbf{F}_I = -\int \frac{\partial V_{ext}(\mathbf{r})}{\partial\mathbf{R}_I}\ n_0(r)\ d\mathbf{r} - \frac{\partial E_n}{\partial\mathbf{R}_I} \ . \tag{2.67}$$

Practical schemes for the variation of the atomic positions to approximate the equilibrium structure, will be discussed in a further section.

2.6 Practical calculations

Previously, we have laid the foundation for DFT (the Hohenberg-Kohn theorems) and we have derived a set of equations that simplifies the many-body problem (the Kohn-Sham equations), studying also the crucial exchange-correlation energy. Now, we will investigate how DFT can be implemented practically, for numerical computation.

2.6.1 The Bloch theorem

The first requirement for a practical approach to DFT, is the use of the spatial periodicity of the crystal lattice. Accordingly, the KS potential is periodic for all lattice parameters $\mathbf{R}$ of the lattice:

$$V_{KS}(\mathbf{R}) = V_{KS}(\mathbf{r}+\mathbf{R}) \ . \tag{2.68}$$

A periodic structure is defined by a unit cell, which is repeated in all spatial directions. This may be a supercell of the simple lattice of a material, to implement more complex structures, such as a slab, point defects etc.

For the periodic lattice that has been introduced, the *Bloch theorem* holds:

The wavefunction of a particle in a periodic potential can be written as a product of a plane wave and a periodic function with the same periodicity as the lattice.

This wavefunction can be written as:

$$\phi_{n\mathbf{k}} = e^{i\mathbf{kr}}\ u_{n\mathbf{k}}(\mathbf{r}) \tag{2.69}$$

with

$$u_{n\mathbf{k}}(\mathbf{r}) = u_{n\mathbf{k}}(\mathbf{r}+\mathbf{R})\ . \tag{2.70}$$

It follows easily that the energy spectrum is periodic w.r.t. the reciprocal lattice:

$$E_n(\mathbf{k}) = E_n(\mathbf{k}+\mathbf{G})\ , \tag{2.71}$$

for all reciprocal lattice vectors $\mathbf{G}$. Therefore, the energy spectrum is fully represented within the *first Brillouin zone* (BZ), the primitive cell of the reciprocal lattice. This representation is called the *band structure*. It will continuously be used within this thesis to display the electronic structure.

2.6.2 Planewave basis set

It is convenient to expand a periodic function such as $u_{n\mathbf{k}}(\mathbf{r})$ using a planewave basis set:

$$u_{n\mathbf{k}}(\mathbf{r}) = \sum_{\mathbf{G}} c_{n\mathbf{k}}(\mathbf{G})\ e^{i\mathbf{Gr}}\ , \tag{2.72}$$

where the summation runs over all reciprocal lattice vectors. The planewaves form a complete basis set and thus the expansion is a Fourier series. Herein lies one of the main advantages of a planewave basis, namely, a fast Fourier transform (FFT) can be performed to switch between real and reciprocal space. Using the Bloch theorem, it follows that the electronic wavefunctions are:

$$\phi_{n\mathbf{k}} = \sum_{\mathbf{G}} c_{n\mathbf{k}}(\mathbf{G})\ e^{i(\mathbf{k}+\mathbf{G})\mathbf{r}}\ . \tag{2.73}$$

The kinetic energy related to planewaves in this expansion is $(\mathbf{k}+\mathbf{G})^2/2$. The summation over $\mathbf{G}$ is infinite and thus for practical reasons an upper boundary should be set, the

cutoff energy E_{cut}, so:

$$\frac{(\mathbf{k}+\mathbf{G})^2}{2} < E_{cut} \tag{2.74}$$

or, equivalently:

$$|\mathbf{G}| < G_{max} \ . \tag{2.75}$$

The cutoff can be understood in terms of a 'resolution': details in the wavefunction smaller than $2\pi/G_{max}$ are neglected. It results in the second important advantage of the planewave basis set, namely the accuracy can be improved systematically by increasing E_{cut}.

2.6.3 Integration over the first Brillouin zone: the k-point grid

In DFT, all quantities, e.g. the energy spectrum, are derived from the electron density. The electron density reads:

$$n(\mathbf{r}) = \int_{BZ} d\mathbf{k} \sum_{n=1}^{N_\mathbf{k}} f_{n\mathbf{k}} \ |u_{n\mathbf{k}}(\mathbf{r})|^2 \ , \tag{2.76}$$

where the sum runs over all occupied bands and $f_{n\mathbf{k}}$ is the occupancy of the band, either 1 - below the Fermi level - or 0 [2]. In order to facilitate the convergence of the integration w.r.t. the number of k-points, it is advantegeous to replace the step function by a smooth function. This is a so-called *finite-temperature approach*, also known as *smearing*, since it mimics the effect of temperature [39]. A function frequently used for smearing is the Gaussian function.

For an infinitely extended real space lattice, $\mathbf{k}$ is a continuous variable, restricted to the first BZ owing to periodicity. In a numerical calculation, integration over a continuous variable is not attainable. Therefore, a *k-point grid* is constructed to 'sample' the first BZ. Commonly, a Monkhorst-Pack grid, an equidistant grid, is selected [40]. Additionally, sampling of the *irreducible Brillouin zone* (IBZ), the reduction of the first BZ by the lattice symmetries, is sufficient for the calculation of the density. The normalized weight $w_\mathbf{k}$ has to be included, to take into account the multiplicity of each k-point.

[2] The occupancy is in principle either 1 or 0, but can be 2, 1 or 0 in case spin-orbit coupling is omitted. In the absence of spin-orbit coupling a fully occupied band contains 2 electrons.

Consequently, the electron density becomes:

$$n(\mathbf{r}) \cong \sum_{\mathbf{k}\in IBZ} w_{\mathbf{k}} \sum_{n=1}^{N_{\mathbf{k}}} f_{n\mathbf{k}} \ |u_{n\mathbf{k}}(\mathbf{r})|^2 \ . \tag{2.77}$$

As an example, the IBZ of a simple square reciprocal lattice in 2D is shown in Figure 2.4.

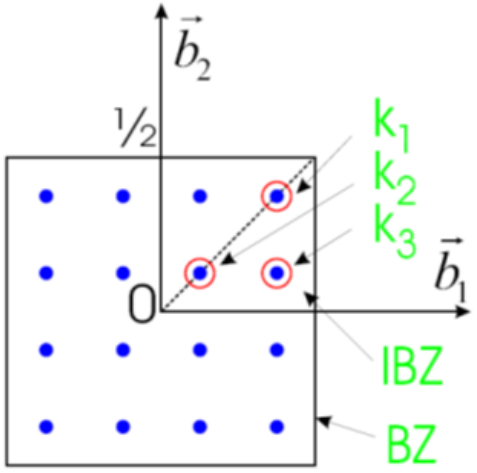

FIGURE 2.4: *The IBZ of a simple square reciprocal lattice in 2D. The IBZ contains the wavevectors* $\boldsymbol{k}_1 = \left(\frac{3}{8}, \frac{3}{8}\right)$ *with weight* $w_{\boldsymbol{k}_1} = \frac{1}{4}$, $\boldsymbol{k}_2 = \left(\frac{1}{8}, \frac{1}{8}\right)$ *with weight* $w_{\boldsymbol{k}_2} = \frac{1}{4}$ *and* $\boldsymbol{k}_3 = \left(\frac{3}{8}, \frac{1}{8}\right)$ *with weight* $w_{\boldsymbol{k}_3} = \frac{1}{2}$.

2.6.4 Pseudopotentials

The electronic wavefunctions (orbitals) of the elements contained in the unit cell are fed as input to a practical DFT routine. The true orbitals may contain many nodes, leading to a huge basis set (a high E_{cut}). Moreover, for bonding, the core electrons are usually not relevant. To illustrate this, the radial parts of the 4d, 5s and 5p orbitals of Mo and Nb are displayed in Figure 2.5. The oscillations of the true (all-electron) valence electron orbitals near the core are due to the core electrons. The nodes - and thus the oscillations - arise from the orthogonality of the orbitals to the core orbitals. In a pseudopotential (PP) method, the effect of the core electrons is removed from the true orbitals yielding a smoothed function. Let us consider an orbital ψ, resulting from a one-electron Schrödinger equation, e.g. the Kohn-Sham equation:

$$\hat{h}\psi = \varepsilon\psi \ . \tag{2.78}$$

Following the principle of the PP method, ψ can be written as:

$$\psi = \phi + \sum_c b_c \psi_c \ , \tag{2.79}$$

where ϕ is a smooth function, corresponding to the true wavefunction ψ outside of a cutoff radius r_c, in the region of chemical bonds. In Figure 2.5 the full curves are examples of smooth wavefunctions coinciding with the true wavefunction outside radius r_c. The summation over c runs over all core orbitals and b_c are the coefficient of the linear combination. As such, we have split the true wavefunction into a smooth and an oscillating contribution. The constants b_c can be determined from the orthogonality of ψ to the core orbitals. We select any of the core orbitals ψ_{c0} to obtain:

$$\langle \psi_{c0} | \psi \rangle = \langle \psi_{c0} | \phi \rangle + b_{c0} \ . \tag{2.80}$$

Therefore:

$$b_{c0} = -\langle \psi_{c0} | \phi \rangle \ , \tag{2.81}$$

and inserting this in Equation 2.82 results in:

$$\psi = \phi - \sum_c \langle \psi_c | \phi \rangle \psi_c \ . \tag{2.82}$$

This formula is related to the Gramm-Schmidt orthogonalization procedure. Then, the one-electron eigenvalue equation 2.78 becomes:

$$\begin{aligned} \hat{h}\psi(\mathbf{r}) &= \hat{h}\phi(\mathbf{r}) + \sum_c b_c \hat{h}\psi_c(\mathbf{r}) \\ &= \hat{h}\phi(\mathbf{r}) - \sum_c \int \psi_c^*(\mathbf{r}')\phi(\mathbf{r}')d\mathbf{r}' \varepsilon_c \psi_c(\mathbf{r}) \ , \end{aligned} \tag{2.83}$$

where we have used that $\hat{h}\psi_c = \varepsilon_c \psi_c$. Alternatively we can write:

$$\begin{aligned} \hat{h}\psi(\mathbf{r}) &= \epsilon\psi(\mathbf{r}) \\ &= \hat{h}\phi(\mathbf{r}) - \sum_c \int \psi_c^*(\mathbf{r}')\phi(\mathbf{r}')d\mathbf{r}' \varepsilon \psi_c(\mathbf{r}) \ . \end{aligned} \tag{2.84}$$

Combining Equations 2.83 and 2.84 gives a single-electron equation for the smooth wavefunction ϕ:

$$\hat{h}\phi(\mathbf{r}) + \sum_c (\varepsilon - \varepsilon_c) \int \psi_c^*(\mathbf{r}')\phi(\mathbf{r}')d\mathbf{r}'\psi_c(\mathbf{r}) = \varepsilon\phi(\mathbf{r}) \ . \tag{2.85}$$

The left hand side consists of the one-particle Hamiltonian $\hat{h}$ and a non-local operator, both acting on $\phi(\mathbf{r})$. Equation 2.85 can be rewritten by introducing the PP $\hat{V}_{ps}$:

$$\left(-\frac{1}{2}\boldsymbol{\nabla}^2 + \hat{V}_{ps}\right)\phi(\mathbf{r}) = \varepsilon\phi(\mathbf{r}) \ . \tag{2.86}$$

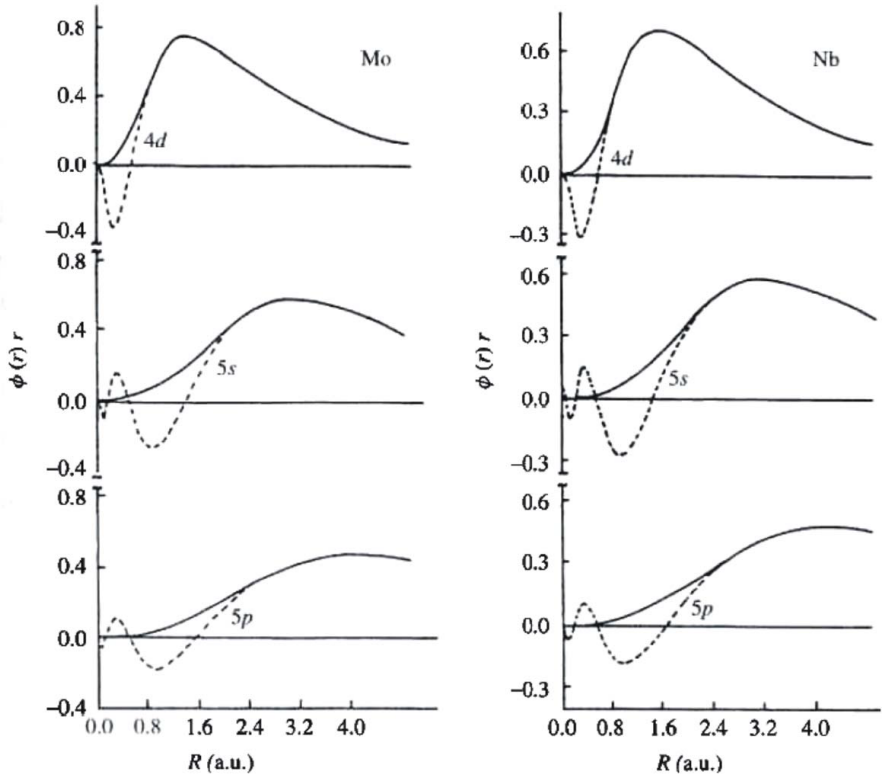

FIGURE 2.5: *The real (dashed curve) and smoothed (full curve) radial parts of the 4d, 5s and 5p orbitals of Mo (left) and Nb (right). The radial distance is expressed in atomic units, i.e. in terms of the Bohr radius* $a_B = 0.529$ *Å. [25]*

2.6.5 Projector augmented waves

Another method used to reduce the computational cost of electron-ion interaction in DFT, is the projector augmented wave (PAW) method, developed by P. E. Blöchl [41].

It is closely related to the PP method, since the aim is still to distinguish between the oscillating part of the orbitals close to the core and the smooth part of the orbitals further away. In contrast to the PP approach, the all-electron character of the wavefunction is conserved. This is done as follows.

First, the true orbitals ψ_i of the isolated atom are obtained from an all-electron calculation. Then, as was the case for PP, the true wavefunctions are transformed into smoother wavefunctions ϕ_i, the so-called *partial waves*. Hereby the constraint is that the true and partial wavefunctions should coincide outside the core region (beyond the cutoff distance r_c). The inverse transformation is achieved by a linear transformation operator $\hat{T}$:

$$\psi_i = \hat{T}\phi_i \ . \tag{2.87}$$

The third step consists of expanding the smooth valence wavefunctions of the electrons, the atom being placed in the vicinity of other atoms. This reads:

$$\Phi_i = \sum_i c_i \phi_i \ . \tag{2.88}$$

The true wavefunction is obtained by the transformation with $\hat{T}$:

$$\Psi_i = \hat{T}\left(\sum_i c_i \phi_i\right) = \sum_i c_i \psi_i \ . \tag{2.89}$$

The PAW method can furthermore be formulated using projectors p_i that operate only in the core region, within the radius r_c. The definition of the projectors is:

$$\langle p_i | \phi_j \rangle = \delta_{ij} \ . \tag{2.90}$$

They can be utilized to rewrite the operator $\hat{T}$ as:

$$\hat{T} = 1 + \sum_j \left(|\psi_j\rangle - |\phi_j\rangle \right) \langle p_j| \ . \tag{2.91}$$

Indeed, inserting this expression in Equation 2.87 and employing Equation 2.90, gives:

$$|\psi_i\rangle = \hat{T}|\phi_i\rangle = |\phi_i\rangle + \sum_j \left(|\psi_j\rangle - |\phi_j\rangle \right) \delta_{ij} \ , \tag{2.92}$$

which is consistent. Consequently, the true electron wavefunction in a system can be written:

$$|\Psi_i\rangle = \hat{T}|\Phi_i\rangle = |\Phi_i\rangle + \sum_j \left(|\psi_j\rangle - |\phi_j\rangle\right) \langle p_j|\Phi\rangle \ . \tag{2.93}$$

According to this expression, the all-electron wavefunction is reconstructed from the smooth pseudowavefunction by correcting for the differences between the true orbitals and the partial waves of the atoms. This is how the PAW method retains the all-electron character of the wavefunctions. As a result, the PAW method is generally more accurate than the PP method.

In practice, the partial waves are again expanded in a basis of planewaves. This basis is truncated at an appropriate cutoff energy E_{cut}. A lower cutoff energy can be selected in the PAW method compared with the PP method [27]. Because of the clear advantages of the PAW method over the PP method, PAW potentials are used throughout this thesis.

2.7 Software packages

We have seen that DFT can be used to reduce the many-body problem. Still, the KS equations are to be solved self-consistently and a sufficiently large basis set has to be selected, as well as an appropriate supercell to implement more complex systems. So, DFT is implemented numerically in a wide variety of software packages, such as ABINIT, Gaussian, Quantum ESPRESSO, SIESTA, VASP, WIEN2k etc. These differ in several aspects, i.a. the choice of basis functions, PPs or PAWs and algorithms used for diagonalization of the KS Hamiltonian. All results presented in this thesis have been obtained using VASP. This is why we will limit our discussion to VASP. We refer to the VASP manual and an article by G. Kresse and J. Furthmüller (collaborators in the VASP project), the main sources for this section, for further reading [39, 42].

2.7.1 VASP

2.7.1.1 Overview of VASP

The Vienna Ab-initio Simulation Package (VASP) is a commercial software package developed at the University of Vienna. The code is written in the Fortran language.

In VASP, several approaches to solve many-body problems are implemented, the main methods being DFT, the HF approximation, and the GW approximation (a method originating from many-body perturbation theory). DFT in VASP is aimed at finding solutions of the KS equations in a self-consistent (SC) iteration. Several approximations of the XC functional are available, such as LDA and GGA (e.g. the PBE functional). Additionally, hybrid functionals can be selected, more specifically the HSE functional, that mixes HF exchange into the XC functional in the short range. Calculations involving the HF approximation are implemented via the HF-Roothaan equations. If required, spin-orbit coupling can be included. Practically, the wavefunctions and potentials are expanded in a planewave basis set. Electron-ion interactions can either be treated using PPs (specifically ultrasoft Vanderbilt PPs) or PAWs. We have opted for the latter method, because it is generally more accurate and requires a smaller basis set, as we have mentioned in Section 2.6.5. In VASP, PAWs for all elements of the periodic system are included. PAWs for DFT calculations are generated within a certain approximation to the XC functional. For hybrid calculations by means of the HSE functional, PAWs with PBE-character are to be selected. Moreover, the VASP user has the choice - for most elements - of which electrons are treated as valence electrons. The recommeded choices for accurate calculations can be found in the VASP manual.

In the self-consistent solution of the KS equations, several methods for the diagonalization of the KS Hamiltonian can be employed. The three main methods in VASP are (i) the *blocked Davidson algorithm*, (ii) the *conjugate gradient algorithm* (CGA) and (iii) the *residual minimization method by direct inversion in the iterative subspace* (RMM-DIIS). The efficiency of the self-consistency cycle can be improved by *charge density mixing*, i.e. taking a combination of previous output charge densities to create the input charge density for a new iteration step. Geometry optimization of the ionic stucture is also executed in an iterative way. The geometry is considered optimized or relaxed if the forces on all ions are below the selected convergence criterion. Within each step of the relaxation, the electronic structure has to be calculated in a self-consistency cycle. Subsequently, the forces can be calculated using the Hellmann-Feynman theorem, as we have explained in Section 2.5. The most reliable method for relaxation in VASP is based on a conjugate gradient algorithm. In the first step, the ionic positions are altered in the direction of the forces acting on them. This is a so-called line minimization. Similarly,

the cell shape is changed in the direction of the calculated stress. The forces, stress tensor and total energy are recalculated, which concludes the trial step. For the corrector step, a third-order interpolation is performed to further approximate the minimum in total energy. Again, the forces on the ions are calculated. In case any force on an ion in the system exceeds the convergence criterion, the procedure is repeated. The new search direction are conjugated to the previous search directions.

To meet the computational demands, VASP allows for parallelization, i.e. subtasks are divided over multiple CPUs. Parallelization in VASP can be achieved both w.r.t. energy bands and k-points. Communication between the CPUs that partake is based on the Message Passing Interface (MPI). Additionally, we have found that the hybrid functional raises the computational cost of the calculation considerably, compared with other functionals, e.g. the PBE functional. Several reasons can be identified. First, the HF exchange included in the hybrid functional requires the evaluation of two-electron integrals. Moreover, it is to be calculated using the orbitals instead of the density. The wavefunctions are - according to the Bloch theorem - products of functions with the same periodicity as the lattice and planewaves. That is why, contrary to the density, the wavefunctions do not possess the full periodicity of the lattice. Accordingly, in reciprocal space, the full first BZ instead of the IBZ is to be sampled. This increase in computational cost can be partially overcome by carrying out a uniform reduction of the k-point mesh used for the evaluation of the HF kernel. As the VASP manual points out, this option should be used with vigilance, especially for doped systems. Finally, scaling of the calculation with the system size also contributes to the difference in computational cost between pure DFT and the hybrid method. It has been reported that the scaling performance of hybrid calculations is poor in comparison with the scaling of pure DFT [43].

2.7.1.2 Input and output

The four main input files of VASP that are to be modified by the user are (i) the INCAR file, (ii) the POSCAR file, (iii) the KPOINTS file and (iv) the POTCAR file. We will discuss them one by one. The INCAR file contains parameters that determine which calculation is executed and how it is executed. This includes the choice of the XC functional, the amount of HF mixing in the HSE functional, the cutoff energy of

the planewave basis set etc. Furthermore, convergence criteria, such as those used in the electronic SC iteration and structural relaxation are specified in the INCAR file. In addition, the desired output can be adapted. The default output consists of the optimized ionic positions and the related forces and stress, the KS eigenvalues for all k-points of the mesh, the KS orbitals and the charge density. The latter two can be used in a new calculation on the same system to reach convergence in the electronic SC cycle more easily. Extra quantities that can be output are i.a. the density of states, the electrostatic and total potential and the dielectric function.

In the POSCAR file, the ionic positions are listed, either in terms of the lattice parameters or in Cartesian coordinates. Similarly, the KPOINTS file contains the k-points used for the integration over the BZ. Either these k-points are listed explicitly in the KPOINTS file or the dimensions of the mesh needed to generate a Monkhorst-Pack grid are specified. The former method is required for the calculation of a band structure along specific lines in the BZ. Finally, the POTCAR file comprises the PPs or PAWs of the elements present in the INCAR file.

Chapter 3

Structural, electronic and optical properties of CIGS

3.1 Introduction

Due to technological interest in thin-film photovoltaic cells, $CuIn_{1-x}Ga_xSe_2$ (CIGS) has been the subject of both experimental and theoretical research. One of the early landmark, theoretical articles was written by J. E. Jaffe and A. Zunger [3]. In this article the electronic structure of several ternary chalcopyrite semiconductors, including $CuInSe_2$ (CIS) and $CuGaSe_2$ (CGS), is calculated by using the LDA functional containing Ceperley-Alder correlation. This particular correlation functional is non-analytic and is obtained as a result of Monte-Carlo simulations. Naturally, the band gaps obtained for CIS and CGS are heavily underestimated w.r.t. experimental results. In this chapter, we will show how (CIGS) materials can be studied using a hybrid functional. The main reason to apply a hybrid functional is to overcome the band gap problem in DFT. The amount of HF mixing (or the range-separation parameter) can be tuned to achieve the best possible agreement with experimental results. The result can in turn be used for calculations that rely critically on the band gap, e.g. band alignment and defect calculations. We will distinguish between structural, electronic and optical properties of CIGS and systematically compare results obtained with PBE and HSE functionals. Spin-orbit coupling is not taken into account. This kind of calculation requires solving

of the Kohn-Sham equations for the double number of bands as compared to the non-spin-orbit coupled case. We will demonstrate that non-spin-orbit coupled calculations prove satisfactory for the main topics of this thesis, namely band alignment and defect properties of CIGS compounds.

3.2 Crystal structure

The structural properties of the chalcopyrite structure have been established in Chapter 1, Section 1.1. The atomic configurations of the constituent atoms of CIGS are tabulated in Table 3.1. The underlined orbitals in Table 3.1 are treated as valence electrons in projector augmented wave (PAW) potentials used throughout the thesis. For integration over the Brillouin zone, a Γ-centered $6 \times 6 \times 6$ Monkhorst-Pack grid is found to yield convergence on the total energy of less than 1 meV for a primitive unit cell containing 8 atoms. The Monkhorst-Pack grid is an equidistant grid [40]. The energy cutoff for the plane-wave basis is chosen to be 500 eV for convergence within $\sim$ 1 meV. Finally, in the self-consistent iteration, convergence of the total energy to 0.1 meV is imposed.

In order to simulate CIGS compounds with varying Ga content, x, we make use of the $1 \times 1 \times 2$ supercell containing 16 atoms. In this way, five possible Ga contents 0 (CIS), 0.25, 0.5, 0.75 and 1 (CGS) are considered. This choice enables to study varying Ga-to-In ratio without resorting to an exceedingly large supercell. It results in six CIGS compounds, since for $x = 0.5$ there are two inequivalent possible structures: one with the sequence In-Ga-In-Ga (denoted as '$x = 0.5$ (a)') and the other with In-In-Ga-Ga (denoted as '$x = 0.5$ (b)') in subsequent planes. They are shown in Figures 3.1 (a) and (b). For the $1 \times 1 \times 2$ supercell containing 16 atoms a $4 \times 4 \times 4$ k-point mesh is used to give convergence of the total energy of $\sim$ 2 meV (i.e. $\sim$ 1 meV per 8 atoms). The atomic positions of all these compounds are relaxed using a *conjugate-gradient algorithm* (CGA), discussed in Section 2.7.1 of Chapter 2. The maximum allowed force for the

Atom	Atomic configuration	Atomic number	Block	Group
Cu	[Ar] $\underline{3d^{10}4s^{1}}$	29	d	I
Ga	[Ar] $\underline{3d^{10}4s^{2}4p^{1}}$	31	p	III
In	[Kr] $\underline{4d^{10}5s^{2}5p^{1}}$	49	p	III
Se	[Ar] $\underline{3d^{10}4s^{2}4p^{4}}$	34	p	VI

TABLE 3.1: *The atomic configurations of the constituent atoms of CIGS.*

relaxation of the structures that are studied in this chapter is 30 meV/Å. All possible degrees of freedom are optimized; this comprises the cell shape and volume and the ionic positions. We compare the results of relaxation through the PBE and HSE06 functional.

The space symmetry and lattice parameters obtained using the PBE and HSE06 functional are summed up in Tables 3.2 and 3.3. Only the compounds CIS (x=0) and CGS ($x = 1$) have kept the chalcopyrite space symmetry I$\bar{4}$2d. Compounds with $x = 0.25$ and $x = 0.75$ are found to adopt the simple tetragonal symmetry P$\bar{4}$ (No. 81). For $x = 0.5$ there are two possible configurations, which yield different space symmetries. The configuration In-Ga-In-Ga (a) leads to body-centered tetragonal space symmetry I$\bar{4}$, while In-In-Ga-Ga (b) results in an orthorhombic structure P222$_1$ (No. 17). The changes in symmetry can be intuitively understood by the difference in atomic radii of In (1.67 Å) and Ga (1.53 Å) [44]. For instance, the loss of body-centering in case $x = 0.25$ and $x = 0.75$ is schematically shown in Figure 3.2. For the compounds that have the chalcopyrite space symmetry, one can also calculate the anion displacement (u) of the Se

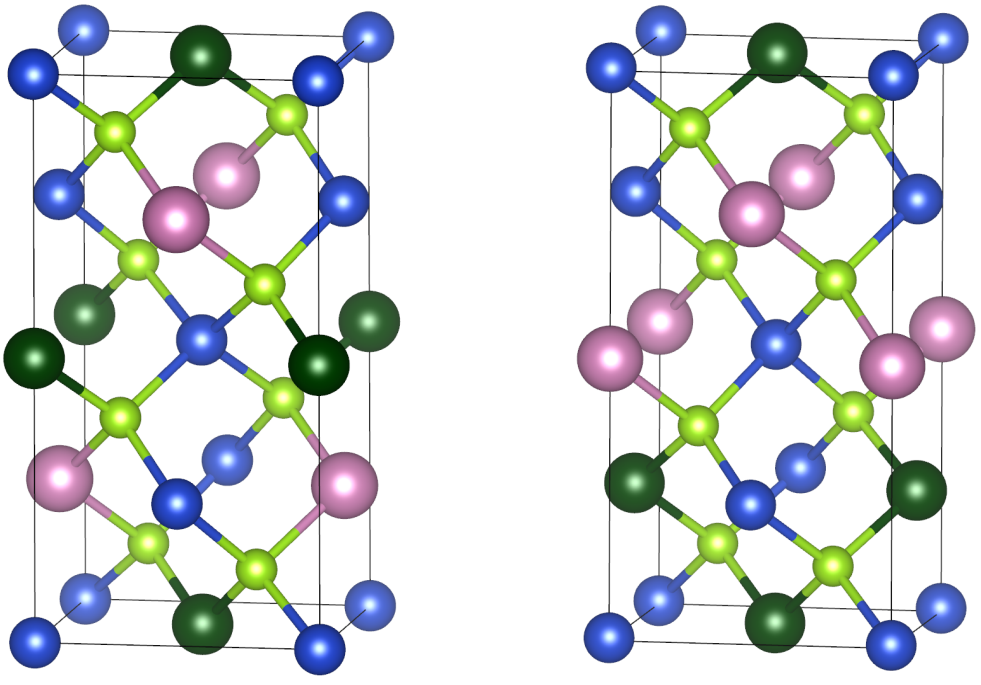

(a) In-Ga-In-Ga (b) In-In-Ga-Ga

FIGURE 3.1: *Two possible configurations for Ga content of $x = 0.5$. The color code is: Cu (blue), In (pink), Ga (dark green) and Se (bright green).*

ions, which has been introduced in Section 1.1 of Chapter 1. The lattice parameters for CIS and CGS are given in Table 3.4 and compared with experimental results. One can observe that relative deviations from the experimental values are small. The theoretical values for a and c are consistently larger than experimental results. They are more accurately described by the HSE06 functional in comparison with the PBE functional. Experimental values may also be slightly reduced due to strain present in experiment, related to the growth conditions.

It should be noted that the deviation of the space structures from $I\bar{4}2d$ is rather small compared to the lattice parameters. For instance, the atomic displacement that leads to the loss of body-centering for compounds with $x = 0.25$ and $x = 0.75$ is in the order of 0.062 to 0.066 Å, cfr. Figure 3.2. The lowering in symmetry that is found theoretically has not been reported in e.g. X-ray diffraction experiments [45]. We will try to explain our understanding of what causes this discrepancy. In DFT, there is an inevitable need of periodicity that is not compatible with the randomization of an alloy. The implementation of alloying in a $1 \times 1 \times 2$ supercell can impose additional conditions on the system that lead to the slight change in symmetry. In order to implement more disorder, one would have to resort to large systems that are currently hardly attainable with hybrid functionals. Also, our DFT calculations predict the crystal structure at zero temperature. In conclusion, it can be expected that in a disordered alloy at nonzero temperature the extra conditions 'wash out'.

Ga content 'x'	Space symmetry (Hermann-Mauguin notation)	a (Å)	c (Å)
0	$I\bar{4}2d$ (No. 122, BCT)	5.881	11.801
0.25	$P\bar{4}$ (No. 81, TET)	5.825	11.703
0.5 (a)	$I\bar{4}$ (No. 82, BCT)	5.776	11.552
0.5 (b)	$P222_1$ (No. 17, ORT)	a=5.761, b=5.788	11.576
0.75	$P\bar{4}$ (No. 81, TET)	5.726	11.420
1	$I\bar{4}2d$ (No. 122, BCT)	5.680	11.260

TABLE 3.2: *Structural properties of CIGS compounds calculated with the PBE functional.*

Ga content 'x'	Space symmetry (Hermann-Mauguin notation)	a (Å)	c (Å)
0	$I\bar{4}2d$ (No. 122, BCT)	5.832	11.735
0.25	$P\bar{4}$ (No. 81, TET)	5.787	11.587
0.5 (a)	$I\bar{4}$ (No. 82, BCT)	5.742	11.436
0.5 (b)	$P222_1$ (No. 17, ORT)	a=5.735, b=5.750	11.461
0.75	$P\bar{4}$ (No. 81, TET)	5.696	11.283
1	$I\bar{4}2d$ (No. 122, BCT)	5.652	11.119

TABLE 3.3: *Structural properties of CIGS compounds calculated with the HSE06 functional.*

Parameter	CIS	CGS
a_{exp} (Å)	5.784	5.614
a_{calc}^{PBE} (Å)	5.881 (+1.7 %)	5.680 (+1.2 %)
a_{calc}^{HSE} (Å)	5.832 (+0.8 %)	5.652 (+0.7 %)
c_{exp} (Å)	11.616	11.030
c_{calc}^{PBE} (Å)	11.801 (+1.6 %)	11.260 (+2.1 %)
c_{calc}^{HSE} (Å)	11.735 (+1.0 %)	11.119 (+0.8 %)
u_{exp}	0.224	0.250
u_{calc}^{PBE}	0.223 (-0.4 %)	0.247 (-1.2 %)
u_{calc}^{HSE}	0.229 (+2.2%)	0.253 (+1.2 %)

TABLE 3.4: *Comparison of lattice parameters calculated with HSE06 and PBE and experimental results [46]. For the calculated values the relative deviation from the experimental results is given.*

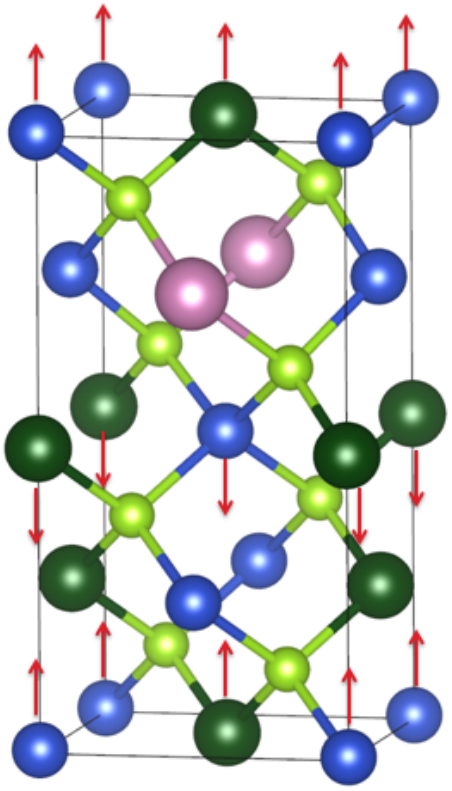

FIGURE 3.2: *The ion displacement for $x = 0.75$ due to different size of In and Ga is depicted with red arrows. As a result body-centering is lost. The effect is exaggerated for clarity. The displacement indicated by the arrows is in fact 0.062 Å using the PBE functional and 0.066 Å for the HSE06 functional.*

3.2.1 Vegard's law for structural parameters

An approximate model that describes lattice parameters of a solid solution is given by *Vegard's law*. This law states that the lattice parameters of a solid solution are linear combinations of the lattice parameters of the compounds limiting the homogeneity range. The coefficients of the linear combination depend on the concentration of the elements. In CIGS the limiting compounds are CIS ($x = 0$) and CGS ($x = 1$). Vegard's law yields the following set of equations for both lattice parameters a and c:

$$\begin{cases} a(x) = a(0) \cdot (1 - x) + a(1) \cdot x \\ c(x) = c(0) \cdot (1 - x) + c(1) \cdot x \ . \end{cases} \tag{3.1}$$

In case the structure does not follow Vegard's law an extra term can be included containing *bowing parameter* B. This adaptation of Vegard's law looks as follows:

$$\begin{cases} a(x) = a(0) \cdot (1-x) + a(1) \cdot x - B \cdot x(1-x) \\ c(x) = c(0) \cdot (1-x) + c(1) \cdot x - B' \cdot x(1-x) \ . \end{cases} \tag{3.2}$$

The lattice parameters a and c are plotted in Figure 3.3 as a function of Ga content, x, calculated with PBE and HSE06. For results obtained with PBE, there is more deviation from Vegard's law as given by Formula 3.1 than for those calculated with HSE06. Thus, it is useful to introduce bowing, respectively 0.0170 Å and -0.0844 Å for lattice parameters a and c. On the other hand, for HSE06 results, bowing is negligibly small, so Vegard's law is valid. Compliance with Vegard's law for lattice parameters in CIGS is confirmed by experimental work by Li et al. using transmission electron microscopy [47].

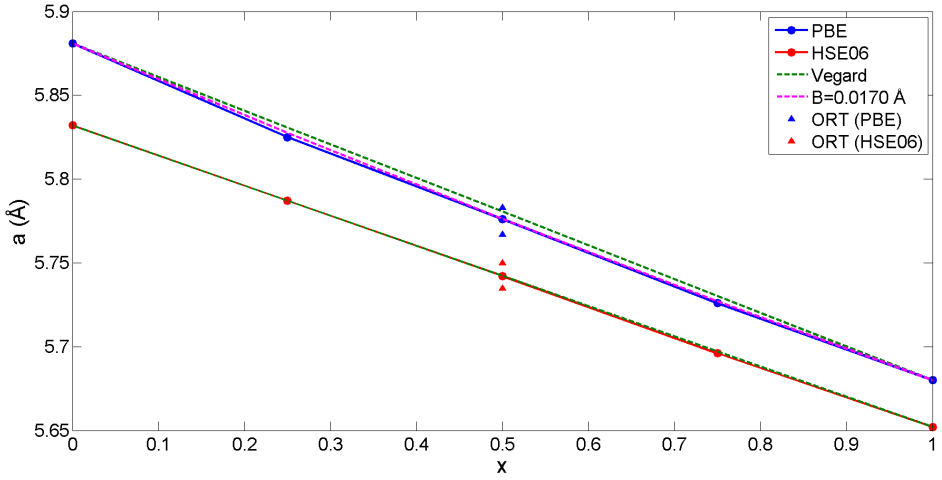

(a) Lattice parameter a

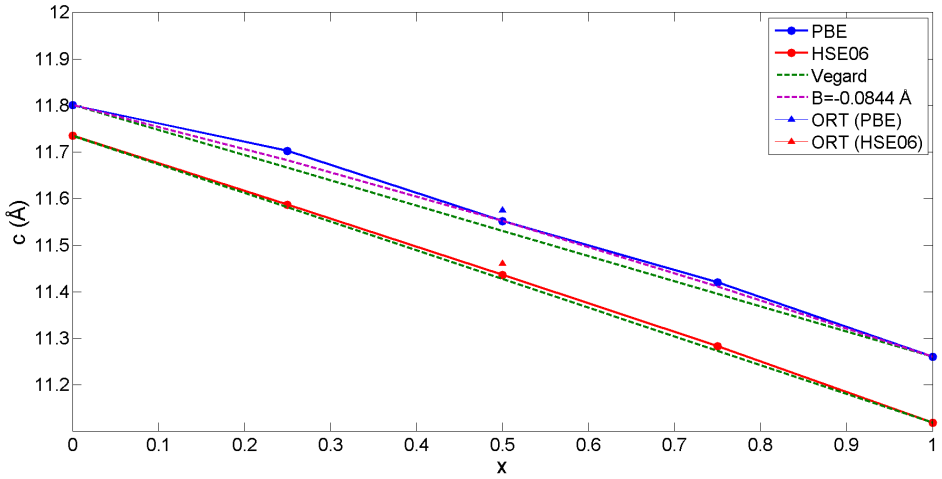

(b) Lattice parameter c

FIGURE 3.3: *Lattice parameters of CIGS as a function of Ga content (x), calculated with PBE (blue) and HSE06 (red). A fit is performed with Vegard's law (dashed, green) and Vegard's law with bowing, B, included (dashed, purple). The fits do not include the orthorhombic (ORT) structure obtained for* $x = 0.5$ *in the In-In-Ga-Ga configuration (triangles).*

3.2.2 Mixing enthalpy

Another major question for an alloy is whether the compounds will mix or segregate into separate phases. It is important for CIGS photovoltaic cell devices that the alloying is homogeneous. Theoretical work by C. D. R. Ludwig et al., a combination of a *cluster expansion method* [1] and Monte Carlo simulations for randomization, suggests that there is tendency for phase segregation in CIGS at low temperatures [48]. It is an experimental fact that there is no phase segregation in actual CIGS absorber layers [12]. Ludwig et al. explain this by the high temperature (typically $\sim$ 500 to 600 °C) at which CIGS layers are produced. They argue that the mixing that is established at higher temperature freezes upon cooling.

Using DFT, we can also assess the tendency for phase segregation of CIGS. For this purpose we can study the *mixing enthalpy* ΔH of mixed systems. This is defined as:

$$\Delta H = E\left(\mathrm{CuIn_{1-x}\ Ga_xSe_2}\right) - (1-x)\ E\left(\mathrm{CuInSe_2}\right) - x\ E\left(\mathrm{CuGaSe_2}\right)\ , \tag{3.3}$$

where E denotes the total energy. The mixing enthalpies obtained from calculations with functionals PBE and HSE06 are tabulated in Table 3.5. We find that the mixing enthalpy is positive, meaning that energy is needed to mix CIS and CGS. Yet, the mixing enthalpy per mixing atom is in the order of 10 meV to 14 meV. Mixing atoms are those atoms that have to mix to obtain a homogeneous alloy, in the case of CIGS these are In and Ga. Since 1 meV corresponds to $\sim$ 11.6 K, we conclude that there is no phase segregation at temperatures of $\sim$ 170 K and above.

Functional	$x = 0.25$	$x = 0.5$	$x = 0.75$
PBE	13.6	13.2	14.4
HSE06	11.2	10.0	12.4

TABLE 3.5: *Mixing enthalpy ΔH in units of meV per mixing atom obtained with PBE and HSE06 functionals.*

[1] This method consists of an expansion of the formation energy of an atomic configuration into different contributions. These energy contributions are respectively due to single atoms, pairs of atoms a.s.o. The coefficients of the expansion are calculated using a first-principles method, usually DFT.

3.3 Electronic structure

We proceed by studying the electronic structure of $CuIn_{1-x}Ga_xSe_2$ compounds. The computational details of the calculations in this section are very similar to those in the previous section. Integration over the Brillouin zone is performed on a $6 \times 6 \times 6$ Monkhorst-Pack grid and the energy cutoff for the plane wave basis is set to 500 eV. The integration includes occupancies $f_{n\mathbf{k}}$, that are distributed according to the Fermi-Distribution and are thus discontinuous at the Fermi level. To facilitate the convergence of the integration w.r.t. the number of k-points, the step function can be replaced by a smooth function, a method called *smearing*. We use Gaussian smearing with a width of 0.05 eV, since this method is particularly suited for semiconductors [42]. The symmetric primitive lattice vectors and corresponding reciprocal vectors of the body-centered tetragonal crystal system are [49]:

$$\begin{cases} \mathbf{a}'_1 = \left(-\frac{a}{2}, \frac{a}{2}, \frac{c}{2}\right) \ , \ \mathbf{b}'_1 = 2\pi \left(0, \frac{1}{a}, \frac{1}{c}\right) \\ \mathbf{a}'_2 = \left(\frac{a}{2}, -\frac{a}{2}, \frac{c}{2}\right) \ , \ \mathbf{b}'_2 = 2\pi \left(\frac{1}{a}, 0, \frac{1}{c}\right) \\ \mathbf{a}'_3 = \left(\frac{a}{2}, \frac{a}{2}, -\frac{c}{2}\right) \ , \ \mathbf{b}'_3 = 2\pi \left(\frac{1}{a}, \frac{1}{a}, 0\right) \ . \end{cases} \tag{3.4}$$

Then one can define the following special k-points:

$$\begin{cases} Z : (0.5, 0.5, -0.5) \\ \Gamma\text{:} \ (0, 0, 0) \\ P : (0.25, 0.25, 0.25) \ , \end{cases} \tag{3.5}$$

in the convention formulated by W. Setyawan and S. Curtarolo [49]. The Brillouin zone of the primitive unit cell with lattice parameters 3.4 is shown in Figure 3.4.

Following J. E. Jaffe and A. Zunger [3], for the $1 \times 1 \times 2$ supercell we transform the lattice parameters and corresponding reciprocal vectors to:

$$\begin{cases} \mathbf{a}_1 = (a, 0, 0) \ , \ \mathbf{b}_1 = 2\pi \left(\frac{1}{a}, 0, -\frac{1}{c}\right) \\ \mathbf{a}_2 = (0, a, 0) \ , \ \mathbf{b}_2 = 2\pi \left(0, \frac{1}{a}, -\frac{1}{c}\right) \\ \mathbf{a}_3 = (a, a, c) \ , \ \mathbf{b}_3 = 2\pi \left(0, 0, \frac{1}{c}\right) \end{cases} \tag{3.6}$$

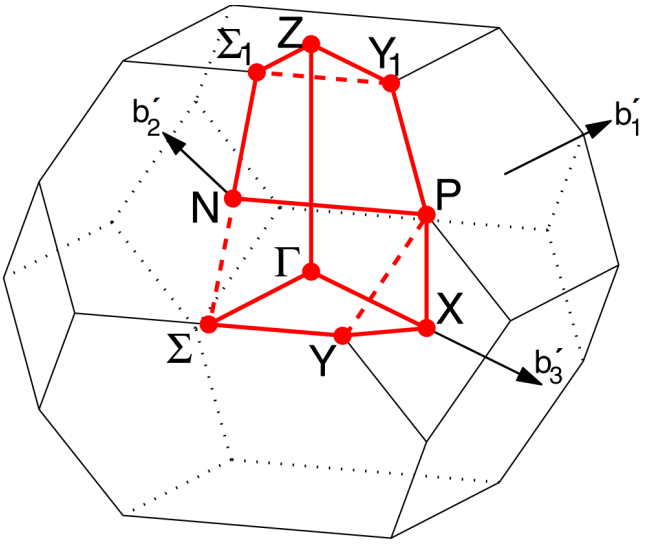

FIGURE 3.4: *The first Brillouin zone of the body-centered tetragonal crystal system in case $c > a$. [49]*

The equivalent special k-points of Formula 3.5 for the $1 \times 1 \times 2$ supercell and in terms of the reciprocal vectors in Formula 3.6 are:

$$\begin{cases} Z : (0, 0, 0.5) \\ \Gamma\text{: } (0, 0, 0) \\ P : (0.5, 0.5, 0) \ . \end{cases} \tag{3.7}$$

Band structure calculations are performed along the line Z-Γ-P. The density of states (DOS) is calculated using a denser Γ-centered Monkhorst-Pack grid, namely $8 \times 8 \times 8$.

3.3.1 Band gap

CIGS compounds are semiconductors with a direct band gap. The direct nature of the band gap will be demonstrated by means of the dielectric function in a further section. The direct band gap results in high optical absorption, applicable for photovoltaics. We need to stress that the band gaps calculated in this section are not necessarily equal to the optical band gaps, that excited electrons feel. The reason is that excitonic interaction, i.e. interaction between electrons and holes, is not taken into account. Under the influence of a Coulomb-like attraction the optical band gap is smaller than the calculated electronic band gap.

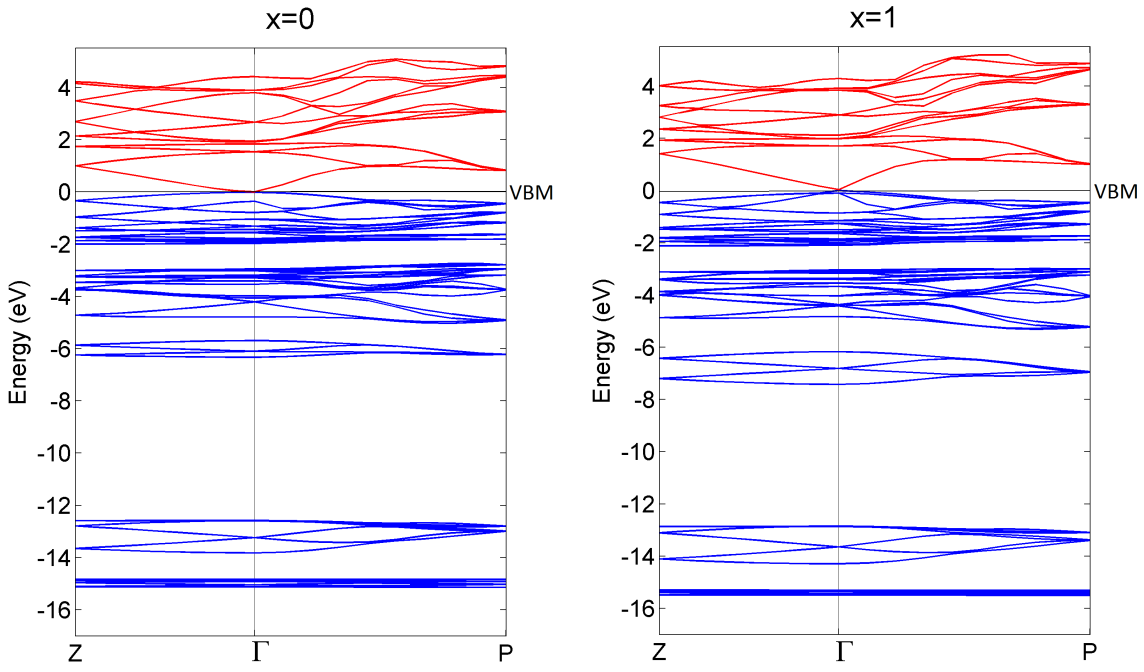

(a) CIS ($x = 0$) (b) CGS ($x = 1$)

FIGURE 3.5: *Band structures calculated with the Perdew-Burke-Ernzerhof functional. The valence band maxima (VBM) are set to zero, meaning that the band structures are not yet aligned w.r.t. eachother. Valence bands are colored in blue and conduction bands in red.*

As was mentioned in the introduction, pure DFT functionals, like LDA or GGA, lead to a significant underestimation of the band gap. This holds true in CIGS compounds. In Figure 3.5 the band structures of CIS ($x = 0$) and CGS ($x = 1$), as calculated with PBE (a type of GGA), are shown. The band gaps are respectively 0.02 eV and 0.04 eV. The band gaps of all studied CIGS compounds are to be found in Table 3.6. Experimental values are 1.0 eV for CIS and 1.7 eV for CGS [50]. The correspondence with the experimental band gaps can be greatly improved by replacing the PBE functional with a hybrid functional, more specifically the HSE06 functional. The band structures of CIS, CIGS with $x = 0.5$ and CGS obtained with this functional are displayed in Figure 3.6. The resulting band gap of CIS is 0.85 eV and that of CGS is 1.37 eV, cfr. Table 3.6. The relative deviations from the experimental values thus amount to 15 % and 19 %. Thus, much better agreement with experiment is found than for band gaps calculated with the PBE functional. For a realistic study of topics discussed further on in this thesis - band alignment of CIGS compounds and impurity studies - it is appropriate to establish a more accurate fit with experimental band gaps. This can be achieved by modifying

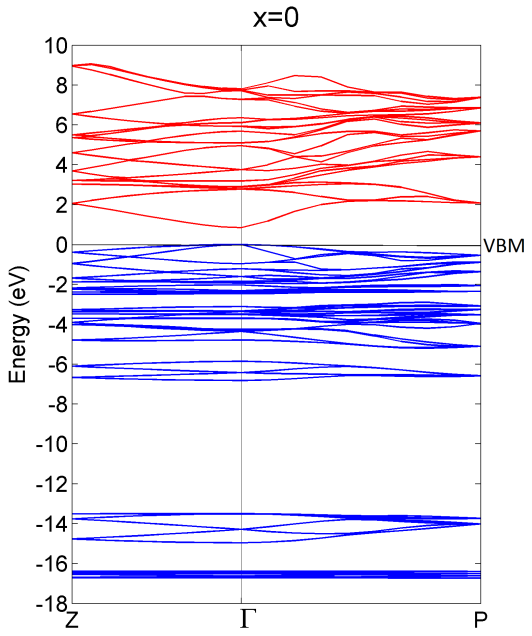

(a) CIS: band structure

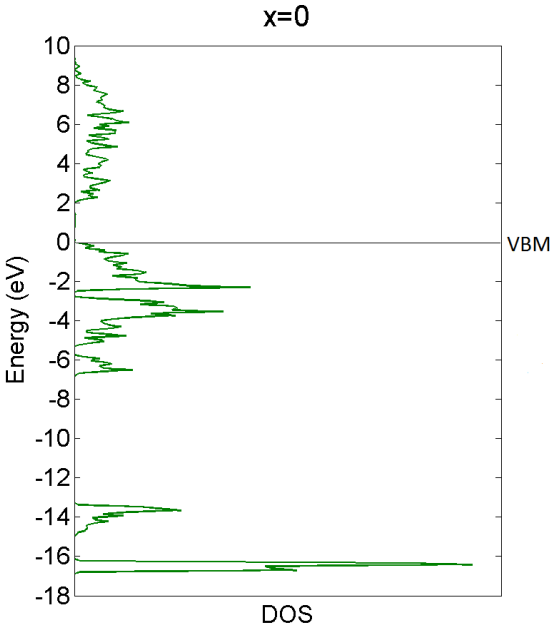

(b) CIS ($x = 0$): DOS

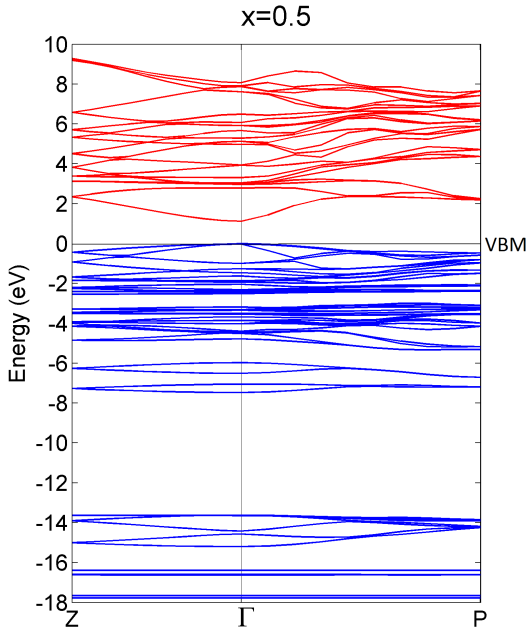

(c) CIGS with $x = 0.5$: band structure

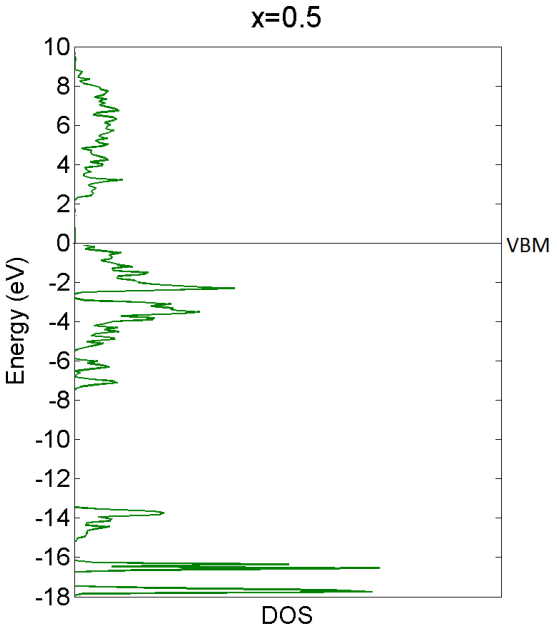

(d) CIGS with $x = 0.5$: DOS

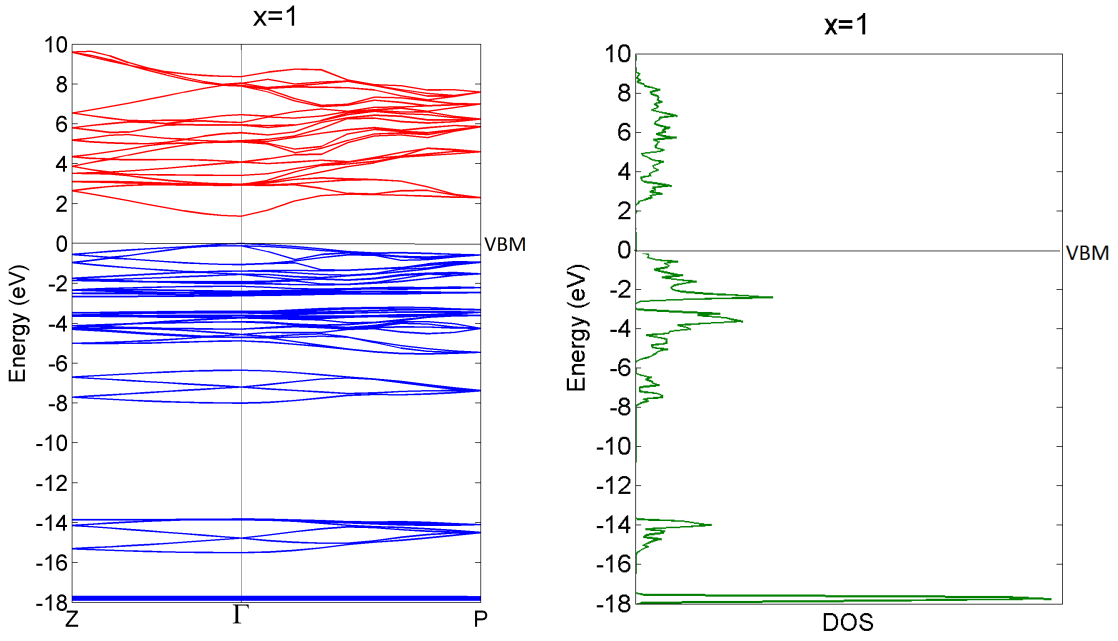

(e) CGS ($x = 1$): band structure

(f) CGS ($x = 1$): DOS

FIGURE 3.6: *Band structures and corresponding density of states (DOS) calculated with the Heyd-Scuseria-Ernzerhof functional. The valence band maxima (VBM) are set to zero, meaning that the band structures are not yet aligned w.r.t. eachother.*

the HSE06 functional by 'tuning' the Hartree-Fock mixing coefficient α (introduced in Equation 2.61) w.r.t. experimental band gaps [2]. Parameter α has been determined via linear interpolation starting from band gap energies of CIS and CGS calculated with $\alpha = 0.25$ and $\alpha = 0.4$. The values for α for the intermediate alloys are also obtained from those for CIS and CGS by linear interpolation. The result is summed up in Table 3.7. The tuned HSE06 functional will be denoted HSE06$^{(t)}$.

Additionally, in Table 3.6 the effect of spin-orbit coupling (SOC) on the HSE06$^{(t)}$ functional is demonstrated. Given the HSE06$^{(t)}$ functional, it is apparent that spin-orbit coupling reduces the band gap by ~ 0.1 eV. For the purpose of band alignment and impurity calculations we therefore can legitimately omit spin-orbit coupling, since our conclusions are not significantly affected. Including SOC doubles the number of equations to be solved numerically by VASP, so it is computationally restrictive.

[2] Alternatively parameter μ, that determines the range of the interaction could be modified. We found, however, that the band gap is more sensitive to α than to μ.

Functional	$x = 0$	$x = 0.25$	$x = 0.5$	$x = 0.75$	$x = 1$
PBE	0.02	0.02	0.03	0.05	0.04
HSE06	0.85	0.98	1.12	1.24	1.37
HSE06$^{(t)}$	1.00	1.16	1.36	1.52	1.72
HSE06$^{(t)}$+SOC	0.91	1.08	1.27	1.43	1.62

TABLE 3.6: *Band gaps in units of eV calculated with the following functionals: PBE, HSE06 and HSE06$^{(t)}$. In addition, the effect of spin-orbit coupling (SOC) on the band gap is given.*

Ga content, x	α (d.u.)
0	0.2780
0.25	0.2860
0.5	0.2939
0.75	0.3019
1	0.3098

TABLE 3.7: *Hartree-Fock mixing parameter α in the HSE06$^{(t)}$ functional.*

Another important question related to the band gap is if there is bowing as a function of the alloying. This is very similar to Equation 3.8 in the context of the structural parameters. For the band gap energy, E_g, it reads:

$$E_g(x) = E_g(0) \cdot (1 - x) + E_g(1) \cdot x - B \cdot x(1 - x) \ , \tag{3.8}$$

where B is the bowing parameter. The results are depicted in Figure 3.7. We find that in the electronic structures obtained with hybrid functionals, only a small amount of bowing of the band gap is present. For HSE06, bowing is $B = -0.03$ eV and for HSE06$^{(t)}$, $B = 0.06$ eV. Experimental data are not conclusive regarding bowing of the band gap energy. A variery of values can be found, ranging from -0.07 eV to 0.24 eV [51].

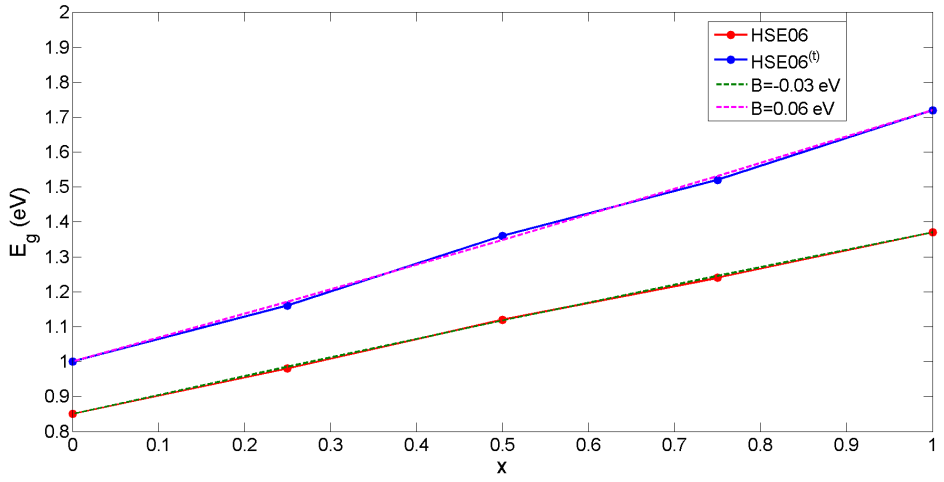

FIGURE 3.7: *The band gap energies calculated with the HSE06 (red curve) and HSE06*$^{(t)}$ *(blue curve) as a function of Ga content, x. A fit including bowing is plotted, for HSE06 it is* $B = -0.03$ *eV and for HSE06*$^{(t)}$ $B = 0.06$ *eV.*

3.3.2 Band mass

A property directly related to the band structure is the *Band mass* (or *effective mass*). The band mass m_b of charge carriers is defined in a quadratic approximation to the actual dispersion:

$$E(k) = E_0 \pm \frac{\hbar^2 k^2}{2m_b} \ , \tag{3.9}$$

for the dispersion around Γ. E_0 is the energy of the band at Γ. The + sign is to be selected in case of a conduction band and the - sign for a valence band. The band mass is directly related to the *mobility* μ of the charge carriers as:

$$\mu = \frac{e\tau}{m_b} \ , \tag{3.10}$$

where e is the elementary charge and τ is the collision time [52]. The mobility of the charge carriers plays an important role in photovoltaic devices.

CIGS is an anisotropic material and consequently we distinguish between band masses in the (100), equivalent with (010) for the tetragonal crystal system, and (001) directions (in the Cartesian coordinate system). The band masses in the (100) direction will be denoted $m_b^{\parallel}$ and those in the (001) direction as $m_b^{\perp}$. We study the three upper valence bands, referred to as $v1$ to $v3$ for hole band masses and the lowest conduction band $c1$

for electrons. The analysis is carried out for CIS, CIGS with $x = 0.5$ and CGS. Their dispersion around Γ is to be found in Figure 3.8.

We have found that the second order coefficient, from which the band mass is obtained, is converged in the sixth order fit. Therefore, the dispersion is fitted with a sixth order polynomial of the wavevector. The fit is carried out using the 'polyfit' function in the mathematical programming language MATLAB. As is shown in Figure 3.8 (b), the dispersion in either dimension is mirrored around Γ to allow for a more accurate fit. The reason is that the constraint on the first derivative at 0 is included. The figure shows the instance of the lower conduction band, $c1$ of CIS. The interval of choice for the fit is 0.1 Å^{-1} around Γ (except when explicitly stated otherwise). The irreducible Brillouin zone (IBZ) extends to 0.54 Å^{-1} for CIS and 0.56 Å^{-1} for CGS in the (100) direction. In the (001) it measures 0.27 Å^{-1} in case of CIS to 0.28 Å^{-1} in case of CGS.

The band masses of the bands that have been studied, are listed in Table 3.8. All band masses are below 1, which is beneficial for the mobility of the charge carriers. The most relevant band masses for the mobility in CIGS photovoltaic devices are those related to the top valence band $v3$ (for holes) and the bottom conduction band $c1$ (for electrons). With the exception of $v1$ and $v3$ for $x = 0.5$ and 1, the anisotropy between the $\parallel$ and $\perp$ directions is limited. C. Persson has compared band structures calculated with and without inclusion of spin-orbit coupling (SOC) [53]. His calculations use a GGA functional mixed with Coulomb interaction through the GGA+U^{SIC} method, where SIC stands for self-interaction correction. He demonstrates that the dispersion of the top valence band in CIGS compounds is significantly influenced by spin-orbit coupling. For instance, neglecting SOC, he finds the hole band mass of the top valence band in the (100) direction in CIS to be 0.79, compared to 0.14 when including SOC. Our result is $m^{\parallel}_{v3}(\text{CIS}) = 0.683$.

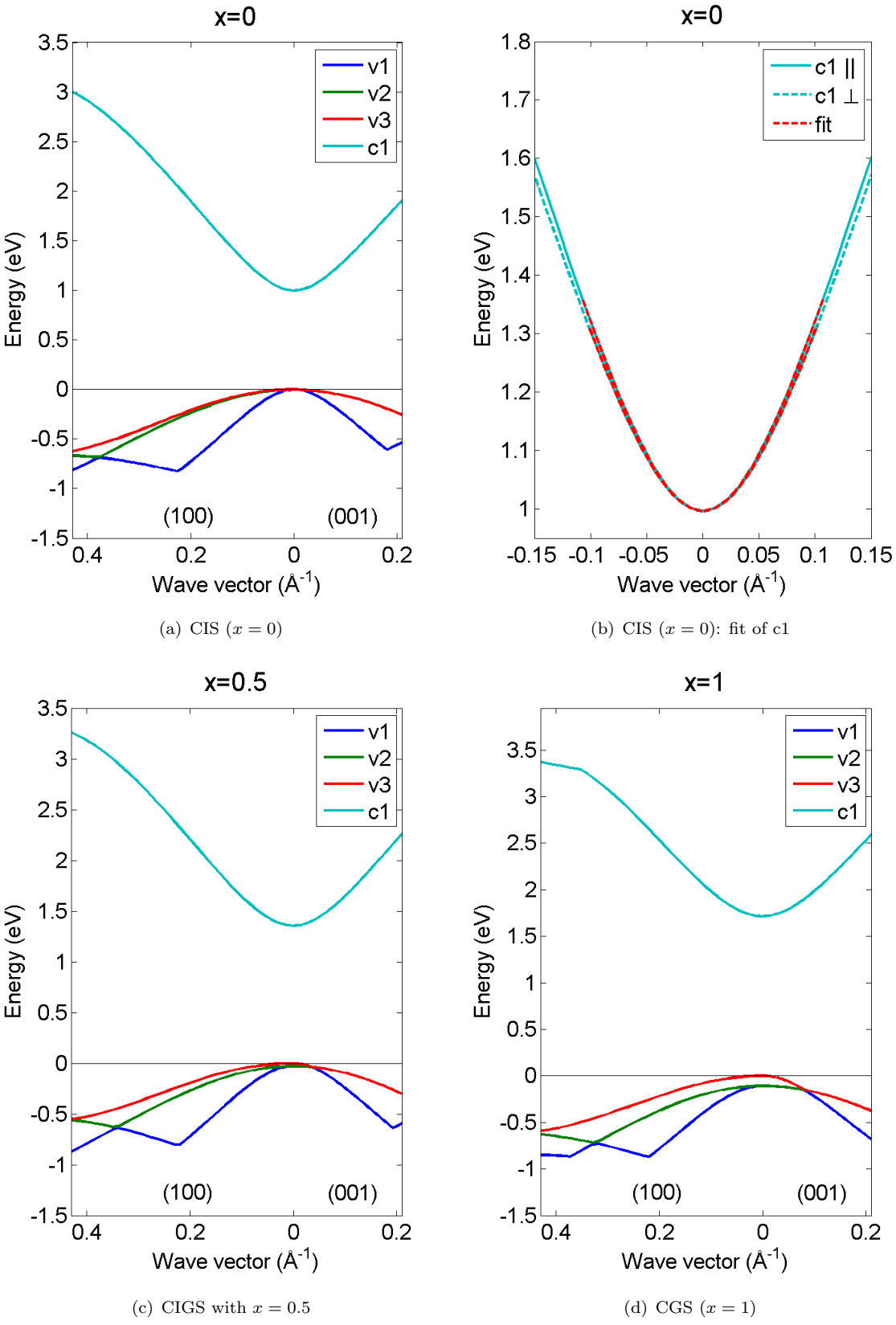

(a) CIS ($x = 0$)

(b) CIS ($x = 0$): fit of c1

(c) CIGS with $x = 0.5$

(d) CGS ($x = 1$)

FIGURE 3.8: *The bands of CIS (a), CIGS with $x = 0.5$ (c) and CGS (d) for which the band masses are calculated. In (b) the fitting procedure is demonstrated for c1 of CIS.*

Band mass	$x = 0$	$x = 0.5$	$x = 1$
$m_{v1}^{\parallel}$	0.103	0.126	0.142
$m_{v1}^{\perp}$	0.113	0.494	0.712
$m_{v2}^{\parallel}$	0.570	0.477	0.533
$m_{v2}^{\perp}$	0.607	0.553	0.562
$m_{v3}^{\parallel}$	0.683	0.733	0.603
$m_{v3}^{\perp}$	0.511	0.129	0.146
$m_{c1}^{\parallel}$	0.092	0.111	0.125
$m_{c1}^{\perp}$	0.097	0.109	0.123

TABLE 3.8: *Electron and hole band masses in units of m_0, the bare electron mass. The interval for fitting of $m_{v1}^{\perp}$ and $m_{v3}^{\perp}$ for $x = 0.5$ is chosen 0.035 $\AA^{-1}$ around Γ because there is strong deviation from quadratic dispersion beyond this value. Similarly, for $m_{v3}^{\perp}$ in case $x = 1$, the interval is 0.070 $\AA^{-1}$.*

3.3.3 Chemical bond

We proceed to discuss properties of the bonds in CIGS compounds. First, we study the projected density of states (PDOS) to identify the character of the different energy bands. Secondly, the partial charges due to bonding are studied using *Bader charge analysis*.

3.3.3.1 Projected density of states

The projected density of states (PDOS) is the decomposition of the density of states to the azimuthal quantum numbers, l, of the electron states of the constituent atoms. From the PDOS the character of the states present in the band structure can be specified. For instance, it can be found which states make up the top of the valence band and which the bottom of the conduction band.

The PDOS calculated with the hybrid functional HSE06 is shown in Figure 3.9 for CIS and CGS in the interval of -7 to 7 eV. In both compounds the hybridization of the Cu-3d with the Se-4p states is apparent. Since the d-bands are much less dispersive than the p-bands, hybridization is inevitable. The strength of the hybridized interaction is inversely proportional to the energy separation of the p- and d-bands. This leads to so-called *p-d repulsion* [3]. This p-d repulsion generally causes an upwards shift of the valence bands. The result of the full study of the PDOS can be found in Figure 3.10. The deepest valence bands are the In-4d (~ -16.4 to -16.5 eV w.r.t. the Fermi level of CIS) and Ga-3d (~ -16.7 to -16.8 eV w.r.t. the Fermi level of CGS) bands, followed

by the Se-4s bands (∼ -13.5 to -15 eV for CIS and ∼ -13.8 to -15.5 eV for CGS). The hybridized In-5s and Se-4p bands of CIS (∼ -5.9 to -6.8 eV) form a considerably narrower band than the corresponding Ga-4s and Se-4p of CGS (∼ -6.4 to -8.0 eV). The top of the valence band is formed by the hybridized Cu-3d and Se-4p bands (0 to ∼ -5.2 eV for CIS and to ∼ -5.4 eV for CGS). The bottom of the conduction band is formed by hybridized In-5s/Ga-4s and Se-4p bands. The Cu-4s orbital is extremely hybridized throughout the spectrum and thus cannot be associated with any specific group of bands.

The binding energy of the electrons can be experimentally determined using *x-ray photoelectron spectroscopy* (XPS). Rife et al. report the result for CIS, measured with synchrotron radiation [54]. It is displayed in Figure 3.11. The energy of the In-4d electrons w.r.t. the top valence band is measured to be ∼ -17.6 eV, about 1 eV below the energy we have obtained theoretically. The Se-4s electron energy is ∼ -13 eV in experiment, compared to ∼ -13.5 to -15 eV in theory. We may conclude that there is a clear correspondence between theoretical and experimental electronic binding energies.

3.3.3.2 Bader charge analysis

Bader charge analysis is a method for the calculation of partial charges of atoms, developed by R. Bader [55]. The method consists of constructing the 'zero-flux surface' of each atom in order to distinguish the atoms. The zero-flux surface is the surface on which the charge density is minimal in the direction normal to the surface. The charge density as calculated in VASP can be used for this purpose [3]. Once the compound is divided into the constituent atoms, the charge per atom follows easily. The result of the charge analysis is shown in Table 3.9. The Bader charge analysis reveals that the partial charges of the atoms are well below their ionic values +1 (Cu), +3 (In and Ga) and -2 (Se). Therefore, the bonds in CIGS are covalent rather than ionic. It is also found that CIS is slightly more ionic than CGS. This is likely to be a consequence of the slightly higher electronegativity of Ga (1.81) compared to In (1.78), on the Pauling scale for electronegativity [56].

[3]The Bader charge analysis has been carried out with code downloaded from http://theory.cm.utexas.edu/bader, made available by the University of Texas.

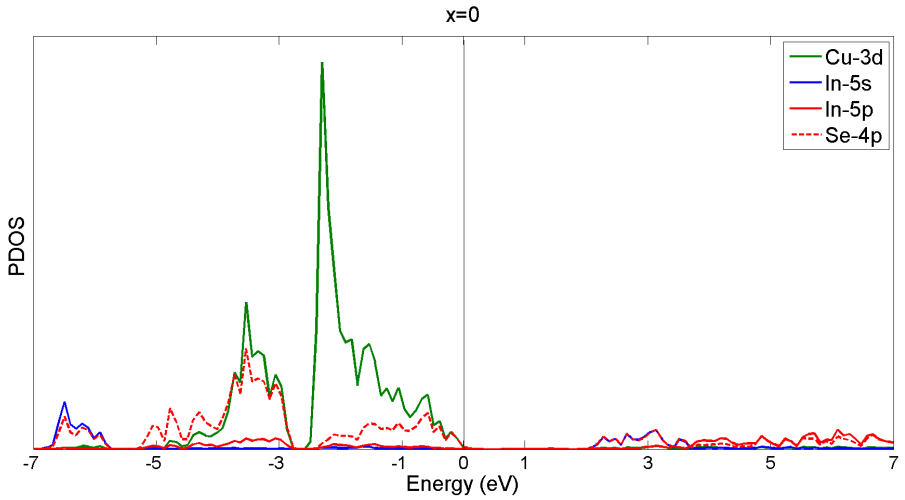

(a) CIS ($x = 0$)

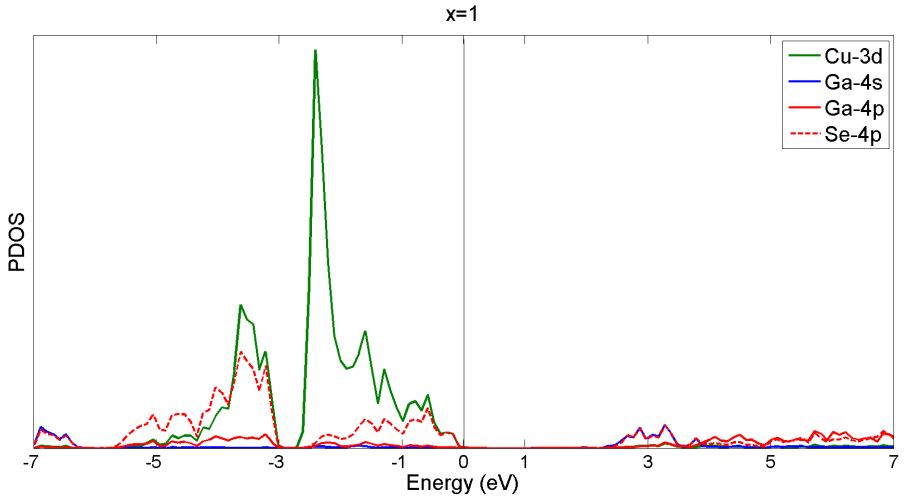

(b) CGS ($x = 1$)

FIGURE 3.9: *Projected density of states (PDOS) in the interval of* -7 *to* 7 *eV with the Fermi level at* 0.

Atom	CIS	CGS
Cu	+0.401	+0.398
In/Ga	+1.153	+1.121
Se	-0.773 , -0.781	-0.751 , -0.768

TABLE 3.9: *The result of Bader charge analysis of CIS and CGS, expressed as partial charge per atom. Se atoms come with two possible partial charges, dependent on their position.*

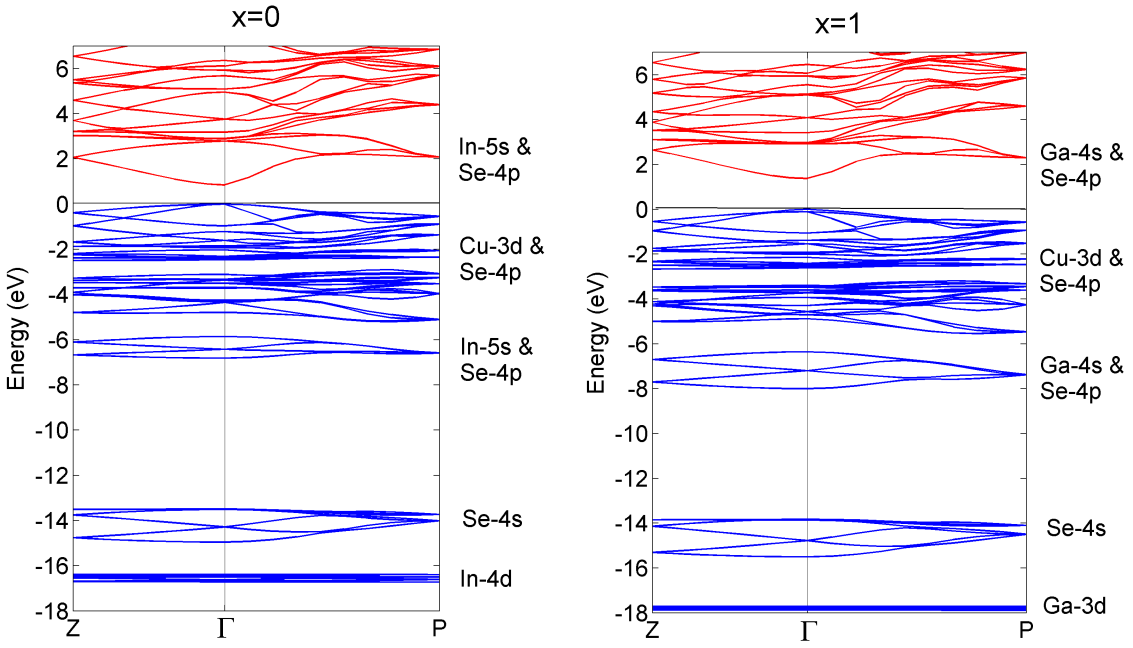

(a) CIS ($x = 0$) (b) CGS ($x = 1$)

FIGURE 3.10: *Band character obtained from the calculation of the PDOS.*

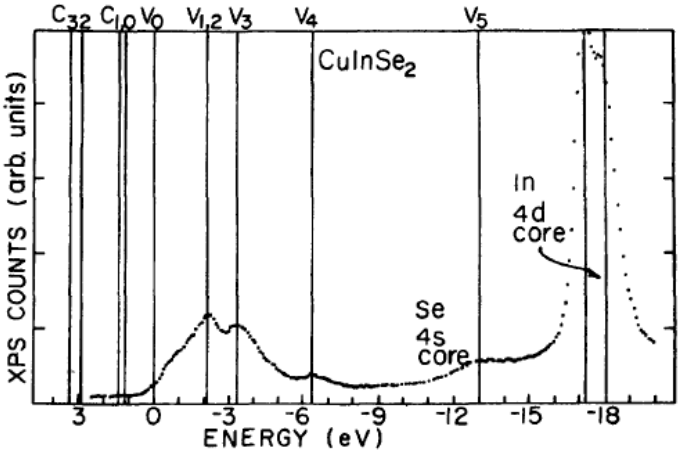

FIGURE 3.11: *The energy spectrum (electron binding energies) of CIS obtained with XPS. [54]*

3.4 Optical properties

3.4.1 Dielectric function

Another quantity that derives from the electronic structure is the *dielectric function*. We focus on the properties of the dielectric response to an electromagnetic wave (AC field) with frequency ω, ignoring magnetic interaction and we employ the cgs unit system. The dielectric function presents an elegant way to deal with the electric displacement field $\mathbf{D}(\mathbf{k},\omega)$ and the electric current density $\mathbf{j}(\mathbf{k},\omega)$ of the dielectric medium. They are defined as:

$$\begin{cases} \mathbf{D}(\mathbf{k},\omega) = \varepsilon^0(\omega)\ \mathbf{E}(\mathbf{k},\omega) \\ \mathbf{j}(\mathbf{k},\omega) = \sigma(\omega)\ \mathbf{E}(\mathbf{k},\omega)\ , \end{cases} \tag{3.11}$$

where $\varepsilon^0(\omega)$ is the *dielectric constant* (dimensionless in cgs units) and $\sigma(\omega)$ is the *conductivity* (units of frequency in the cgs system). They can be combined to form the complex dielectric function [57]:

$$\varepsilon(\omega) = \varepsilon^0(\omega) + \frac{4\pi i}{\omega}\sigma(\omega)\ . \tag{3.12}$$

Only in the case of a DC field and an AC field with low frequency, $\varepsilon^0(\omega)$ and $\sigma(\omega)$ represent distinguishable properties. Then, $\varepsilon^0(\omega)$ describes the response of the core electrons, the *bound charges*, to the electric field. The conductivity $\sigma(\omega)$ is related to the response of the conduction electrons, the *free charges*. More generally, the complex dielectric function is written as the sum of a real part, $\varepsilon_1(\omega)$, and an imaginary part, $\varepsilon_2(\omega)$:

$$\varepsilon(\omega) = \varepsilon_1(\omega) + i\ \varepsilon_2(\omega). \tag{3.13}$$

ε_2 can be calculated from the electronic states by application of *Fermi's golden rule* that expresses the probability of interband transitions. For this purpose, the periodic factors of the Bloch states, $u_{m,\mathbf{k}}$ (m being the band index) are used. The corresponding orbital energy is denoted $\varepsilon_{m,\mathbf{k}}$. The Bloch states are normalized w.r.t. the unit cell by means of the unit cell volume Ω. One also has to consider that the dielectric function is in general a tensor, $\varepsilon_2^{\alpha\beta}(\omega)$, with $\alpha,\ \beta$ for instance the Cartesian directions $x,\ y,\ z$. Thus

the formula for the dielectric function's tensor reads [42]:

$$\varepsilon_2^{\alpha\beta}(\omega) = \frac{4\pi e^2}{\Omega} \lim_{q\to 0} \frac{1}{q^2} \int \frac{d\mathbf{k}}{(2\pi)^3} \sum_{c,v} 2w_{\mathbf{k}}\ \delta\left(\varepsilon_{c,\mathbf{k}} - \varepsilon_{v,\mathbf{k}} - \omega\right) \langle u_{c,\mathbf{k}+\mathbf{e}_\alpha q} | u_{v,\mathbf{k}} \rangle \times \langle u_{c,\mathbf{k}+\mathbf{e}_\beta q} | u_{v,\mathbf{k}} \rangle^* \ , \tag{3.14}$$

where c and v refer to conduction and valence band, $w_{\mathbf{k}}$ is the weight of wavevector $\mathbf{k}$ and $\mathbf{e}_\alpha$, $\mathbf{e}_\beta$ are the unit vectors in the α, β directions. Formula 3.14 gives the dielectric function in the *dipole approximation* [58]. The factor 2 originates from the double occupation of the orbitals. The real part of the dielectric function, $\varepsilon_1(\omega)$, follows immediately from $\varepsilon_2(\omega)$ through the *Kramers-Kronig relation*:

$$\varepsilon_1^{\alpha\beta}(\omega) = 1 + \frac{2}{\pi} \mathcal{P} \int_0^\infty \frac{\varepsilon_2^{\alpha\beta}(\omega')\ \omega'}{\omega'^2 - \omega^2 + i\epsilon} d\omega' \ . \tag{3.15}$$

In this expression $\mathcal{P}$ is the *principal value* and ϵ is an infinitesimal number.

We study the dielectric functions of CIS, CIGS with $x = 0$ and CGS. The treatment of the dielectric function we have discussed, is implemented in VASP as the function LOPTICS [42]. The dielectric function is calculated by Equations 3.14 and 3.15 from the states calculated self-consistently on a $6 \times 6 \times 6$ k-point mesh using the tuned hybrid functional. The results are displayed in Figure 3.12. The onset energy and positions of the main peaks are found to be well converged w.r.t. the choice of the k-point mesh. Some minor oscillations may be suppressed with the choice of a denser mesh. The number of bands in the calculation is 208 of which 72 are valence bands, since a considerable number of unoccupied bands has to be taken into account for an accurate calculation of the dielectric function. Since CIGS are anisotropic, the dielectric tensor has $\parallel$ and $\perp$ components. $\parallel$ denotes the Cartesian (100) direction, equivalent with the (010) direction for the chalcopyrite symmetry, while $\perp$ refers to the (001) direction. An important feature of ε_2 is its relation to the optical selection rules through Fermi's golden rule. In this way ε_2 shows whether the transition from VBM to CBM at Γ is allowed by means of symmetry. Indeed, it is found that the onset of ε_2 occurs at E_g of the respective compounds and thus the band gap in CIGS compounds is *direct*. This is also an experimental fact [12]. Additionally, it is apparent that ε_2, related to the optical absorption, decreases with increasing Ga content at the lower energy range. This may contribute to the phenomenon of diminishing efficiency of CIGS photovoltaic devices as

more than $\sim$ 30 % Ga is incorporated [59].

The dielectric function can be measured by *ellipsometry*. For this purpose one rewrites the dielectric function as $\sqrt{\varepsilon} = n + i\kappa$, where n is the refractive index and κ the extinction coefficient. Consequently the reflection coefficient, ratio of the reflected and incident electric field, reads [57]:

$$\begin{aligned} r &= \frac{|E^r|}{|E^i|} \\ &= \left|\frac{1-\sqrt{\varepsilon}}{1+\sqrt{\varepsilon}}\right| \\ &= \frac{(1-n)^2+\kappa^2}{(1+n)^2+\kappa^2} \ . \end{aligned} \tag{3.16}$$

In order to extract n and κ from measured r, one can employ the Kramers-Kronig relation between them. Through ellipsometry with two polarization compounds, the $\parallel$ and $\perp$ components of the dielectric tensor can be measured. M. I. Alonso et al. have performed ellipsometric measurements on single-crystal CIS and CGS at room temperature [60]. The experimental dielectric functions are depicted in Figure 3.13 [4]. A good agreement with the calculated results presented in Figure 3.12 is found. For instance, the experimental peaks in ε_2 at 2.8 eV ($\parallel$ and $\perp$) and 4.7 eV ($\perp$) in the case of CIS and corresponding peaks at 3.2 eV and 5.0 eV for CGS are met in the hybrid optical calculations. In the experimental result, details in the dielectric function are suppressed, due to experimental noise and the effect of nonzero temperature.

[4] In the figure, we have adapted the notation of the different components of the dielectric tensor to agree with our convention.

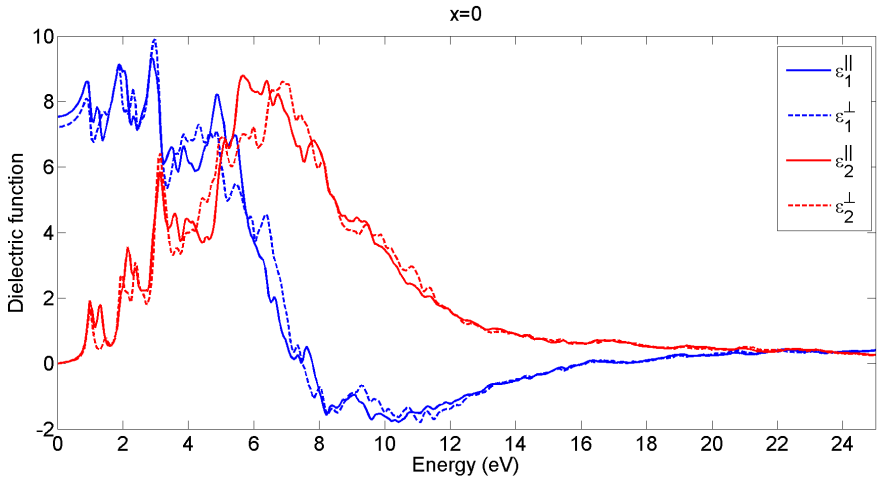

(a) CIS ($x = 0$)

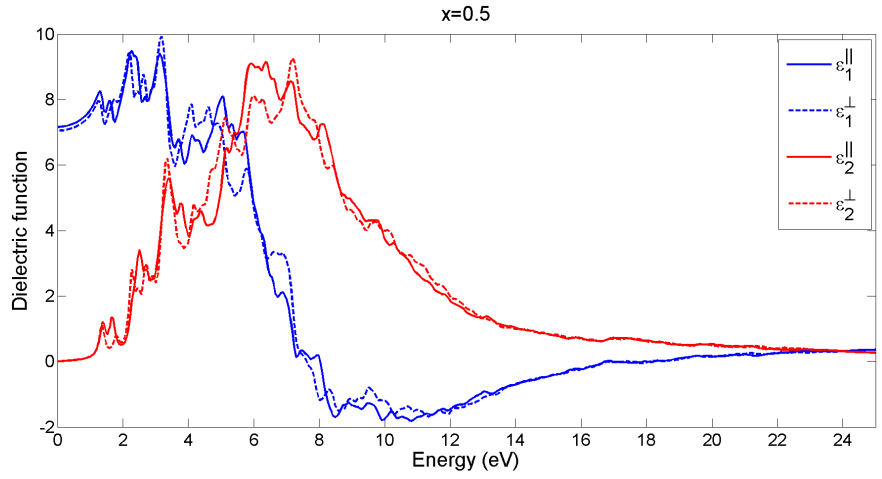

(b) CIGS with $x = 0.5$

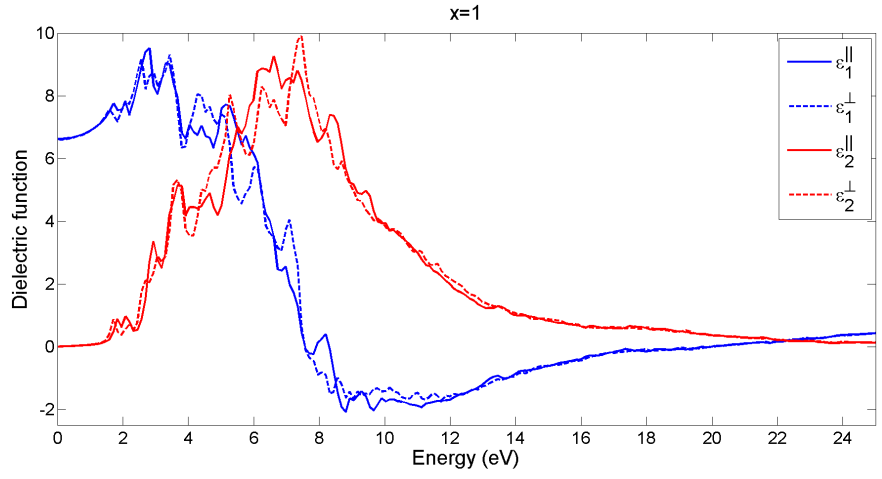

(c) CGS ($x = 1$)

FIGURE 3.12: *Dielectric functions of CIS (a), CIGS with $x = 0.5$ (b) and CGS (c) in units of the vacuum permittivity (which is 1 in the cgs unit system) as a function of the energy of the incident electromagnetic wave. The real part, ϵ_1, is plotted in blue and the imaginary part, ϵ_2, in red. $\parallel$ components are dashed curves, whereas $\perp$ components are full.*

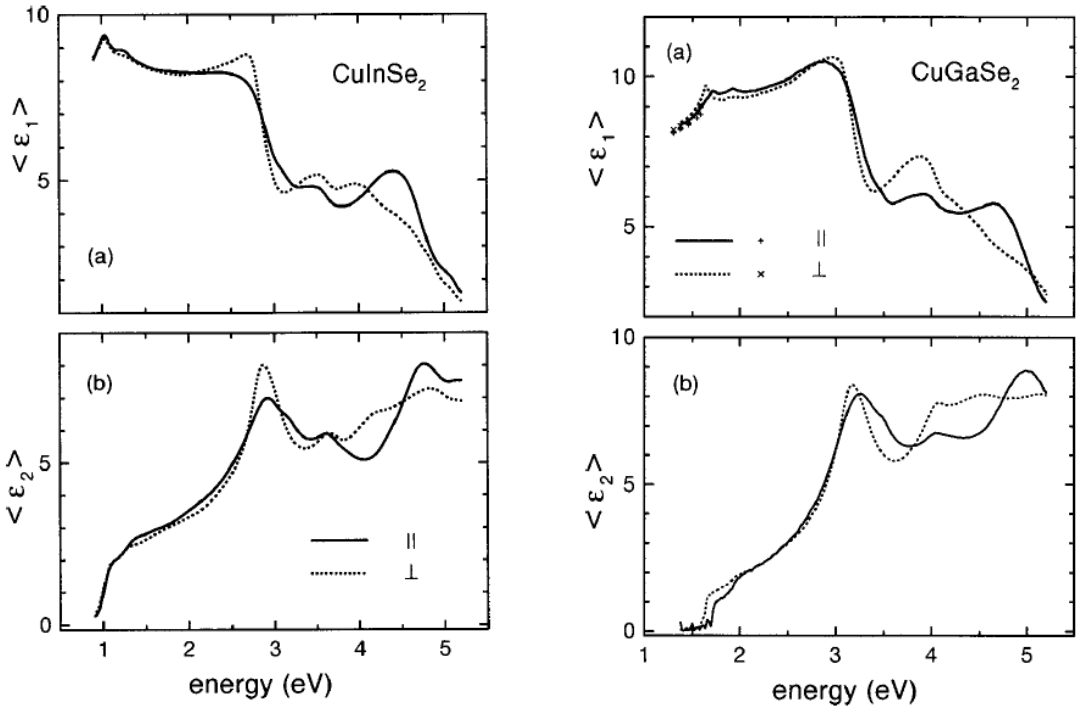

(a) CIS ($x = 0$)

(b) CGS ($x = 1$)

FIGURE 3.13: *Experimental results for dielectric function of single-crystal CIS and CGS, obtained with ellipsometry at room temperature. [60]*

Chapter 4

Band alignment of CIGS

4.1 Introduction

In the study of the electronic structure of $CuIn_{1-x}Ga_xSe_2$ (CIGS) materials in the previous chapter, we did not yet discuss the *band alignment* (or band line-up) of the compounds with varying Ga amount (x). Whenever band structures have been presented, they were not aligned on a common energy scale. The reason is that calculations based on density functional theory do not contain an absolute energy level. For instance, in VASP, the average electrostatic potential (i.e. the potential including interaction with ions and a mean field interaction between electrons) is set to zero [42]. The consequence is a different zero of energy for different materials. Therefore, band alignment is not an easy task. At the same time, the band alignment of components of a photovoltaic device determines many of the properties of the device. The band line-up of the device alters with varying x in CIGS; there may even be a gradient of x across the absorber layer. This is a major reason why a full chapter is dedicated to band alignment of CIGS.

Within the field of study of computational electronic structure calculations several methods have been proposed for band alignment. Herein lies the other main goal of this chapter. Namely, to review and test these different methods and to compare the results they produce for a single group of materials, the CIGS compounds. We will focus on (i) the method consisting of calculating the *branch-point energy* (BPE) and (ii) the method based on the potential in a *slab* of material. The branch-point method has the advantage that it solely relies on the bulk band structure. The limitation is that a band alignment

by branch-points is a relative alignment on a common energy scale, yet without an absolute reference. Contrary to this, in the supercell used for slab calculations, vacuum is included. This allows for an absolute level of energy, namely the vacuum level. Thus, also the electron affinity of the semiconductor immediately follows. The slab calculation requires a larger supercell, since both a slab of sufficient thickness and an adequate amount of vacuum have to be included. Therefore, in principle, slab calculations are much harder to perform computationally. We will show that slab calculations for the purpose of alignment that rely solely on the PBE functional present a very reliable approximation. This chapter is arranged as follows: first, we explain in more detail the methods for band alignment, then we proceed to a comparison of the results.

4.2 Methods

4.2.1 Branch-point energy

The branch-point energy is a notion originating from surface physics. At the interface of two materials, the bulk electronic states - Bloch functions in case of a periodic arrangment - are modified. *Surface states* are exponentially decaying states, related to a complex wave vector near the Brillouin zone edge [61]. For a translationally invariant interface, Im($\mathbf{k}$) is normal to the interface. These states are also known as Virtual Gap States (ViGS), in case of an interface between two semiconductors. Their eigenvalues usually lie within the band gap of the bulk material. ViGS can be considered a combination of bulk valence and conduction bands [21]. Then, the branch-point energy (BPE) is defined as the energy for which the character of the ViGS changes from VB-like (donor-like) to CB-like (acceptor-like) [1]. The branch-point energy can alternatively be defined as energy of the ViGS state with the shortest decay length [62]. As the ViGS extend in both materials, a charge transfer may be produced that depends on the Fermi levels and BPEs and leads to an interface quantum dipole. J. Tersoff has argued that the energy bands of the adjacent materials line up so the interface dipole vanishes [63]. This is the accomplished by an alignment of the BPE of both materials. Tersoff has expressed this in the form of a Green's function, building on general work by R. E. Allen on Green's functions for surface physics [64]. The following real-space Green's function expresses

[1] The term *charge neutrality level* is used for interfaces of a metal and a semiconductor.

the propagation with energy E near an interface:

$$\begin{aligned} G(\mathbf{R}, E) &= \int d\mathbf{r} \sum_{n,\mathbf{k}} \frac{\psi^*_{n\mathbf{k}}(\mathbf{r})\ \psi_{n\mathbf{k}}(\mathbf{r}+\mathbf{R})}{E - E_{n\mathbf{k}}} \\ &= \sum_{n,\mathbf{k}} \frac{e^{i\mathbf{k}\cdot\mathbf{R}}}{E - E_{n\mathbf{k}}} \ , \end{aligned} \tag{4.1}$$

where $E_{n\mathbf{k}}$ is the complex band structure (i.e. the band structure as a function of complex $\mathbf{k}$). Recall that ViGS are defined for wave vectors close to the Brillouin zone edge. So, indeed one has to consider correlations between states that are a multiple of the lattice vector apart: $\psi_{n\mathbf{k}}(\mathbf{r})$ and $\psi_{n\mathbf{k}}(\mathbf{r}+\mathbf{R})$. In the second step of Equation 4.1 we use the fact that these states are Bloch functions. Within the Green's function approach the BPE is defined as the energy for which the Green's function changes sign, i.e. $G(\mathbf{R}, E_{BP}) = 0$. The vector $\mathbf{R}$, multiple of a lattice vector of the material, is preferably chosen parallel to $\mathrm{Im}(\mathbf{k})$ and thus normal to the interface (in case it is translationally invariant). The Green's function has to be converged for sufficiently large $|\mathbf{R}|$ for all possible interface orientations. This strongly complicates a practical use of the Green's function method as given by Tersoff [65]. On the other hand, a clear advantage is that the method only depends on surface orientation and not on structural details of the surface.

In order to overcome the problem of convergence of the Green's function for all possible surface orientations, interface-averaged approximations have been developed. In an article on transparent conducting oxide (TCO) materials (SnO_2, $CuAlO_2$ and $CuInO_2$) [20], J. Robertson and B. Falabretti have proposed the following Green's function [2]:

$$\begin{aligned} G(E) &= \sum_{n,\mathbf{k}} \frac{1}{E - E_{n\mathbf{k}}} \\ &= \int \frac{N(E')}{E - E'} \mathrm{d}E' \ , \end{aligned} \tag{4.2}$$

where $N(E')$ is the density of states at energy E'. Again, the BPE is found as $G(E_{BP}) = 0$. We have used the Green's function as given by Robertson and Falabretti for calculation of the BPE in CIGS compounds.

[2] In the article, the definition of the Green's function in terms of the DOS contains an additional integration over the BZ. The argument of this integration, however, is not dependent on the wavevector. The integration introduces thus only a different normalization that is not relevant in the calculation of the BPE.

Another approach for interface-averaged BPE calculation that can be followed, has also been introduced by Tersoff. He found semi-empirically that the BPE for the diamond and zincblende structure can be calculated as the average of the valence band maximum (VBM) at Γ and the conduction band minimum (CBM) at X [21]:

$$E_{BP} = \frac{1}{2}\left(\varepsilon_{VBM}(\Gamma) + \varepsilon_{CBM}(X)\right) \ . \tag{4.3}$$

The result is that the centers of the band gaps of adjacent materials of this kind coincide within the approximation. A. Schleife et al. have proposed a generalization of this procedure for other structures [21]. The idea originates from an extensive theoretical discussion of interface states by F. Flores and C. Tejedor [66]. The BPE is calculated by the following average over the BZ:

$$E_{BP} = \frac{1}{2N_{\mathbf{k}}} \sum_{\mathbf{k}} \left[\frac{1}{N_{VB}} \sum_{i}^{N_{VB}} \varepsilon_{VB_i}(\mathbf{k}) + \frac{1}{N_{CB}} \sum_{j}^{N_{CB}} \varepsilon_{CB_j}(\mathbf{k}) \right] \ . \tag{4.4}$$

In this expression $N_{\mathbf{k}}$ is the number of k-points in the mesh, N_{VB} and N_{CB} are the number of valence and conduction bands. Regarding the number of valence and conduction bands to include in this calculation, there is some uncertainty. One has to investigate the influence of the choice of N_{VB} and N_{CB} on the alignment. Schleife et al. have applied Formula 4.4 to nitrides (e.g. GaN and InN) and oxides (e.g. CdO and ZnO) using a HSE03 hybrid functional. They have chosen to retain the cubic unit cell, e.g. CdO as the reference for N_{VB} and N_{CB}. It contains 8 valence electrons (not counting the d-electrons). For the cubic unit cell, two valence bands and one conduction band are selected to use in Formula 4.4. For other structures N_{VB} and N_{CB} are scaled according to the number of valence electrons (without d-electrons). The approach proposed by Schleife et al. for the calculation of the BPE has been attempted for the photocatalyzer TiO_2 by Deák et al. [67]. Regarding the uncertainty connected to N_{VB} and N_{CB}, they conclude that there is little influence on the BPE.

For CIGS, we investigate the dependence of the BPE and band alignment on N_{VB} and N_{CB}. To test this, we calculate the BPE of $CuInSe_2$ (CIS), $CuIn_{0.5}Ga_{0.5}Se_2$ (CIGS with $x = 0.5$) and $CuGaSe_2$ (CGS) making use of Equation 4.4. We select an equal number of valence and conduction bands, $N_{VB} = N_{CB}$, and vary this number as 1, 5, 10, 15 and 20. Computational details largely coincide with those discussed in Section 3.2 of Chapter 3.

The $1 \times 1 \times 2$ supercell containing 16 atoms is used for the implementation of the alloys. A $4 \times 4 \times 4$ Monkhorst-Pack k-point mesh is selected that yields convergence of the total energy within ~ 2 meV. The tuned hybrid functional introduced in Section 3.3.1 of Chapter 3 is used for the calculation of the eigenvalues. The resulting differences in BPE, ΔE_{BP}, are displayed in Figure 4.1. The BPE of CGS calculated with $N_{VB} = N_{CB} = 1$ is set to zero. One observes that the curves of the BPE as function of $N_{VB} = N_{CB}$ belonging to different compounds are almost equidistant. Thus the difference in BPE of either two compounds is approximately constant, especially for $N_{VB} = N_{CB} > 1$. We observe that the BPE itself is significantly influenced by the choice of N_{VB} and N_{CB}. Consequently, caution has to be exercised regarding the interpretation of the BPE. On the other hand the relative alignment is mostly unaffected. We find it to be accurate within a margin of 0.02 eV for a wide range of N_{VB} and N_{CB} (if more than two bands are selected). We proceed by using the counting procedure for N_{VB} and N_{CB} in Formula 4.4 that Schleife and coworkers have established. CIGS contain Cu: [Ar] $\underline{3d^{10}4s^1}$, In: [Kr] $\underline{4d^{10}5s^25p^1}$, Ga: [Ar] $\underline{3d^{10}4s^24p^1}$ and Se: [Ar] $3d^{10}\underline{4s^24p^4}$. The electrons occupying the underlined orbitals are computationally treated as valence electrons. This means that the $1 \times 1 \times 2$ supercell contains 64 electrons, not counting the d-electrons. Following Schleife et al., the BPE should be calculated with 16 VBs and 8 CBs. The relative alignment that follows from the BPE method can be thoroughly tested by comparison with the more direct method of alignment via slab calculations.

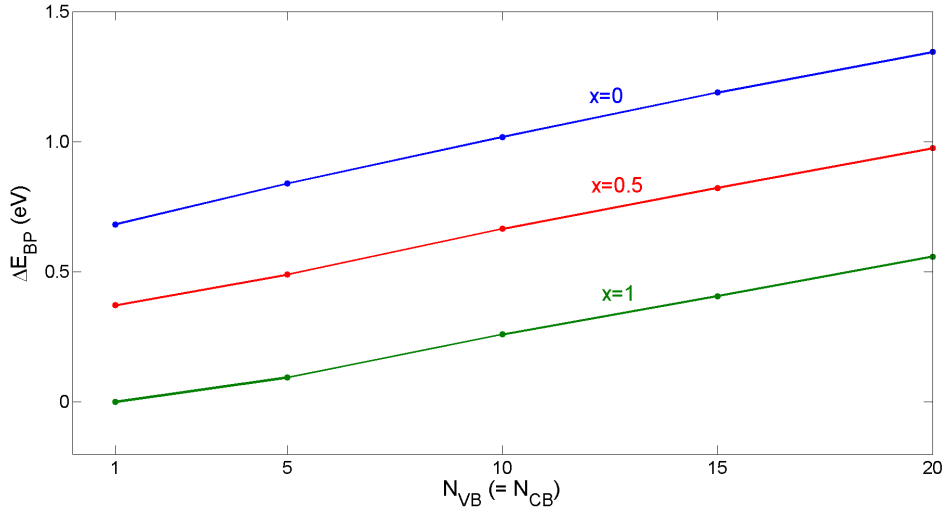

FIGURE 4.1: *The branch-point energies of CIS ($x = 0$), CIGS with $x = 0.5$ and CGS ($x = 1$) calculated employing Equation 4.4 as function of $N_{VB} = N_{CB}$. The BPEs are relative to the BPE of CGS calculated with one VB and one CB, which is set to* 0.

4.2.2 Slab calculation

The method for alignment based on slab calculations has, for example, been described by C. G. Van de Walle et al. [68]. They have applied it for studying semiconductor nitrides (e.g. GaN and InN) employing the HSE06 functional. Alignment by slabs allow for the determination of an absolute reference for band alignment, namely the potential in vacuum, V_{vac}. In principle two calculations have to be performed: (i) a calculation of the bulk band structure w.r.t. the average potential and (ii) a slab calculation to relate the average potential in bulk to the potential in vacuum. We portray the principle for alignment within this method schematically in Figure 4.2. In the left part of the figure the bulk calculation is represented. The zero of energy is the reference chosen by VASP, which varies for different materials. It is on the same energy scale as the average potential $\langle V \rangle$ in bulk. We will calculate $\langle V \rangle$ as a *planar average*, this means as potential averaged over planes along a certain direction, in our case lattice vector $\mathbf{a}_3$. In the part right of the figure the result of the slab calculation is shown. The potential is the so-called *macroscopic average potential*, which comes down to the average of the planar average potential over a distance of one unit cell along $\mathbf{a}_3$ (the same direction as used for the planar average) [68]. The purpose of the macroscopic average potential is to distinguish between the average potential $\langle V \rangle$ in bulk and vacuum on the same energy scale. Then $\langle V \rangle$ in bulk in both calculations naturally have to coincide, as is shown in the figure. In this way the bulk band structure is set on a common energy scale with the potential in vacuum, V_{vac}, an absolute reference. The slab selected for this calculation in our work can be found in Figure 4.3, for CIS. The slab extends in the $\mathbf{a}_1$ and $\mathbf{a}_2$ directions, while vacuum space is implemented in the $\mathbf{a}_3$ direction. The supercell for the slab calculation is indicated. The bulk material thus is interrupted in the $\mathbf{a}_3$ direction, forming a slab. The thickness of the slab corresponds to 2 primitive unit cells, that consist of 9 atomic layers of alternate Cu and In planes and Se planes. This is sufficiently thick for convergence of the potential within the slab to the potential in bulk. The thickness of the slab accordingly is 13.2 Å for calculations with the PBE functional and 13.1 Å in case of HSE06. This corresponds with a distance of 14.4 Å in the $\mathbf{a}_3$ direction for PBE and 14.3 Å for HSE06. The atomic positions in the slab are not relaxed because we wish to investigate the alignment of bulk band structures.

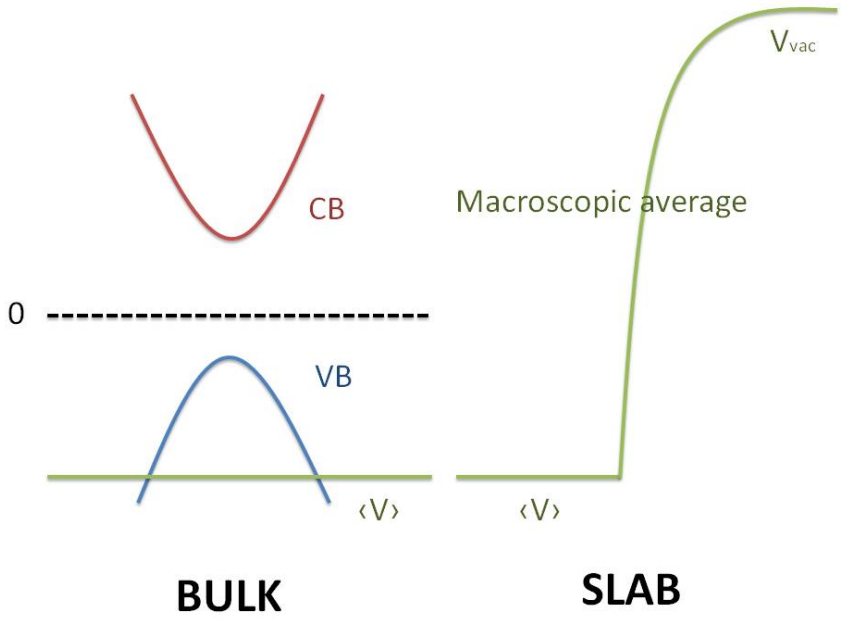

FIGURE 4.2: *A schematic representation of alignment within the slab method. On the left one finds the bulk band structure with its zero of energy and average potential $\langle V \rangle$, obtained from the bulk calculation. On the right $\langle V \rangle$ in bulk, as obtained from a slab calculation is aligned. This implies an alignment of the bulk band structure with the potential in vacuum, V_{vac}.*

As such, we do not allow for reconstruction at the surface [3]. A convergence study is carried out assessing the effect of the included amount of vacuum on the total energy of the material contained within the slab supercell. For an amount of vacuum of twice the thickness of the slab, convergence up to less than 3 meV for the whole supercell is reached. A $6 \times 6 \times 1$ Monkhorst-Pack k-point grid is chosen for Brillouin zone sampling, since the supercell is largely extended in the $\mathbf{a}_3$ direction.

As mentioned in the introduction to this chapter, multiple approaches for the slab calculations can be thought of. The reason is that different potentials can be studied in VASP. The total potential in the Kohn-Sham equation is:

$$V_{TOT} = V_{ext} + V_H + V_{XC} \ , \tag{4.5}$$

where the first term is the external potential due to interaction with the nuclei, the

[3]Nonetheless, it has to be noted that the alignment via the slab method is in fact also approximate. The electronic structure is in general slightly altered at the surface. This possibly results in a surface dipole, that affects the potential inside the slab. The surface dipole can be described by advanced charge analysis methods, e.g. Hirshfeld charge analysis. The effect on the alignment is an open question and is beyond the scope of this thesis.

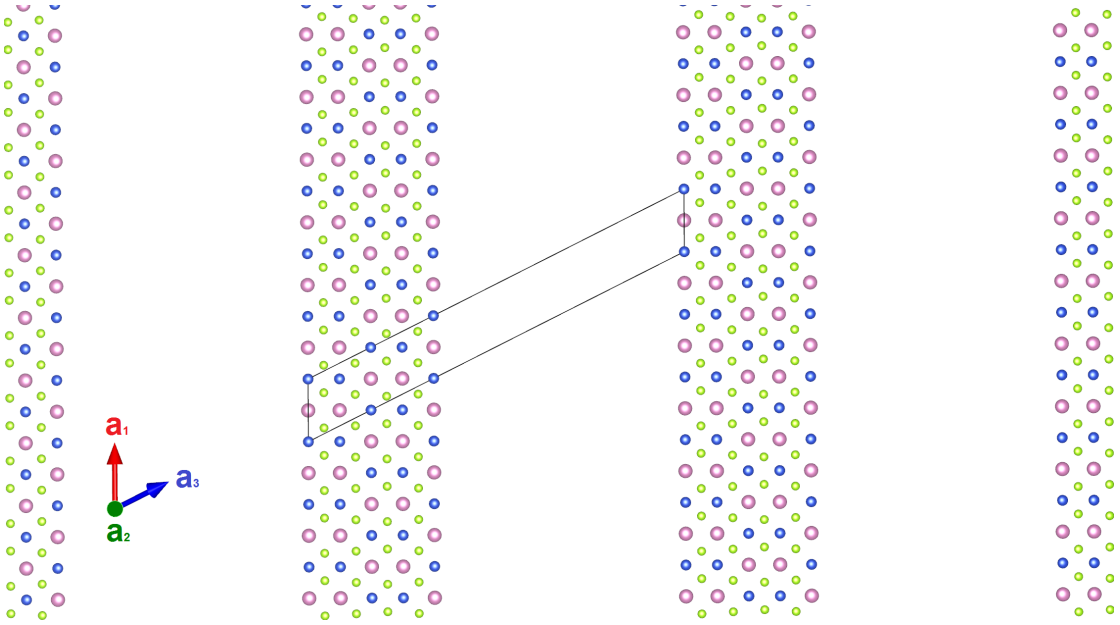

FIGURE 4.3: *Periodic pattern of slabs of CIS by the implementation of vacuum along the* $\boldsymbol{a}_3$ *direction. The material extends in the* $\boldsymbol{a}_1$ *and* $\boldsymbol{a}_2$ *directions, forming a slab. The amount of vacuum relates to the thickness of the slab as 2:1.*

second term is the mean-field electronic (Hartree) potential and the last term is the exchange-correlation potential. Another potential that can be given as output in VASP is the electrostatic potential:

$$V_{HAR} = V_{ext} + V_H \ . \tag{4.6}$$

The advantage of the electrostatic potential is that in VASP the zero of energy is defined as the average electrostatic potential, i.e. $\langle V_{HAR} \rangle \equiv 0$ [42]. The various methods that can be followed for slab calculations are listed in Table 4.1. Method 1 consists of a bulk and a slab calculation with the hybrid functional outputting the total potential. From the bulk calculation, the bulk band structure and the average potential in bulk are obtained. Methods 2 and 3 differ from Method 1 because the electrostatic potential is used. The bulk calculation still yields the band structure, yet it is not necessary to calculate the average of the potential, it is zero by definition. In principle, since the electrostatic potential does not contain exchange and correlation, calculations using PBE and HSE06 are equivalent. A small difference may exist due to the slightly different atomic positions for both functionals. We have tested the effect of the choice of the method in slab calculations for CIS and CGS. The result is listed in Table 4.2. The tolerance on the vacuum level is found to range from 0.02 eV to 0.06 eV. The alignment of CIS and CGS itself varies at most 0.01 eV. Thus, if necessary for computational reasons, Method 3

may be employed for band alignment based on slabs. Since the slab calculation itself is carried out with the PBE functional, the computation is drastically simplified.

Method	Potential	Functional
Method 1	V_{TOT}	HSE06
Method 2	V_{HAR}	HSE06
Method 3	V_{HAR}	PBE

TABLE 4.1: *Possible methods for a slab calculation.*

Method	VBM of CIS	VBM of CGS	Offset
Method 1	-4.86	-4.92	0.06
Method 2	-4.90	-4.95	0.05
Method 3	-4.84	-4.89	0.05

TABLE 4.2: *Valence band minima (VBM) w.r.t. the vacuum level, in eV, obtained from different methods listed in Table 4.1. Also the offsets between the VBM of CIS and CGS are given (in eV).*

4.3 Results

We now bring together the results for the alignment obtained from three different approaches. On one side, we show two approaches that rely on the calculation of the branch-point energy, namely (i) via the Green's function as described by Robertson and Falabretti (following Equation 4.2) and (ii) via the summation proposed by Schleife et al. (given in Equation 4.4). Also, the alignment by means of a slab calculation is presented. It provides an absolute reference for the alignment, namely the potential in vacuum, V_{vac}. The three approaches are compared via the alignment of CIS and CGS. Further on, we will present an alignment of a larger variety of CIGS compounds.

To start with, let us take a look at the potentials that occur in the slab approach. We treat CIS as an example. In Figure 4.3 (a) and (b), the total potential is given respectively in bulk and in a slab, both calculated by means of a HSE06 functional. The planar averages are taken along $\mathbf{a}_3$. These plots are used for an alignment following Method 1 as described in Table 4.1. In Figure 4.3 (c) and (d), the same systems are studied by means of the electrostatic potential and the PBE functional. This leads to an alignment via Method 3, introduced in Table 4.1. Method 2 follows an analogous approach, yet using the HSE06 functional. The alignment following from the slab method is shown in Figure 4.4 (a). As we have already discussed, the vacuum level is altered by at most

0.06 eV by the choice of the potential and functional. The relative alignment is only influenced by 0.01 eV. For the alignment in Figure 4.4 (a), Method 2 has been applied. The alignment that is found, is a so-called *straddling* (type-I) alignment of two semiconductor materials. This means that the VBM of material 1 (CIS) lies above the VBM of material 2 (CGS) and the other way around for the CBM. We remind that the band gaps of CIS and CGS as calculated with the hybrid HSE06$^{(t)}$ functional are respectively 1.00 eV and 1.72 eV, as has been elaborated in Chapter 3, Section 3.3.1. The VBM of CIS is located at -4.90 eV and the VBM of CGS at -4.95 eV. The VBM offset between CIS and CGS is found to be 0.05 eV and the CBM offset is 0.67 eV.

In Figure 4.4 (b) and (c), one can find the relative band line-ups of CIS and CGS that are achieved by aligning the BPE of both materials, which is then set to 0. More specifically, in (b) the BPE is obtained by evaluation of a Green's function, as given in Equation 4.2. For (c), the BPE is found as the BZ average of the band structure, according to Equation 4.4. Both formulas have been evaluated using the same valence and conduction bands, i.e. the top 16 VBs and the bottom 8 CBs. The two methods for BPE determination respectively yield VBM offsets of 0.21 eV and 0.13 eV and CBM offsets of 0.51 eV and 0.59 eV. Since the BPE method for band line-up is an approximate method, it has to be compared to the result from the more exact slab treatment. The VBM offset from the latter method is 0.05 eV, so there is much better agreement with the alignment in (b) than in (c). The reason may be that the BPE of CIS in the Green's function method lies above the CBM. Usually, the Green's function method is not applicable if the BPE is not located in the band gap, due to the divergences if $E_{BP} = E_{n\mathbf{k}}$. In the case of CIGS it is nonetheless possible to find $G(E_{BP}) = 0$ with the BPE in the lower part of the conduction band, because the DOS is low in the bottom part of the conduction band.

From the previous considerations, one can conclude that the BPE method for alignment based on the BZ average of the band structure, is in rather good agreement with an alignment by use of a slab. The difference in VBM offset is found to be 0.08 eV. The clear advantage of the BPE method is it being completely accessible by bulk calculations instead of the computationally restrictive calculations on slab supercells. In this way we can align a full range of CIGS compounds with varying Ga content, x. As in Chapter 3, alloys are simulated by x=0, 0.25, 0.5, 0.75 and 1. The alignment of these CIGS compounds is displayed in Figure 4.5. The band line-up is straddling (type-I). The VBM alters much less from CIS to CGS than the CBM. This can be easily understood

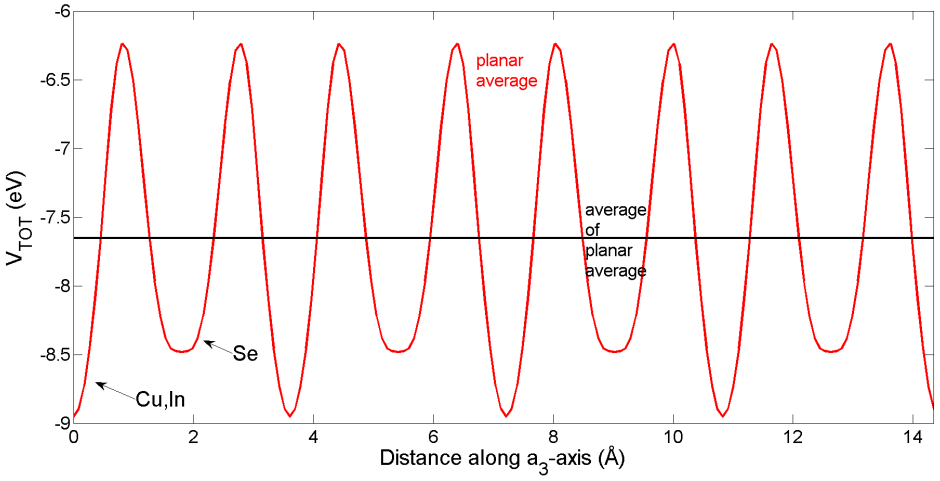

(a) The total potential (planar average) in bulk (red). The planes containing Cu and In and those containing Se are well resolved. The average of the planar average at −7.66 eV is plotted (black). The potential is calculated within a treatment with the HSE06 functional.

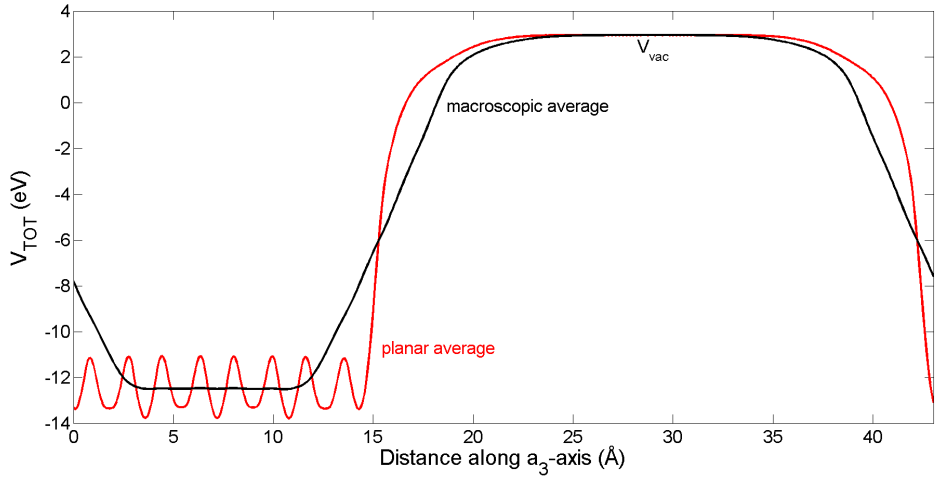

(b) The total potential (planar average) in a slab (red). The macroscopic average is also plotted (black) and the vacuum level is indicated. This result is obtained employing a HSE06 functional.

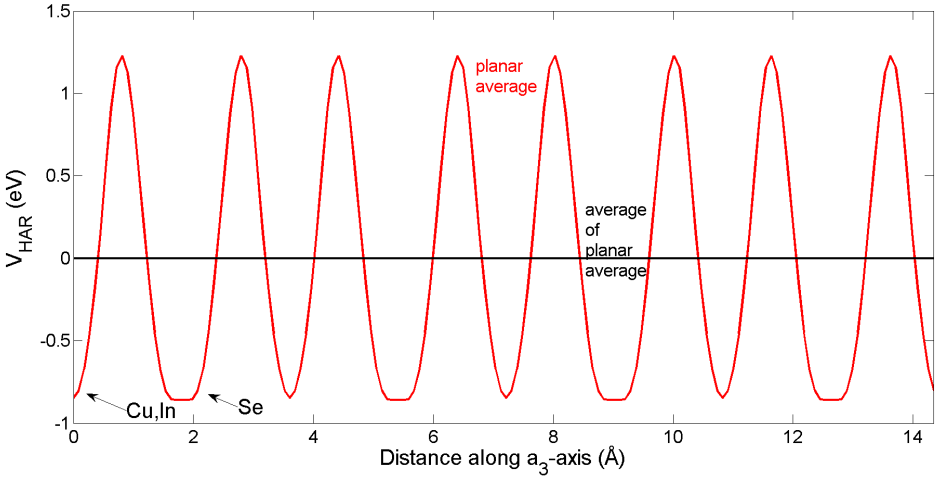

(c) The electrostatic potential (planar average) in bulk (red). The average of the planar average electrostatic potential is zero. The calculation is performed using the PBE functional.

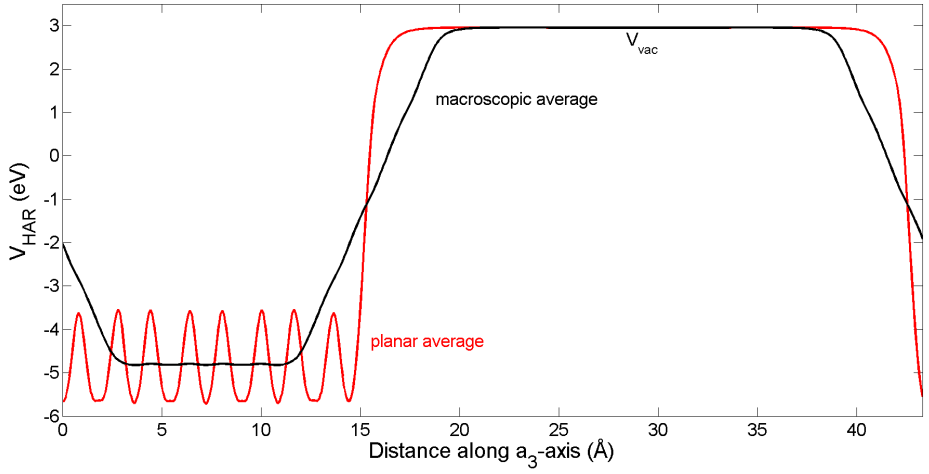

(d) The electrostatic potential (planar average) in a slab (red). The macroscopic average is also plotted (black) and the vacuum level is indicated. The PBE functional is used.

FIGURE 4.3: *Potentials appearing in the band alignment using the slab method, for CIS as an example.*

from the PDOS of CIGS, that is discussed in Chapter 3, Section 3.3.3. The PDOS indicates that the top of the CIGS valence band is formed by orbitals with hybridized Cu-3d and Se-4p character. The bottom of the conduction band is made from Ga-4s and/or In-5s orbitals hybridized with Se-4p. Thus, by interchanging In with Ga, the CBM is naturally most affected.

In the scientific literature, there is not much work available on the mutual alignment of CIGS, neither theoretical nor experimental. W. Mönch has performed an alignment of CIS and CGS by calculation of the BPE [69]. The electronic structure is calculated from a semi-empirical tight-binding model. Mönch finds that the BPE lies 0.75 eV above the VBM of CIS and 0.93 eV above the VBM of CGS. Thus the VBM offset between CIS and CGS is 0.18 eV. This is within 0.05 eV from the band offset we find by calculating the BPE as the BZ average of the band structure. Our hybrid electronic structure calculation is in principle more advanced than a tight binding model. A band line-up can be experimentally determined by *Photoelectron Spectroscopy* (PES), where the *electron affinities* are measured [67]. The electron affinity of a semiconductor is the energy difference between the CBM and the vacuum energy level. This immediately produces a band alignment, since the vacuum level provides an absolute reference. To our knowledge, no systematic experimental study of the mutual band line-up of CIGS is available.

Finally, it is interesting to point out that in compounds containing more In than Ga, the calculated BPE is located close to the CBM, as one observes in Figure 4.5. It even lies within the conduction band in the case of CIS. We wish to remind that caution is needed regarding the calculated value of the BPE. For CIGS, we found it to be strongly dependent on the number of valence and conduction bands included in the calculation, at the same time conserving the relative alignment (see Section 4.2.1 of this chapter). Nevertheless, the BPE may play an important role in the interface properties of polycrystalline CIGS absorber layers. It leads to donor-like surface states nearby the CBM, that introduce electrons in the conduction band at an interface. This causes an accumulation of electrons at this interface. Indeed, it has been experimentally demonstrated that the free surface and heterojunction of CIS are electron-rich [14]. The absorber layer itself is hole-rich (mainly due to Cu-vacancy defects). This phenomenon is named 'type-inversion'. C. Persson and A. Zunger have proposed a model for this type-inversion: the existence of a *hole barrier* [14]. The notion of the hole barrier starts from a Cu deficient compound, which results in a lowering of the valence band w.r.t. the stoichiometric material. Persson and Zunger also attribute reduced recombination of electrons and holes at the grain boundaries (a kind of interfaces) of polycrystalline CIGS to this hole barrier. Our results for defect calculations in CIGS, that will be presented in Chapter 5, disagree with the existence of an effective hole barrier at the GBs due to extrinsic (Na) doping. We suggest instead that the donor-like surface states near the CBM, related to the BPE, may contribute to type-inversion of interfaces (including GBs) of In-rich CIGS compounds.

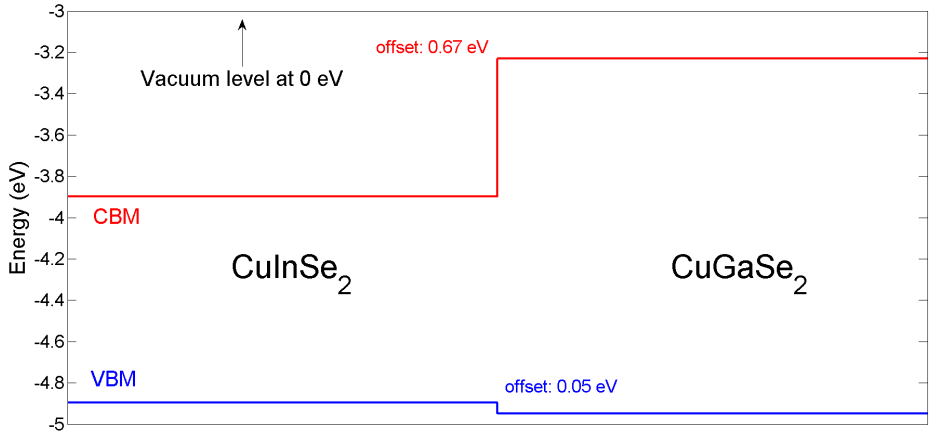

(a) Alignment of CIS and CGS via a slab calculation. The potential in vacuum is set at 0 eV.

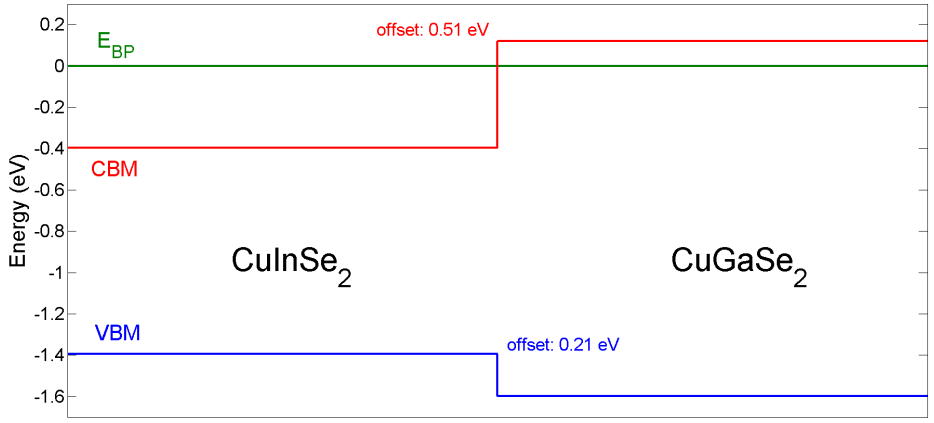

(b) Alignment of CIS and CGS by calculating the BPE using a Green's function.

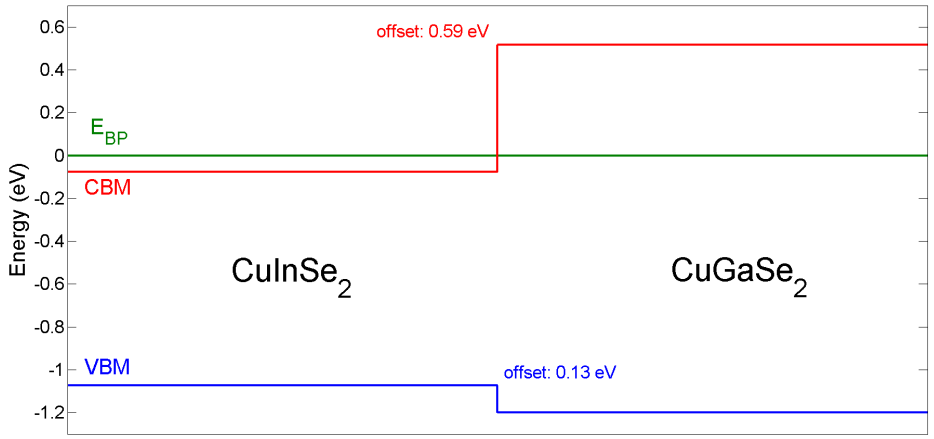

(c) Alignment of CIS and CGS by calculating the BPE using the BZ average of the band structure.

FIGURE 4.4: *Alignment of CIS and CGS by three different methods: via a slab calculation and by calculating the branch-point energy by (i) a Green's function (see Equation 4.2) and (ii) a BZ average of the band structure (see Equation 4.4). The VBM are drawn as blue lines and the CBM as red lines. In (b) and (c) the BPE is set to* 0 *and plotted in green.*

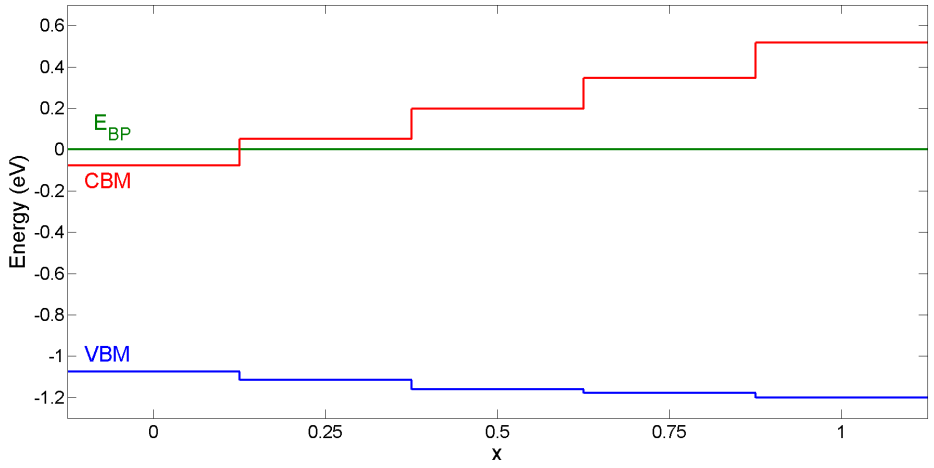

FIGURE 4.5: *Alignment of CIGS compounds with varying Ga content, x. Alloys with $x = 0$, 0.25, 0.5, 0.75 and 1 are included. The alignment is determined by calculation of the branch-point energy via a BZ average of the band structure (see Equation 4.4). The VBM are drawn as blue lines and the CBM as red lines. The BPE is set to 0 and plotted in green.*

Chapter 5

Defect calculations on CIGS

5.1 Introduction

In Chapters 3 and 4 we have studied the properties of pristine CIGS compounds. In this chapter we will explore the effect of *point defects* in CIGS. These point defects may either be *vacancies*, *substitutionals* or *interstitials*. The latter two are examples of impurities or dopants. A substitutional dopant replaces an atom of the pure material, while an interstitial dopant is located on a position that is not a regular lattice site. A vacancy defect is a free lattice site that would be occupied in the stoichiometric material. Our choice of the defects we will discuss, is inspired by their use in photovoltaic (PV) applications. We will start by considering copper (Cu) vacancies, denoted as V_{Cu}, that can result from typically 10 % Cu-deficiency in the synthesis of the CIGS absorber layer [13]. Subsequently, sodium (Na) impurities, more specifically the Na on Cu site substitutional, Na_{Cu} are studied. It is an experimental fact that the incorporation of Na (in the range of $\sim$ 0.1 at.%) in CIGS enhances the efficiency of the PV cell [16]. The mechanism behind this fact is not well understood. We will review some of the propositions based on our results. Finally, we will present a whole range of carbon (C) impurities, both substitutionals and interstitials. This is a subject that is rarely mentioned in the scientific literature. The interest of C defects has been brought to our attention by contacts at Umicore (a materials technology company headquartered in Brussels, Belgium) and IMEC (Interuniversity Microelectronics Centre in Leuven, Belgium). The C impurities may appear in nonvacuum synthesis methods, e.g. printing of an ink containing precursor nanoparticles (a wet method) [12]. In this ink, C atoms

are part of the organic solvents. The main advantage of the nonvacuum processes is a reduced loss of material, compared to losses of 20 to 50 % in vacuum processes. The current maximal conversion efficiency of cells produced using the printing method is 17.1 % (in comparison to 20.4 % in vacuum processes) [19]. More information about (nonvacuum) synthesis methods can be found in Section 1.2.3.2 of Chapter 1.

Defect physics in CIGS has been studied using first-principles methods by A. Zunger and co-workers. S. B. Zhang, S.-H. Wei and A. Zunger have discussed both single defects (e.g. V_{Cu}) and combinations of defects (e.g. $2V_{Cu}^{-}+In_{Cu}^{2+}$) in $CuInSe_2$ (CIS) [22]. Related to the defect combinations, they have introduced the notion of the *ordered defect compound* (ODC) occuring at the grain boundaries (GBs). This ODC would then lead to a hole barrier. The significance of the neutral barriers has been disputed experimentally. Absorbers with positively charged GBs, observed using scanning capacitance microscopy, have been shown to yield the highest efficiency [15]. Computationally, Zunger et al. have used the local density approximation (LDA) functional, correcting for the band gap error by a constant shift of the conduction levels. For all calculations, including those treating combinations of three defects, a supercell of 32 atoms has been chosen. Y.-J. Zhao, C. Persson, S. Lany and A. Zunger have reported on their research on n-type doping of CIGS [23, 70]. They explain the interest in n-type doping pointing out its application in a p-n homojunction. They find that it is harder to n-type dope compounds as their Ga content increases. The reason is the Fermi level being pinned (related to Cu vacancy defects) closer to the CBM in CIS than in CGS. We will demonstrate in this chapter that our own results on Cu vacancies support this conclusion. In the articles discussing n-type conductivity, Zunger and co-workers have employed the LDA functional, corrected for the band gap error by the LDA+U method, and a 64-atom supercell.

Regarding the effect of Na doping in CIS, S.-H. Wei, S. B. Zhang and A. Zunger have distinguished three effects [24]. First, according to Zunger et al., phase segregation of $NaInSe_2$ (NIS) with a larger band gap leads to a higher open-circuit voltage. They also discuss substitutional defects, namely Na_{In} and Na_{Cu}. They find that the former acts as an acceptor, therefore increasing the hole concentration, whereas the latter does not create active electric levels. Finally, Zunger et al. propose that Na residing at the grain boundaries could catalyze the dissociation of O_2 to form O_{Se}. This would prevent the formation of Se vacancies (V_{Se}), that are shallow donors reducing the hole concentration. The results in this article are obtained using the LDA functional, correcting for

the band gap problem by the Xα method. The type of supercell employed for the defect calculations is not mentioned. C. Persson and A. Zunger have found another possible effect of Na doping in CIS: the existence of a *hole barrier* [14], which we have already mentioned in Chapters 1 and 4. This idea is inspired by the experimental observation of type inversion between the interior (p-type) and surface (n-type) of the CIGS absorber layer. Persson and Zunger state that both the neutral defect Na^0_{Cu} and the phase segregated $NaInSe_2$ at the grain boundary produce a hole barrier. The origin of the hole barrier is a lowering of the valence band maximum (VBM) as Cu is replaced by Na, since this removes the *p-d repulsion* present in CIGS compounds. This p-d repulsion is caused by hybridization of Se-4p and Cu-3d levels, which has been discussed in Chapter 3. It leads to a rise of the VBM in CIGS. We will, based on our own data, investigate the possibility of the hole barrier.

Other authors that report on defect properties of $CuInSe_2$ (CIS) and $CuGaSe_2$ (CGS), include T. Maeda and T. Wada [71]. They employ a generalized gradient approximation (GGA) functional, not mentioning any method for treating the band gap error. They make use of a 64-atom supercell, even for calculations on a combination of three defects ($2V^-_{Cu}+In^{2+}_{Cu}$). This raises two major concerns about the results of defect calculations on CIGS found in the scientific literature. First, the calculations are often performed using a LDA or GGA functional, resulting in the well-known band gap problem. Methods for correction include a constant shift of the VB levels, the Xα method, etc. In our calculations we use the tuned hybrid functional that directly yields good values for band gaps. Secondly, the sizes of supercells in which the defect are implemented in the articles we have discussed, tend to be restricted. For example, combinations of three defects are located in 32-atom ([22]) or 64-atom ([71]) supercells. A sufficiently large supercell is needed to (i) approach the single-defect limit and (ii) to reduce the shift of defect levels that lie within the bands, related to the Burstein-Moss shift. We will revisit this question in the next section. Related to this, we have tested $2 \times 2 \times 2$ (64 atoms) and $3 \times 3 \times 3$ (216 atoms) supercells of the 8-atom primitive unit cell of CIGS, for the implementation of single defects. Our approach to defect calculations will be elaborated in Section 5.2 of this chapter. Results for Cu vacancies and Na and C impurities are presented in Section 5.3.

Finally, it is interesting to remark that a link can be made between the band line-up of materials and defect calculations (cfr. Chapter 5). This idea has been elaborated

in the landmark article by C. G. Van de Walle and J. Neugebauer on the alignment of semiconductor and insulator materials based on the defect level due to interstitial hydrogen (H) [72]. This so-called *H level* is determined as the transition level from the +1 to -1 charge state (denoted $\varepsilon\,(+1/-1)$). Van de Walle and Neugebauer have studied the H level of a wide range of materials, including the elemental semiconductors Si and Ge, semiconductor compounds like GaAs and ZnO and the insulators SiO_2 and H_2O. They found that the H level is universally located at ~ -4.5 eV below the vacuum level. The deviation from this value is smaller than 0.5 eV for any material discussed in the article. This can be considered quite accurate, as materials with band gaps of up to ~ 9 eV (SiO_2) are taken into account. Consequently, from the positions of the VBM and CBM, the type of doping due to interstitial H can be (approximately) derived without carrying out an explicit defect calculation. A shallow donor (acceptor) is obtained when the H-level, ~ -4.5 eV, lies close to the CBM (VBM) or within the conduction (valence) band. Extrinsic doping with H falls beyond the scope of this thesis, so we will not review the H level in CIGS.

5.2 Method

5.2.1 Formation energy

The method for the determination of the defect levels relies on the computation of the *formation energy* of defects D in charge state q and will thus be denoted $E^f\,(D^q)$. Early reference for this approach to defect calculations are articles by S. B. Zhang et al. [22, 73]. Recent publications utilizing the concept of the formation energy of defects include work by M. N. Amini et al. and H. Dixit et al. (both on transparent conducting oxides) [74, 75].

The formation energy of a defect D in charge state q, abbreviated D^q, is defined as:

$$E^f\,(D^q) = E_{\text{tot}}\,(D^q) - E_{\text{tot}}\,(bulk) + \sum_\alpha n_\alpha \mu_\alpha + q\,(E_F + E_V + \Delta V)\ . \tag{5.1}$$

In this expression $E_{\text{tot}}\,(D^q)$ is the total energy of the supercell containing the defect and $E_{\text{tot}}\,(bulk)$ is the total energy of the bulk supercell (i.e. without defect). To obtain the formation energy, the chemical potentials of atoms and electrons that are either added

or removed, are to be taken into account. The chemical potentials μ_α of the defect atoms are multiplied by n_α. The absolute value $|n_\alpha|$ is the number of added or removed atoms of element α. If atom α is added $n_\alpha < 0$, if it is removed $n_\alpha > 0$. For electrons, the chemical potential is $(E_F + E_V)$, where E_F is the Fermi level w.r.t. E_V, the top of the valence band of the primitive unit cell. The charge $q < 0$ if electrons are added and $q > 0$ if they are removed. So, for instance, if one electron is removed, the formation energy increases with $(E_F + E_V)$. This is the energy of the electron at the Fermi level. Finally, ΔV is the difference in reference potential of the supercell without defect and with defect.

In conditions of thermodynamic equilibrium, the defect formation energy determines the concentration $c(D^q)$ of defect D^q according to the Boltzmann distribution:

$$c(D^q) = N\ e^{-\frac{E^f}{k_B T}}\ , \tag{5.2}$$

where N is the multiplicity of lattice points per supercell where the defect can be formed. The crucial parameter of this method is E_F. In principle, E_F can be calculated by taking into account every possible point defect with its formation energy. The concentration of defects is restricted by *charge neutrality* in the total system, yielding a value for E_F. Since the number of possible defects is high, this approach is hardly feasible. Instead, we will compute the formation energy of a set of defects in different charge states and plot them as a function of E_F. The graphs of the formation energies are lines with slope q. Naturally, the charge state with the lowest formation energy at given E_F is the ground state. Therefore, the Fermi levels of the intersections of the formation energy, the *transition levels*, are of great importance. They determine the possible occurrence of electrically active defect levels, as we will elaborate in Section 5.2.3. The choice of which charge states $q = .., -2, -1, 0, +1, +2, ..$ are to be considered, can often be limited by the chemical properties of the defect.

5.2.2 Chemical potentials

The chemical potential of an atomic species is the free energy per atom of the species in the reservoir that is in contact with the crystal. As such, it depends on the experimental growth conditions. It is convenient to rewrite the chemical potential as $\mu_\alpha = \mu_\alpha^{elem} + \Delta\mu_\alpha$. Here μ_α^{elem} is the chemical potential of the elemental phase of α. The accessible

chemical potential range for the formation of CIGS compounds is restricted by four constraints [23]. An important notion for the formulation of these restrictions is the *heat of formation*. It is defined as the difference between the total energy of a compound and the energies of the constituent atoms in their elemental standard lattices. It should not be confused with the *cohesive energy*. This is the difference between the total energy of a compound and the energies of the constituent atoms in isolated form ('atom in a box').

The constraints marking the accessible chemical potential range are:

1. In order to *avoid precipitation* of the elemental phase, all chemical potentials μ_α should be lower than μ_α^{elem}:

$$\Delta\mu_{\mathrm{Cu}} \leq 0 \ , \ \Delta\mu_{\mathrm{In/Ga}} \leq 0 \ , \ \Delta\mu_{\mathrm{Se}} \leq 0. \tag{5.3}$$

   If $\Delta\mu_\alpha = 0$, then maximum α-rich conditions are implied.

2. To form and maintain a *stable compound*, the sum of the relative chemical potentials $\Delta\mu_\alpha$ should equal the heat of formation ΔH^f of the compound. In case of CIGS:

$$\Delta H^f(\mathrm{CIGS}) = \Delta\mu_{\mathrm{Cu}} + \Delta\mu_{\mathrm{In/Ga}} + 2\Delta\mu_{\mathrm{Se}}. \tag{5.4}$$

3. The formation of undesired *competing phases* also lays a restriction on the accessible chemical potentials for CIGS compounds. For CIS, competing phases are e.g. Cu_2Se, In_2Se_3 etc., while for CGS examples include Cu_2Se, Ga_2Se_3 [23].

4. Additionally, in case of doping, one can require that no compounds should form between dopant and host atoms. We will study the example of $NaInSe_2$ when discussing Na doping.

We will only consider constraints 1 and 2. In order to determine μ_α^{elem}, calculations of the total energy of Cu, In, Ga and Se in elemental metal form have to performed. Moreover, the same type of calculation is done for Na and C, as they will be studied as dopants. The space symmetries of the elemental metals is obtained from Ref. [76]. For C, graphite is selected as the elemental solid. The atomic structures of the elemental solids are relaxed using a conjugate-gradient algorithm until all force components are smaller than 0.01

Metal	Space symmetry (Hermann-Mauguin notation)	lattice parameters (Å)
Cu	$Fm\bar{3}m$ (No. 225, FCC)	$a = b = c = 3.642$
In	I4/mmm (No. 139, TET)	$a = b = 3.268$, $c = 5.017$
Ga	Cmca (No. 64, ORT)	$a = 4.507$, $b = 7.661$, $c = 4.553$
Se	$P3_121$ (No. 152, TRI)	$a = b = 4.822$, $c = 4.886$
Na	$Im\bar{3}m$ (No. 229, BCC)	$a = b = c = 4.230$
C	$P6_3/mmc$ (No. 194, HEX)	$a = b = 2.452$, $c = 7.361$

TABLE 5.1: *Structural properties of elemental solids calculated with the HSE06 functional for the determination of the chemical potentials.*

eV/Å. The total energy calculations are performed using the HSE06 functional. It is necessary the same type of functional is used in the impurity calculations, so the energy reference is identical. For the calculation of the electronic structure of metals, typically very dense k-point meshes are required. As an example, for Cu a $16 \times 16 \times 16$ Γ-centered Monkhorst-Packgrid has been selected. The space symmetries and calculated lattice parameters of the elemental solids are listed in Table 5.1.

In order to judge whether the computed chemical potentials are reasonable, a comparison can be made of the theoretical and experimental heat of formation. The theoretical heat of formation is calculated from the chemical potentials using constraint No. 2. For CIS:

$$\begin{aligned} \Delta H^f(\mathrm{CIS}) &= E_{tot}(\mathrm{CIS}) - \frac{E_{tot}^{elem}(\mathrm{Cu})}{\mathrm{atom}} - \frac{E_{tot}^{elem}(\mathrm{In})}{\mathrm{atom}} - 2\frac{E_{tot}^{elem}(\mathrm{Se})}{\mathrm{atom}} \\ &= \Delta\mu_{\mathrm{Cu}} + \Delta\mu_{\mathrm{In}} + 2\Delta\mu_{\mathrm{Se}} \end{aligned} \tag{5.5}$$

and analogously for CGS. In this way we find theoretically that the heat of formation of the unit formula of CIS is -3.07 eV and that of CGS is -4.00 eV. Experimental values are given in Ref. [77]. The experimental heat of formation of CIS is -267 kJ/mol (-2.77 eV), that of CGS is -317 kJ/mol (-3.29 eV). This means that the relative deviation of the theoretical values from the experimental ones is respectively 11 % and 22 % for CIS and CGS. We may conclude that there is good agreement between computed values of the chemical potentials of the constituent atoms of CIGS and the experimental heat of formation.

The ranges of accessible chemical potential of CIS and CGS can now be represented by two *stability triangles*. The triangle is drawn as a function of $\Delta\mu_{\mathrm{Cu}}$ and $\Delta\mu_{\mathrm{In/Ga}}$, leaving $\Delta\mu_{\mathrm{Se}}$ as a dependent variable, due to constraint No. 2. The stability triangles are shown

in Figure 5.1. A stability triangle including competing phases can for instance be found in Ref. [23].

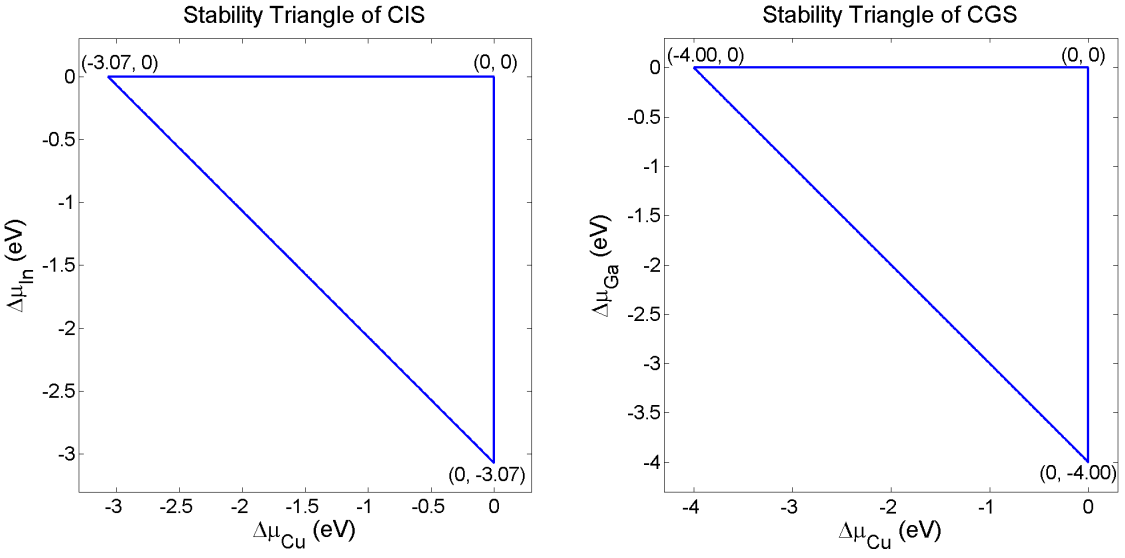

(a) CIS (b) CGS

FIGURE 5.1: *The stability triangles of CIS and CGS as a function of* $\Delta\mu_{Cu}$ *and* $\Delta\mu_{In/Ga}$*. The vertex* $(0,0)$ *corresponds to Cu-rich and In/Ga-rich conditions. The vertices* $(-3.07,0)$ *and* $(-4.00,0)$ *are Cu-poor and In/Ga-rich, while the vertices* $(0,-3.07)$ *and* $(0,-4.00)$ *are Cu-rich and In/Ga-poor. The lines connecting* $(-3.07,0)/(-4.00,0)$ *and* $(0,-3.07)/(0,-4.00)$ *give maximal Se-rich conditions.*

5.2.3 Transition levels

The transition level between different charge states of a defect is defined as the value of E_F at the intersection of the corresponding formation energy graphs. We denote a transition between charge states q and q' as $\varepsilon(D, q/q')$. The transition level $\varepsilon(D, q/q')$ occurs when the defect states with charges q and q' have equal formation energy, i.e. $E^f(D^q) = E^f(D^{q\prime})$. Using Equation 5.1 of the formation energy, this leads to:

$$\varepsilon(D, q/q') = \frac{E_{tot}(D^q) - E_{tot}(D^{q'}) + q\Delta V^q - q'\Delta V^{q'}}{q' - q} - E_V \ , \tag{5.6}$$

where ΔV^q ($\Delta V^{q'}$) is the correction for the reference potential for charge state q (q').

The transition levels are important in the analysis of the defects. Their position relative to the valence and conduction band determines the possible electrical activity of the defect state. Different cases for the position of the defect levels relative to the valence

and conduction band are depicted in Figure 5.2. The defect levels are represented by non-dispersive states, since they can considered to be highly localized. If a transition to a ground state with negative charge occurs near the VBM, the defect level is an *acceptor level*. The resulting p-type conductivity is a consequence of the holes that are left as the electron has moved to the defect level. A *donor level* is analogously defined as a transition to a positive charge state near the CBM. The corresponding n-type conductivity is related to the (semi-)free electrons in the conduction band, originating from the donor level.

In Figure 5.2 it is also shown that defect levels can appear within the valence or conduction band. Given the limited extent of the band gap, this scenario is often more likely than a level in the gap. A level in the valence (conduction) band with a negatively (positively) charged ground state is an acceptor (donor) level. The holes (electrons) occupying the defect level in the valence (conduction) band naturally relax to the VBM (CBM), as can be seen in the figure.

An important distinction to be made, is between *shallow* and *deep* levels. A shallow defect level is likely to be thermally ionized at relevant temperatures. This is typically chosen to be room temperature, 293 K, corresponding to an energy of ~ 25 meV. Therefore, an acceptor (donor) level within 25 meV of the VBM (CBM) will be called a shallow level [1]. Of course, an acceptor (donor) level within the valence (conduction) band is a shallow level as well. On the other hand, an acceptor (donor) level within the band gap, separated by more than 25 meV from the valence (conduction) band, is a deep level.

We wish to remark that we are not able to fully describe the system of ionized defects and semi-free charge carriers. It is a so-called *effective mass state*, an extended state that does not fit in a regular supercell. Hence, it cannot be treated easily using DFT. The extension of the effective mass state is smaller in a nanoparticle. So, by implementing a nanoparticle with a radius corresponding to the Bohr-radius of the hydrogen-like interaction, the effective mass state can be treated in DFT after all. This approach is outside of the scope of this thesis.

[1] There is no absolute consensus on this terminology in the scientific literature. The choice will depend on the temperature of the application and in second place on the interpretation of 'likely'. The criterion for a shallow level usually ranges between 25 and 100 meV in the literature. In selecting the former, we imply that at room temperature at least $\exp(-1) \approx 37$ % of the defects should be ionized according to the Boltzmann distribution.

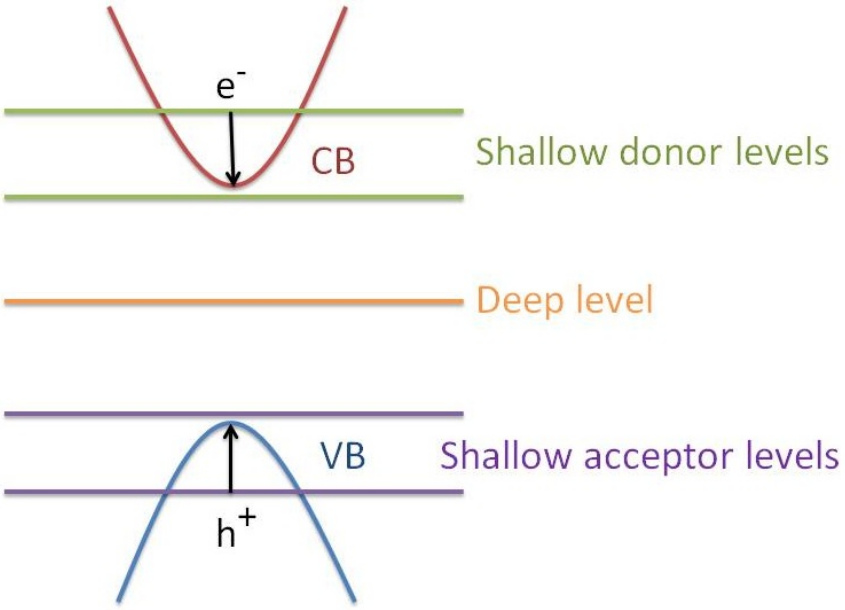

FIGURE 5.2: *A schematic representation of defect levels occuring in a band structure. Instances of donor and acceptor levels and shallow and deep levels are given.*

Electrically active defect levels can be experimentally probed using deep-level transient spectroscopy (DLTS) [75]. In one possible set-up, defects in a p-n junction under reverse bias are subject to a series of periodic voltage pulses [12]. These force the charge carriers from the bulk material to occupy the ionized defect levels. As the pulse ceases, the trapped charge carriers are re-emitted thermally. Subsequently, a transient in the capacitance of the junction appears. From the characteristics of this transient both the defect level and defect concentration can be obtained.

5.2.4 Computational details

Defect calculations in this thesis are performed using a tuned HSE06 functional, since in defect studies correct values of the band gaps are crucial. We remind that the resulting band gap of CIS, CIGS with $x = 0.5$ and CGS are respectively 1.00 eV, 1.36 eV and 1.72 eV (See Section 3.3.1 of Chapter 3). As is the case throughout the thesis, electron-ion interactions are treated using projector augmented wave (PAW) potentials. Integration over the Brillouin zone is achieved on a $2 \times 2 \times 2$ Γ-centered Monkhorst-Pack grid. The energy cutoff of the plane wave basis is 500 eV. The integration is facilitated by Gaussian

smearing with a width of $\sigma = 0.2$ eV. To filter out the effect of the smearing, the total energy is extrapolated for $\sigma \to 0$ (as implemented in VASP) [39]. The charge of the state is simply accomplished by adding $q = .., -2, -1, 0, +1, +2, ..$ electrons to the supercell.

The supercells containing defects are relaxed using the conjugate-gradient algorithm (CGA) until all force components are smaller than 0.05 eV/Å. In this relaxation the volume of the supercell is kept constant, optimizing only the atomic positions. Every charge state has to be relaxed separately. In large supercells relaxation is not a trivial task. Therefore we apply a reduction in the evaluation of the Hartree-Fock kernel by a factor 2 during relaxation. This is supplied in VASP by the function 'NKRED' [42]. However, this reduction should be omitted in the final self-consistent calculation yielding the electronic structure of doped systems. This is illustrated for Cu vacancies in Table 5.2. The transition level $\varepsilon(\mathrm{V_{Cu}}, 0/-1)$ alters from -0.155 eV to -0.212 eV as the reduction on the Hartree-Fock kernel is omitted. Consequently, we calculate the total energies for the defect formation energies by evaluating the Hartree-Fock kernel on the full k-point grid.

NKRED	Supercell	$\varepsilon(\mathrm{V_{Cu}}, 0/-1)$ (eV)
yes	$2 \times 2 \times 2$	-0.155
no	$2 \times 2 \times 2$	-0.212
no	$3 \times 3 \times 3$	-0.095

TABLE 5.2: *Values for the transition level from the* 0 *to* -1 *charge state of the Cu vacancy defect for different computational approaches w.r.t. the VBM (at* 0 *eV).*

5.2.4.1 Supercell size

The size of the supercell in which the defect is implemented is important for two reasons. First, the supercell should be chosen large enough in order to approximate the single-defect limit. Most calculations within this thesis are carried out using a $2 \times 2 \times 2$ supercell of the 8-atom primitive unit cell. This means that this supercell contains 64 atoms. To assess the influence of the size of the supercell, we have performed calculations on a $3 \times 3 \times 3$ supercell, containing 216 atoms for the $\mathrm{V_{Cu}}$ defect in CIS. The defect concentration using the $2 \times 2 \times 2$ is $7.04 \cdot 10^{20}$ cm^{-3} for defects in CIS and $6.26 \cdot 10^{20}$ cm^{-3} in CGS. This concentration decreases to $1.86 \cdot 10^{20}$ cm^{-3} in CIS as the $3 \times 3 \times 3$ supercell is selected. This still exceeds the dilute limit for doping, which is below 10^{18} cm^{-3} [23].

This limit is hardly computationally accessible at present, especially in combination with a hybrid functional. We can study the influence of the supercell size by comparing the results obtained with $2 \times 2 \times 2$ and $3 \times 3 \times 3$ supercells.

A second phenomenon related to the size of the supercell, is schematically depicted in Figure 5.3. The example of a donor level within the conduction band is given. As the supercell size increases, the Brillouin zone is folded. Owing to the preservation of the filling, there is a downwards shift of the Fermi energy in the conduction band. Analogously, the Fermi energy in the valence band (related to an acceptor level) is shifted upwards as the size of the supercell is increased. The modified filling of the bands compared to the bulk band structure leads to an *apparent* increase of the band gap in optical experiments, the so-called *Burstein-Moss shift* [78].

The transition level $\varepsilon(\mathrm{V_{Cu}}, 0/-1)$ using the $2\times2\times2$ and $3\times3\times3$ supercell are tabulated in Table 5.2. It shifts from -0.212 eV to -0.095 eV, mainly an effect of the filling upon BZ folding. It should be noted that the exact energy of the transition level within the valence band is not greatly relevant, since in practice the hole relaxes to the VBM. It is, however, a good measure for the influence of the supercell size. The formation energy plots of $\mathrm{V_{Cu}^{-}}$ in CIS in $2 \times 2 \times 2$ and $3 \times 3 \times 3$ supercells are shown in Figure 5.5 (a) and (b). We see that the conclusion of Cu vacancies being shallow acceptor levels in CIS is not altered. Therefore, we can conclude that the $2 \times 2 \times 2$ supercell is sufficiently large for single-defect calculations. All remaining defect calculations are thus executed employing $2 \times 2 \times 2$ supercells.

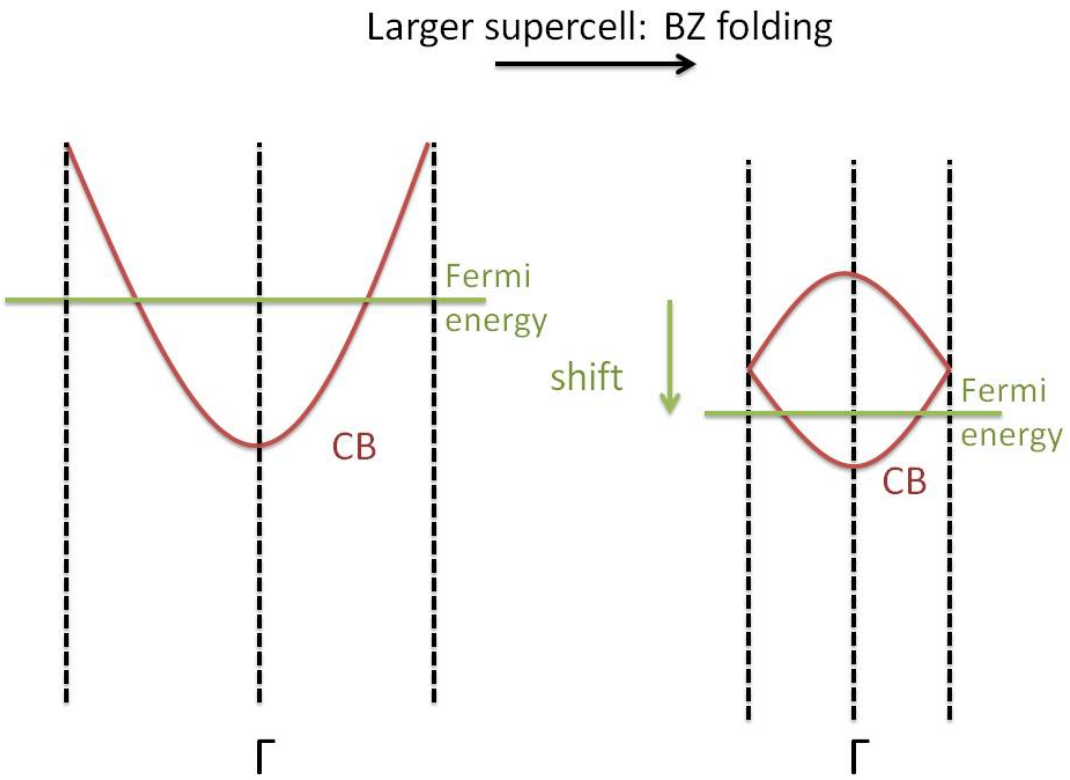

FIGURE 5.3: *Schematic representation of the downwards shift of the Fermi energy within the conduction band as the supercell size increases (folding of the BZ).*

5.2.4.2 Reference potential

As mentioned when Equation 5.1 for the formation energy was introduced, a correction term has to be included for the reference potential. Due to the finite size of the supercell, the undoped and doped supercells have a different reference potential. In order to accurately calculate the formation energy, this has to be taken into account. There are several possible methods to achieve this. Usually, one aligns the electrostatic potential far away from the defect with the potential in the same point(s) in the undoped supercell. We have, however, selected another procedure which is independent of the position of the defect and can thus be carried out very efficiently. One starts by calculating the difference between the electrostatic potential in the supercell without defect and with defect, $V_u(\mathbf{r}) - V_d(\mathbf{r})$, on a grid of points in the supercell. Since the distortion due to the defect is supposed to be limited in space, then ΔV, the difference in reference potential, is the most likely value of $V_u - V_d$. Subsequently a histogram of $V_u - V_d$ is made using the linear tetrahedron method [74]. This method yields the volume in space belonging

to each value of $V_u - V_d$. These volumes are used as 'counts' to construct the histogram. Since ΔV is the most likely value it corresponds to the value of $V_u - V_d$ at the peak of the histogram. An example of a histogram achieved by this approach is shown in Figure 5.4.

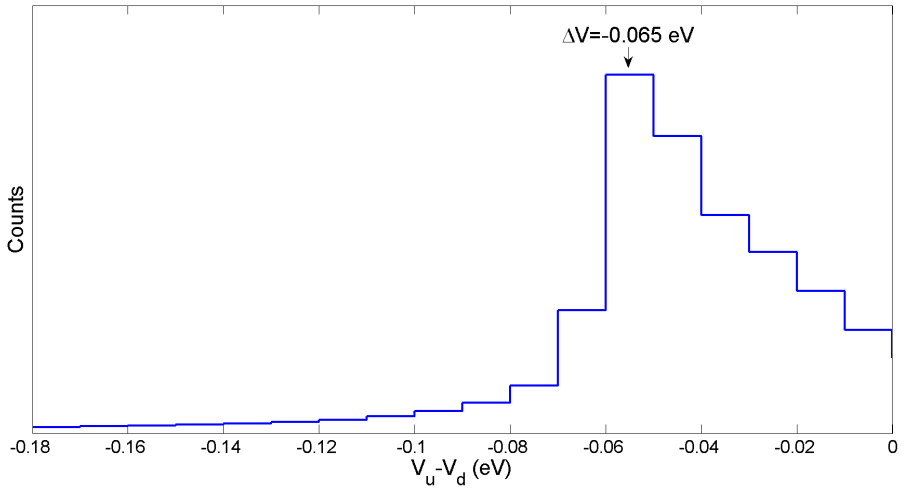

FIGURE 5.4: *Histogram for the determination of ΔV. This particular example originates from the computation of the V_{Cu}^{-} defect in the $3 \times 3 \times 3$ supercell. The result is $\Delta V = -0.065 \pm 0.005$ eV.*

5.3 Results

5.3.1 Copper vacancies

We start our investigation of the defect properties of CIGS compounds with one Cu vacancy, V_{Cu} in a $2 \times 2 \times 2$ supercell. In case of CIS we have also tested the $3 \times 3 \times 3$ supercell. As mentioned in the introduction, they are prevalent due to Cu-deficiency conditions during growth of the common CIGS PV absorber layers. We study $CuInSe_2$ (CIS), $CuIn_{0.5}Ga_{0.5}Se_2$ (CIGS with $x = 0.5$) and $CuGaSe_2$ (CGS) [2].

The relaxed structure of the environment of a V_{Cu} defect is shown in Figure 5.5. The lattice is distorted in a way that the Se atoms that miss a bond due to the vacancy relax by a small amount towards the center of the vacancy. This amount is consistently smaller than 0.1 Å for all compounds. All values are listed in Table 5.3. There is also a slight effect on the interatomic distance between the Se atom and the two In atoms it is bound to. We treat the example of the vacancy in CIS. The unperturbed distance is $d^u_{\text{In}-\text{Se}} = 2.609$ Å for both In atoms. Owing to the defect this alters to $d^d_{\text{In}-\text{Se}} = 2.567,\ 2.571$ Å (in case of the ground state $q = -1$). Se is thus bound a bit more tightly to In due the Cu vacancy. Since formally the oxidation state of Cu in CIGS is $+1$, it is sensible to take into account the formation energy $q = -1, 0, +1$ states. The formation energies of CIS, CIGS with $x = 0.5$ and CGS are displayed in Figure 5.5. The $q = -1$ state is the ground state for every possible E_F in the band gap. This is not surprising, because the removed Cu atom was an electron donor. To compensate for the lack of this Cu atom, the V_{Cu} is an electron acceptor. The consequence is that V_{Cu} is a *shallow acceptor* level in all compounds. This conclusion does not alter upon switching from a $2 \times 2 \times 2$ supercell to a $3 \times 3 \times 3$ supercell. We have tested this for CIS (see (b)). The transition level increases $\varepsilon(0/-1)$ when a larger supercell is selected, due to the shift related to the filling, which was explained in Section 5.2.4.1. The relevant transition levels, between two ground states, are listed in Table 5.4.

The formation energy of V_{Cu} is generally rather low, even under Cu-rich conditions. Since Cu is removed and $\Delta\mu_{Cu} \leq 0$ for a stable compound, the formation energy of all charge states goes *down* uniformly, if more Cu-poor conditions are present. To give an

[2] As we have explained in Chapter 3, the compound with $x = 0.5$ can come in two varieties, depending on the sequence of the In and Ga atoms. Both In-Ga-In-Ga and In-In-Ga-Ga are possible. Within the chapter on defect calculations we have selected the former.

example, in thermal equilibrium at 550°C, the concentration of V_{Cu} is 10^{18} cm^{-3} in case $\Delta\mu_{Cu} = -0.76$ eV for CIS and $\Delta\mu_{Cu} = -0.94$ eV for CGS. These chemical potentials are well attainable, according to the stability triangles of CIS and CGS (cfr. Figure 5.1). Consequently, Cu vacancies are likely to be formed in Cu-poor conditions. They result in the p-type conductivity of the bulk of the CIGS absorber layers. The formation energy of V_{Cu} near the CBM is lower in CGS than in CIS, due to the former's larger band gap. Since it has a negative formation energy in CGS, V_{Cu}^{-} forms spontaneously if E_F is close to the CBM. In this case, it kills the electrical activity of possible donor states. Therefore, it is harder to n-type dope CGS than CIS. This has also been reported by Zunger et al. [23, 70]. A p-n homojunction of CIGS can as a consequence be realized more easily given the compound contains more In than Ga.

Compound	d^u_{Cu-Se}(Å)	$d^d_{V_{Cu}-Se}$(Å)
CIS	2.456	2.393
CIGS with $x = 0.5$	2.460	2.400
CGS	2.440	2.346

TABLE 5.3: *Interatomic distances in the unperturbed (bulk) lattice, d^u_{Cu-Se}, and in the lattice with a V_{Cu} defect, $d^d_{V_{Cu}-Se}$, for $q = -1$ (the ground state). The latter distance is the distance between the center of the vacancy and the adjacent Se atoms.*

Compound	Supercell	Transition	Energy (eV)
CIS	$2 \times 2 \times 2$	0/-1	-0.212
CIS	$3 \times 3 \times 3$	0/-1	-0.095
CIGS with $x = 0.5$	$2 \times 2 \times 2$	0/-1	-0.233
CGS	$2 \times 2 \times 2$	0/-1	-0.216

TABLE 5.4: *Relevant transition levels for a V_{Cu} defect w.r.t. the VBM.*

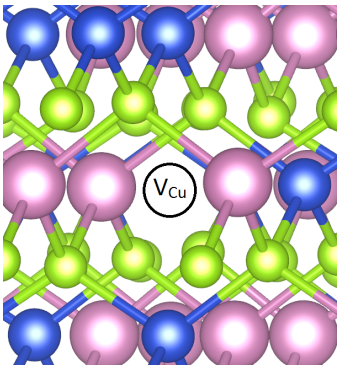

FIGURE 5.5: *Relaxed environment of a V_{Cu} defect in CIS. Cu atoms are colored blue, In pink and Se green.*

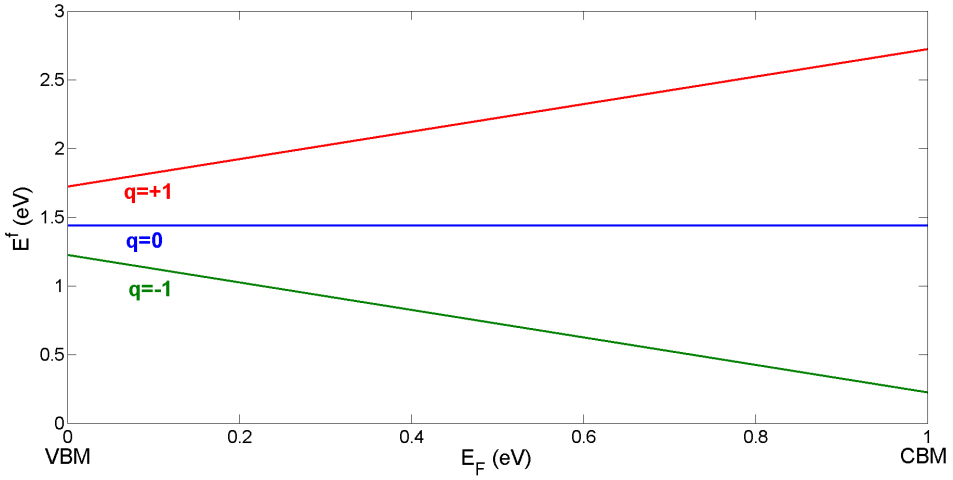

(a) CIS with $2 \times 2 \times 2$ supercell

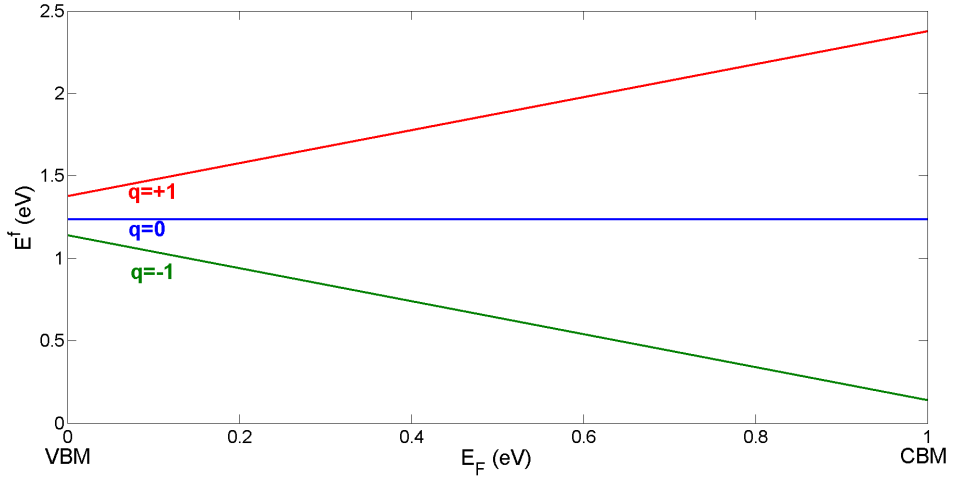

(b) CIS with $3 \times 3 \times 3$ supercell

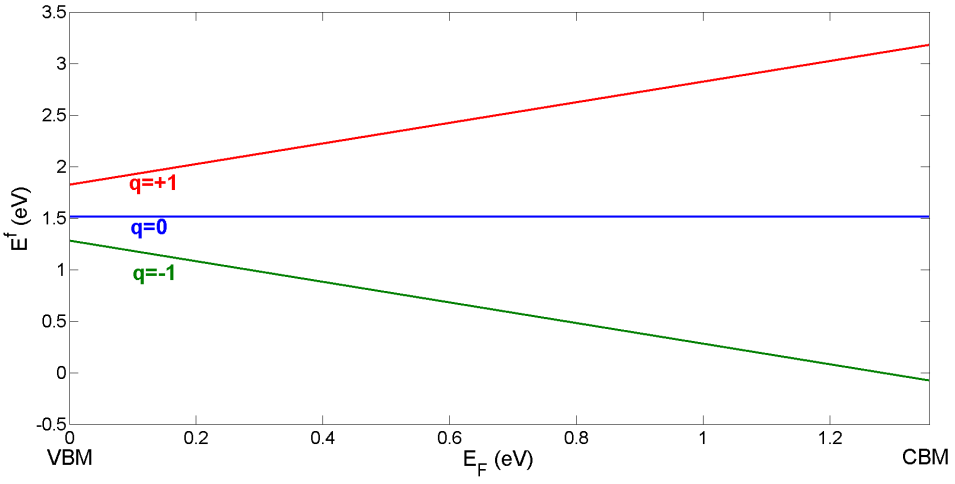

(c) CIGS with $x = 0.5$

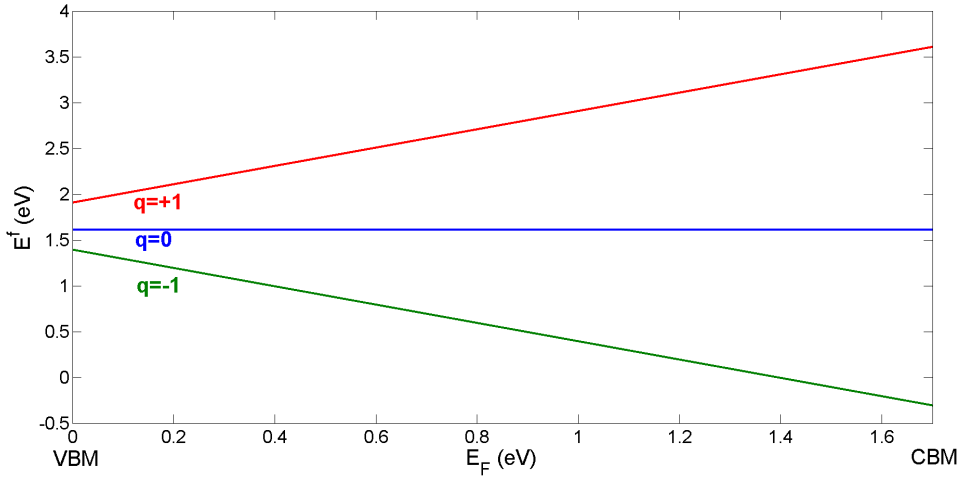

(d) CGS

FIGURE 5.5: *Formation energies E^f (eV) of the V_{Cu} defect in different compounds as a function of the Fermi level E_F (eV) between the VBM and the CBM.*

5.3.2 Sodium impurities

5.3.2.1 Substitutional sodium on copper site

As mentioned before, the benign effect of Na doping (~ 0.1 at.%) on the performance of CIGS PV devices is an experimental fact [16]. Numerous experimental and theoretical studies have attempted to find the origin of this effect [14, 24]. Still, no real consensus has been reached. We contribute to this discussion by investigating the Na_{Cu} substitutional. This choice is again inspired by the general Cu-deficiency in CIGS. The electronic configuration of Na is [Ne] $\underline{3s^1}$, where the underlined electron is treated as a valence electron in the PAW potential.

The Na substitutional and its relaxed environment are depicted in Figure 5.6. A clear measure of the relaxation of the lattice around the defect are the interatomic distances of the surrounding atoms. In this case, how the Cu-Se distance is modified by replacing Cu by Na (for the ground state with $q = 0$). In Table 5.5 one finds that this distance increases by 0.25 Å or less.

The formation energies for CIS, CIGS with $x = 0.5$ and CGS are displayed in Figure 5.7. They are obtained in Cu-rich and Na-rich conditions. In all cases the ground state in the gap is neutral, $q = 0$. The transition levels between the ground states in the bands

are shown in Table 5.6 for completeness. The +1/0 transition occurs within the valence bands and the 0/-1 transition within the conduction bands. They do not give rise to any electrical activity.

The formation energy of the Na^0_{Cu} defect is negative, so the defect forms spontaneously. Then, one can consider that in typical production methods of CIGS, Na diffuses from the sodium lime glas substrate [16]. Therefore, the reservoir resembles isolated Na more closely than elemental solid Na (Na-rich conditions). We have computed the chemical potential of isolated Na by enclosing it in a box with edge 30 Å, that otherwise contains only vacuum. A spin-polarized calculation of the total energy is selected, as Na has an unpaired valence electron. For this type of computation only one k-point, the Γ point, is required. It is found that using these conditions, the formation energy lowers uniformly for all charge states by 1.06 eV. The Na^0_{Cu} defect is consequently readily formed, yet does not contribute to the electrical conductivity of the layer.

Compound	d^u_{Cu-Se}(Å)	d^d_{Na-Se}(Å)
CIS	2.456	2.694
CIGS with $x = 0.5$	2.460	2.706
CGS	2.440	2.666

TABLE 5.5: *Interatomic distances in unperturbed (bulk) lattice, d^u_{Cu-Se}, and in the lattice with Na_{Cu} defect, d^d_{Na-Se}, for $q = 0$ (the ground state).*

Compound	Transition	Energy (eV)
CIS	+1/0	-0.017
	0/-1	1.883
CIGS with $x = 0.5$	+1/0	-0.014
	0/-1	2.163
CGS	+1/0	-0.418
	0/-1	2.062

TABLE 5.6: *Relevant transition levels for a Na_{Cu} defect w.r.t. the VBM.*

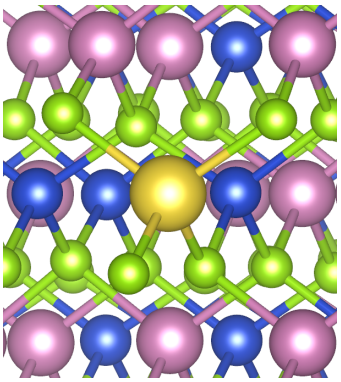

FIGURE 5.6: *Relaxed environment of the Na_{Cu} defect in CIS. The different atoms are: Cu (blue), In (pink), Se (green) and Na (yellow).*

5.3.2.2 The existence of a hole barrier

A model for the benign effect of Na on the grain boundaries of polycrystalline CIGS has been suggested by Persson and Zunger [14]. They propose a hole barrier by Na^0_{Cu} defect at the grain boundary (GB) and by phase segragation of a compound formed between host and dopant, namely $NaInSe_2$ (NIS). The idea behind the hole barrier is a lowering of the VBM as Cu is replaced by Na due to the reduction in p-d repulsion. We did not find evidence from our results that supports the formation of a hole barrier owing to Na^0_{Cu}. The reason is that in studying single point defects it is implied that the bulk band structure is negligibly perturbed. Persson and Zunger argue that Na doping in small quantities leads to reconstruction at the GB. This stacking fault would, according to them, lead to a neutral barrier at the GB. There is no clear experimental evidence to support this hypothesis, as is established in Ref. [15].

In the presence of larger quantities of Na, Persson and Zunger predict the formation of $NaInSe_2$ (NIS) at the GBs. This is in a way supported by experimental work by D. Rudmann, comparing different methods for incorporation of Na in CIGS [79]. He could conclude that the solubility of Na in CIGS is low, causing Na to reside at the GBs. However, segregation of NIS is not explicitly mentioned, as no direct imaging of the GB structure was performed. We present a study of NIS using the HSE06 functional, based on which we can align NIS and CIS, directly showing whether this leads to an effective hole barrier.

The space group of NIS in Hermann-Mauguin notation is $R\bar{3}m$ (No. 166, TRI) [76, 80]. The positions of the atoms in this structure are listed in Table 5.7 and the conventional

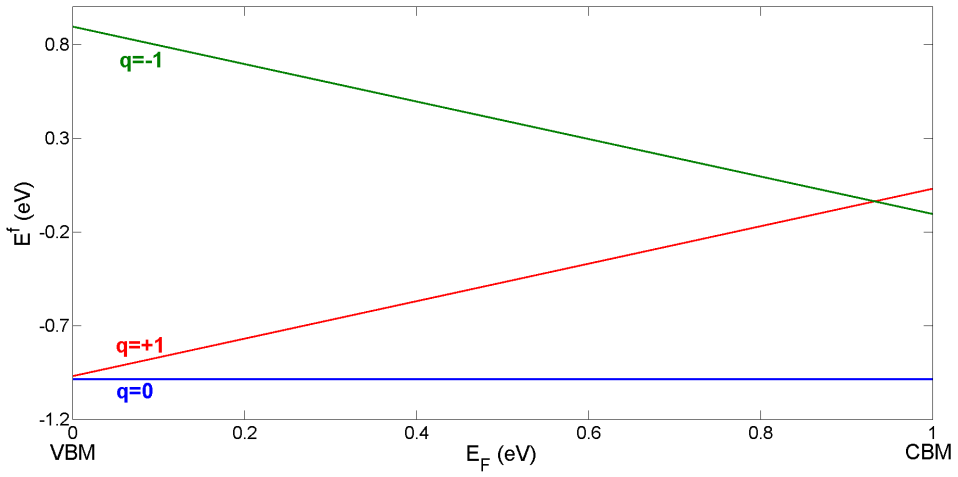

(a) CIS

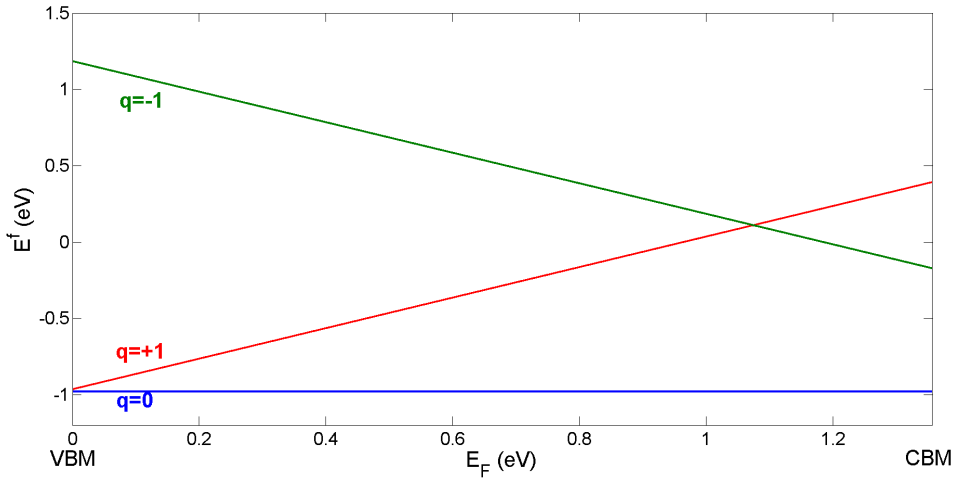

(b) CIGS with $x = 0.5$

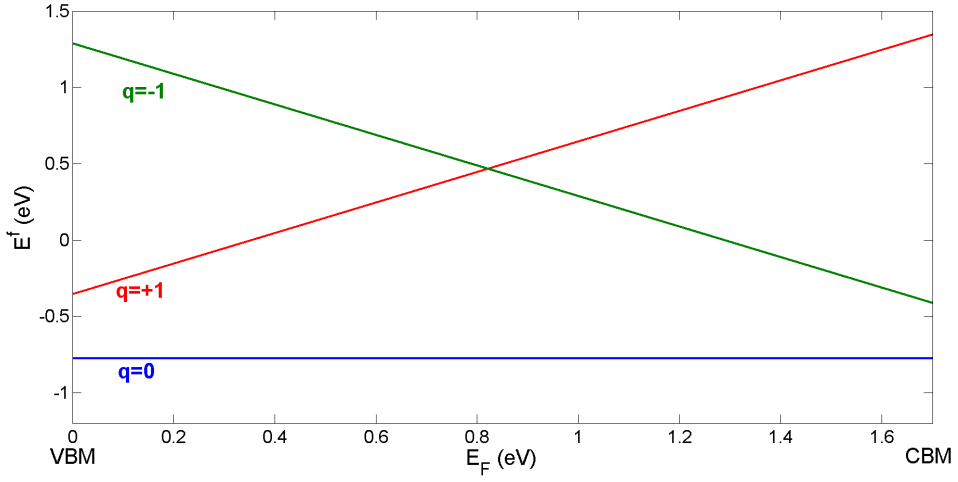

(c) CGS

FIGURE 5.7: *Formation energies E^f (eV) of the Na_{Cu} defect in different CIGS compounds as a function of the Fermi level E_F (eV) between the VBM and CBM.*

unit cell of NIS is shown in Figure 5.8. We theoretically obtain lattice parameters $a = b = 3.981$ Å, $c = 20.894$ Å and parameter $z = 0.260$. These agree well with experimental values $a = b = 3.972$ Å, $c = 20.890$ Å and parameter $z = 0.260$ [76].

The heat of formation of NIS obtained from the hybrid treatment is:

$$\begin{aligned}\Delta H^f(\text{NIS}) &= E_{tot}(\text{NIS}) - E_{tot}^{isol}(\text{Na}) - \frac{E_{tot}^{elem}(\text{In})}{\text{atom}} - 2\frac{E_{tot}^{elem}(\text{Se})}{\text{atom}} \\ &= -5.36 \text{ eV} \ .\end{aligned} \tag{5.7}$$

In this calculation $E_{tot}^{isol}(\text{Na})$ is the total energy of an isolated Na atom. The purpose is to mimic the incorporation of Na in the common growth methods. We can estimate the tendency for phase segregation of NIS by calculating the mixing enthalpy:

$$\Delta H = E_{tot}\left(\text{NaCu}_{15}\text{In}_{16}\text{Se}_{32}\right) - \frac{1}{16}E_{tot}\left(\text{Na}_{16}\text{In}_{16}\text{Se}_{32}\right) - \frac{15}{16}E_{tot}\left(\text{Cu}_{16}\text{In}_{16}\text{Se}_{32}\right) \ , \tag{5.8}$$

where $E_{tot}\left(\text{NaCu}_{15}\text{In}_{16}\text{Se}_{32}\right)$ is the total energy of the structure with the $\text{Na}_{\text{Cu}}^{0}$ defect in the $2 \times 2 \times 2$ supercell and $E_{tot}\left(\text{Na}_{16}\text{In}_{16}\text{Se}_{32}\right)$ and $E_{tot}\left(\text{Cu}_{16}\text{In}_{16}\text{Se}_{32}\right)$ are the total energies of NIS and CIS scaled to the $2 \times 2 \times 2$ supercell. The result is that the mixing enthalpy is 15.2 meV per mixing atom (Na and Cu). It is positive, so mixing does not occur spontaneously. This can be the reason why one finds that the solubility of Na in CIGS is low.

The hypothesis that formation of NIS at the GB results in a hole barrier can be tested by aligning the band structures of NIS (GB) and CIS (GI). We find that NIS has a considerably larger band gap of 2.26 eV, compared to CIS with a gap of 1.00 eV. We align NIS and CIS by calculating the branch-point energy (BPE) by a weighed average over the BZ of the bulk band structure. We have explained this method extensively in Chapter 4. The number of bands used in the average is chosen following Schleife et al. [21]. Consequently, we use 12 valence bands and 6 conduction bands for the BPE of NIS and 16 valence bands and 8 conduction bands for CIS. The alignment is shown in Figure 5.9. It is straddling (type-I) with an offset of 0.51 eV between the valence bands and 0.75 eV between the conduction bands.

It is unsure whether Persson and Zunger have taken into account that NIS has a considerably larger band gap than CIS. The removal of the p-d repulsion due to Cu indeed leads to a lowering of the VBM as Cu in the formation of NIS. Yet, due to the larger

band gap of NIS, the alignment is not staggered (type-II) but straddling (type-I). A staggered alignment indeed separates electrons and holes in opposite directions. The straddling alignment, however, does not lead to an effective hole barrier. Both electrons and holes are confined to the grain interior. There is no reduced recombination of electrons and holes resulting from this scenario and moreover electrical conductivity across the grain boundaries is strongly suppressed. This leads to the conclusion that phase segregation of NIS at the grain boundary, as suggested by Persson and Zunger, is very unlikely to be beneficial for the performance of the device. Larger concentrations of Na (beyond 0.1 at%) are indeed observed to have a negative effect on the efficiency of CIGS absorber layers [12]. Our calculations show one possible advantage of NIS, provided it is not present in excess at the grain boundaries. Namely, due to its large band gap, it may lead to an increase of the open circuit voltage of the PV device.

Element	Wyckoff position	Coordinate
In	3a	(0,0,0)
Na	3b	$(0, 0, \frac{1}{2})$
Se	6c	(0,0,z), (0,0,-z)

TABLE 5.7: *Wyckoff positions and coordinates of the atoms in $NaInSe_2$ (NIS) in the* $R\bar{3}m$ *(No. 166, TRI) space structure [76, 80]. The coordinates are given in terms of the rhombohedral primitive lattice vector [49].*

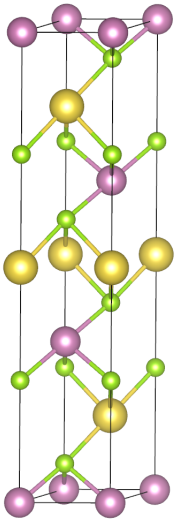

FIGURE 5.8: *Conventional unit cell of NIS in the* $R\bar{3}m$ *(No. 166, TRI) space structure. The conventional unit cell contains 3 Na atoms (yellow), 3 In atoms (pink) and 6 Se atoms (pink).*

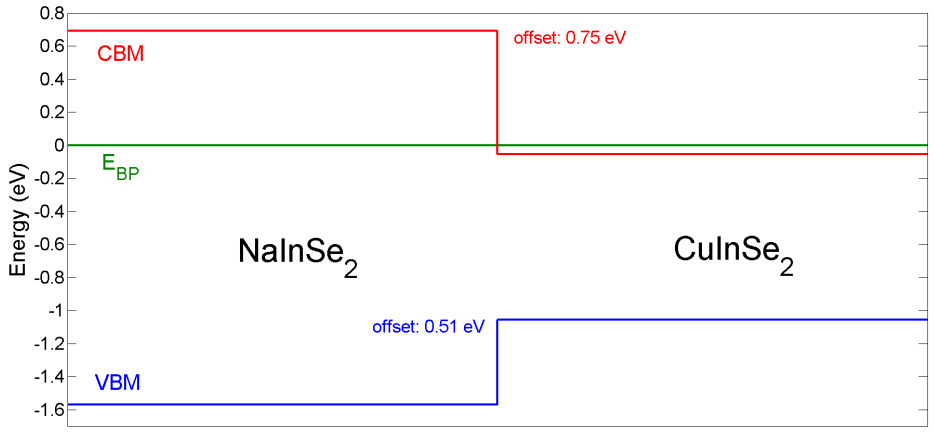

FIGURE 5.9: *Alignment of NIS (at the grain boundary) and CIS (in the grain interior) using a branch-point energy (BPE) method. The BPE is set at* 0 *eV. The alignment is straddling (type-I).*

5.3.3 Carbon impurities

As mentioned in the introduction, the interest for C impurities is inspired by nonvacuum synthesis techniques for CIGS, such as printing of an ink containing precursor nanoparticles. The nonvacuum methods have the clear advantage of a reduced loss of material, compared to losses of 20 to 50 % for vacuum processes. Additionaly, the required energy input is much smaller in nonvacuum methods. In these methods, C is present as part of organic solvents for the nanoparticles. The electronic configuration of C is [He] $\underline{2s^2 2p^2}$, where the electrons in the underlined orbitals are treated as a valence electrons in the PAW potential. We will study three types of C impurities: (i) C_{Cu} (C substitutional on a Cu site), (ii) $C_{In/Ga}$ (C substitutional on an In/Ga site) and (iii) C_i (C interstitial).

5.3.3.1 Substitutional carbon on copper site

The C substitutional on a Cu site, C_{Cu}, is a potential impurity, especially in growth conditions with Cu-deficiency. The C_{Cu} defect in CIS is shown in Figure 5.10. As for V_{Cu} and Na_{Cu} defects, the distortion of the lattice surrounding the defect can be measured as the change in interatomic distance as Cu is replaced by C. In the discussion of C impurities we will each time include the limiting compounds, CIS and CGS. In Table 5.8, the interatomic distances can be found. We list the results for all calculated charge states. A wide range of $q = -2, -1, 0, +1, +2, +3$ is chosen, as C can formally carry oxidation varying from -4 to +4. It turns out that the C-Se distance is smaller than the unperturbed Cu-Se distance for all charge states. The maximal C-Se distance is found for $q = 0$ in both the CIS and CGS host. The C-Se distance decreases for both positive and negative charge states.

The formation energies in CIS and CGS, shown in Figure 5.11, indicate that the C_{Cu} defect prefers to donate electrons. For small Fermi levels, the $q = +3$ state is favored. This is not surprising, since C has 3 valence electrons in excess compared Cu. There is a direct transition from the $q = +3$ to the $q = +1$ state within the band gap, at 0.805 eV and 0.922 eV for respectively CIS and CGS, as can be found in Table 5.9. A transition $+1/0$ occurs far within the conduction bands. This means that, given the Fermi level is positioned sufficiently high, the C_{Cu} can in principle act as a *shallow donor* in both CIS and CGS. This may be of technological interest to n-type doping for CIGS p-n

homojunctions. However, two problems arise: first, as we have found in Section 5.3.1, the ubiquitous V_{Cu} defects pin the Fermi level far from the CBM. The reason is, as we have seen, the spontaneous creation of these defects, especially in compounds with a significant amount of Ga. The second problem is that the formation energy of the donor defect is high. At the CBM, it is 6.57 eV in CIS and 7.11 eV in CGS (under Cu-rich and C-rich conditions). This also means that C_{Cu} defects are no real threat to the p-type conductivity in a printed CIGS absorber layer. So, are there effective n-type dopants for CIGS? Zunger et al. have found theoretically that Cd_{Cu} is a shallow donor in CIS and Mg_{Cu} is a shallow donor in CGS [23]. Yet, the formation energy is not sufficiently low to overcome the compensation by V_{Cu} defects. As such, Zunger et al. put forward the idea of focussing on doping under nonequilibrium conditions.

Compound	q	d^d_{C-Se}(Å)
CIS	+3	2.043
	+2	2.177
	+1	2.307
	0	2.314
	-1	2.300
	-2	2.273
CGS	+3	2.058
	+2	2.177
	+1	2.316
	0	2.349
	-1	2.340
	-2	2.270

TABLE 5.8: *Interatomic distances d^d_{C-Se} in the lattice with C_{Cu} defect for several charge states, q. The unperturbed interatomic distances are d^u_{Cu-Se} = 2.456, 2.440 Å for respectively CIS and CGS.*

Compound	Transition	Energy (eV)
CIS	+3/+1	0.805
	+1/0	1.696
CGS	+3/+1	0.922
	+1/0	2.058

TABLE 5.9: *Relevant transition levels for a C_{Cu} defect w.r.t. the VBM.*

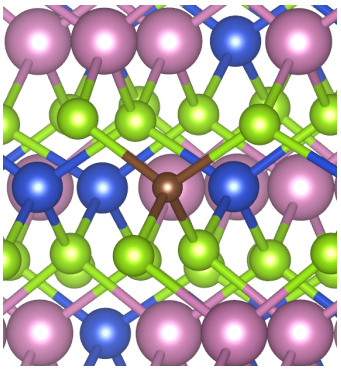

FIGURE 5.10: *The C substitutional (brown) on a Cu site and its relaxed environment in CIS, consisting of Cu (blue), In (pink) and Se (green).*

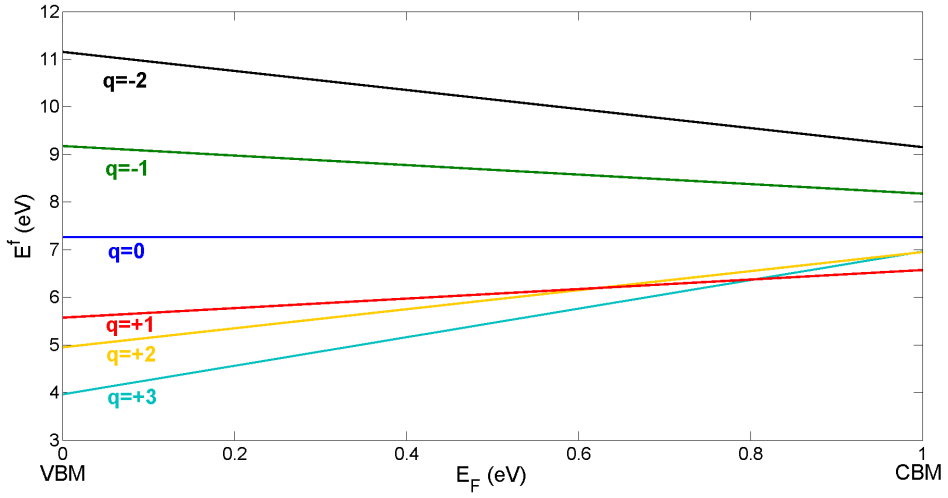

(a) CIS

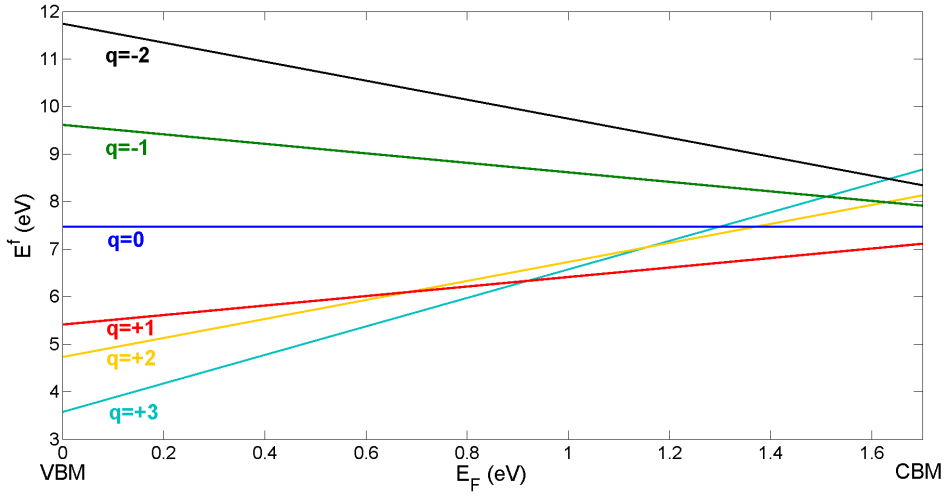

(b) CGS

FIGURE 5.11: *Formation energies E^f (eV) of the C_{Cu} defect in CIS and CGS as a function of the Fermi level E_F (eV) between the VBM and CBM.*

5.3.3.2 Substitutional carbon on indium or gallium site

Another potential defect is substitutional C on an In site (in CIS) or a Ga site (in CGS), as shown in Figure 5.12. These fall in the same category, because In and Ga occupy equivalent lattice sites in the chalcopyrite structure. Since the difference in valence electrons between C and In/Ga is only one, we have selected charge states $q = -2, -1, 0, +1, +2$. In Table 5.10 all C-Se interatomic distances, between C and the adjacent Se atoms are tabulated. They are to be compared to the In-Se and Ga-Se distances in the unperturbed CIGS lattice. Thus we observe that the interatomic distance decreases by an amount ranging from 0.305 (0.156) Å for $q = -2$ to 0.558 (0.385) Å for $q = +2$ in CIS (CGS).

The formation energy plots of the C_{In} defect in CIS and C_{Ga} in CGS are presented in Figure 5.13. The formation energy is calculated using In/Ga-rich and C-rich conditions. The ground state for the lower Fermi levels in the gap is $q = +1$. The interpretation is again clear: by donating one electron, C carries the same number of valence electrons as In and Ga. There is a transition to a different charge state within the gap for both host materials. At 0.743 eV (0.257 eV from the CBM) there is a +1/0 transition in CIS. Similarly, at 1.376 eV (0.344 eV from the CBM) a +1/-1 transition appears in CGS. This means that C_{In} and C_{Ga} give rise to really *deep donor* levels [3]. Hence, there is no direct contribution to the conductivity in CIGS from C_{In} and C_{Ga} defects. In general, a formation energy plot, with a donor ground state near the VBM or an acceptor ground state near the CBM can be considered a 'deep-level trap'. It does not contribute directly to the electrical conductivity, but if the formation energy is low, it may trap the free charge carriers originating from other, electrically active defects. Yet, as the formation energies are high, exceeding 5.50 eV (4.80 eV) in CIS (CGS), $C_{In/Ga}$ cannot be expected to significantly influence the electrical conductivity.

[3] Formally, C_{Ga} in CGS can be considered an extremely deep acceptor level as well, with a +1/-1 transition at 1.376 eV from the VBM.

Compound	q	$d^d_{\mathrm{C-Se}}$(Å)
CIS	+2	2.051
	+1	2.062
	0	2.147
	-1	2.301
	-2	2.304
CGS	+2	2.044
	+1	2.045
	0	2.142
	-1	2.272
	-2	2.273

TABLE 5.10: *Interatomic distances d^d_{C-Se} in the lattice with C_{In} and C_{Ga} defects for several charge states, q. The unperturbed interatomic distances are $d^u_{In-Se} = 2.609$ Å in CIS and $d^u_{Ga-Se} = 2.429$ Å in CGS.*

Compound	Transition	Energy (eV)
CIS	+2/+1	-0.213
	+1/0	0.743
	0/-1	1.031
CGS	+2/+1	0.014
	+1/-1	1.376
	-1/-2	2.294

TABLE 5.11: *Relevant transition levels for the C_{In} and C_{Ga} defects w.r.t. the VBM.*

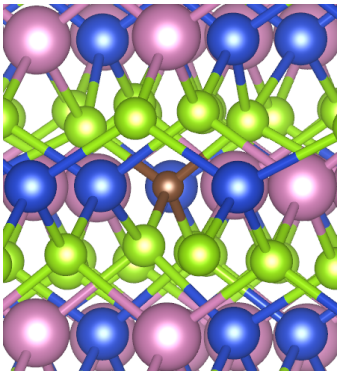

FIGURE 5.12: *The C substitutional (brown) on an In site and its relaxed environment in CIS, consisting of Cu (blue), In (pink) and Se (green).*

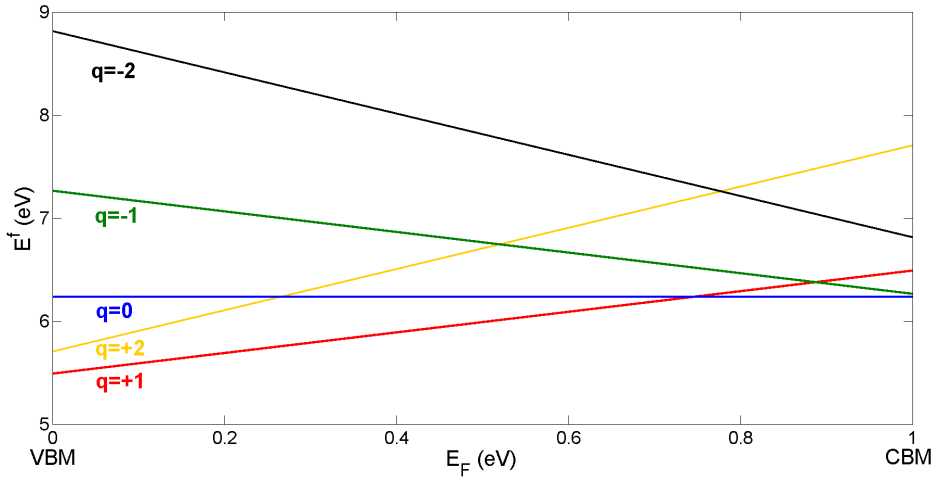

(a) CIS

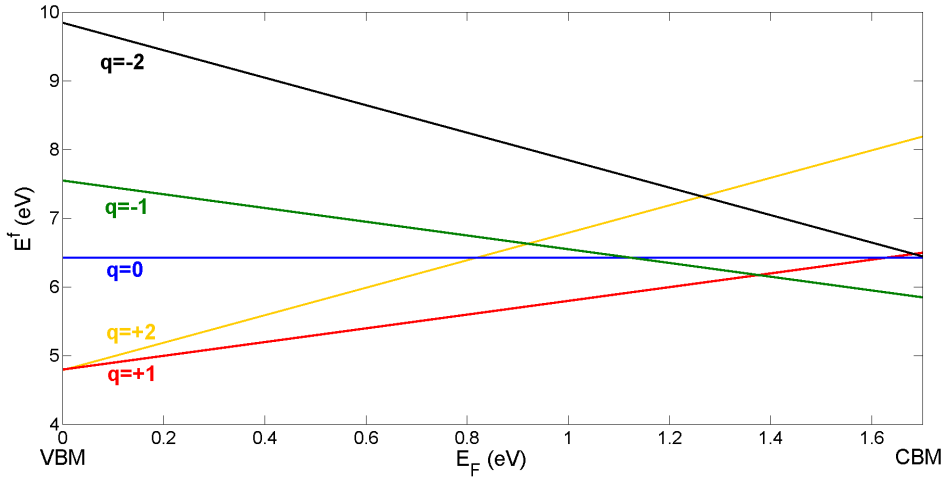

(b) CGS

FIGURE 5.13: *Formation energies E^f (eV) of the C_{In} and C_{Ga} defects in CIS and CGS as a function of the Fermi level E_F (eV) between the VBM and CBM.*

5.3.3.3 Interstitial carbon

The final C impurity we discuss is a C interstitial defect, C_i. The possibility of a C interstitial defect can be understood in terms of the atomic radii. Of course, the notion of an atomic radius is highly approximate, given the quantum mechanical nature of atoms. The atomic radius of C, 0.77 Å, is small compared to the atomic radii of the other atoms: Cu (1.28 Å), Ga (1.41 Å), In (1.66 Å) [4] [23]. The initial position of the interstitial is chosen, so the distance to all other atoms in the lattice is maximal. The relaxed lattice, with all force components below 0.05 eV/Å, is shown in case of CIS (with $q = 0$) in Figure 5.14. The distortion of the lattice can conveniently be measured in terms of the two nearest neighbor distances of the C interstitial, cfr. Figure 5.12. It turns out the nearest neighbors are usually Se and Cu in both CIS and CGS. For the charge acceptor states in CGS the second nearest neighbor is Ga instead.

The formation energies of the C interstitials in CIS and CGS using C-rich conditions are displayed in Figure 5.15. In CIS, there is a transition between the $q = +2$ and $q = 0$ states at 0.657 eV above the VBM (0.343 eV below the CBM). This means that the C_i acts as a very *deep donor*. In CGS, the ground state of C_i is donor-like for the lower range of E_F. There is a transition from $q = +2$ to $q = +1$ at 0.184 eV. Subsequently, at 0.458 eV the neutral state becomes the ground state. For the higher range of E_F in the gap the defect favors acceptor behavior. Transition levels are $\varepsilon(0/-1) = 1.015$ eV and $\varepsilon(-1/-2) = 1.666$ eV. Therefore, the C interstitial is both an extremely *deep donor and acceptor*. The C interstitial is a possible deep-level trap for acceptor levels in CIS and for both donor and acceptor levels in CGS. In the chalcopyrite materials, this is however not a significant problem, since the formation energy is high. For C_i, its minimal value within the band gap is 3.69 eV (3.97 eV) in CIS (CGS).

[4] The atomic radii of the metallic elements are defined as the radius of the ions in 12-coodinated metals, the atomic radius of C is defined as the radius of the atom in a tetrahedral covalent bond.

Compound	q	NN_1	NN_2	$d^d_{C-NN_1}$(Å)	$d^d_{C-NN_2}$(Å)
CIS	+2	Se	Cu	1.733	1.968
	+1	Se	Cu	1.769	1.964
	0	Se	Cu	1.811	1.859
	-1	Se	Cu	1.874	2.273
	-2	Se	Cu	1.905	2.200
CGS	+2	Se	Cu	1.923	1.993
	+1	Se	Cu	1.763	1.984
	0	Se	Cu	1.807	1.858
	-1	Se	Ga	1.839	1.907
	-2	Se	Ga	1.876	1.869

TABLE 5.12: *Interatomic distances between C and its two nearest neighbors, NN_1 and NN_2, in the lattice with C_i defect for several charge states, q.*

Compound	Transition	Energy (eV)
CIS	+2/0	0.657
	0/-2	1.513
CGS	+2/+1	0.184
	+1/0	0.458
	0/-1	1.015
	-1/-2	1.666

TABLE 5.13: *Relevant transition levels of the C_i defect w.r.t. the VBM.*

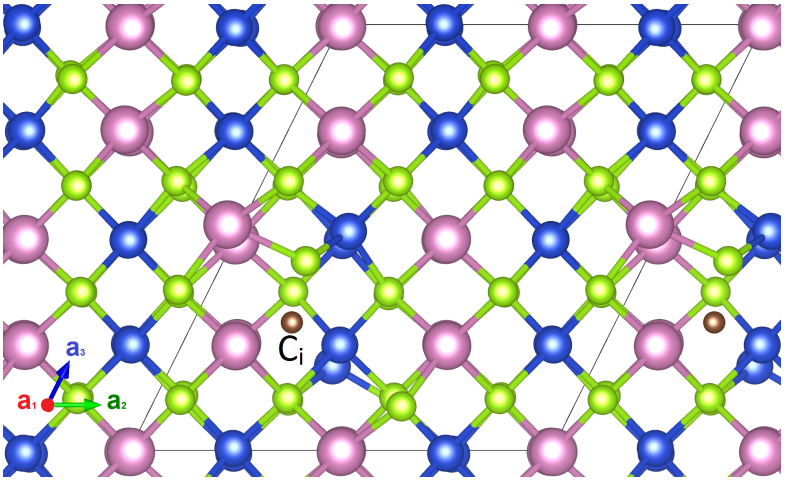

FIGURE 5.14: *The lattice distortion in CIS due to a C_i defect. The $2 \times 2 \times 2$ supercell is indicated. The position of the interstitial in terms of $\boldsymbol{a}_1 = (2a, 0, 0)$, $\boldsymbol{a}_2 = (0, 2a, 0)$ and $\boldsymbol{a}_3 = (a, a, c)$, the primitive lattice vectors that span the $2 \times 2 \times 2$ supercell, is $\sim(0.97, 0.23, 0.30)$.*

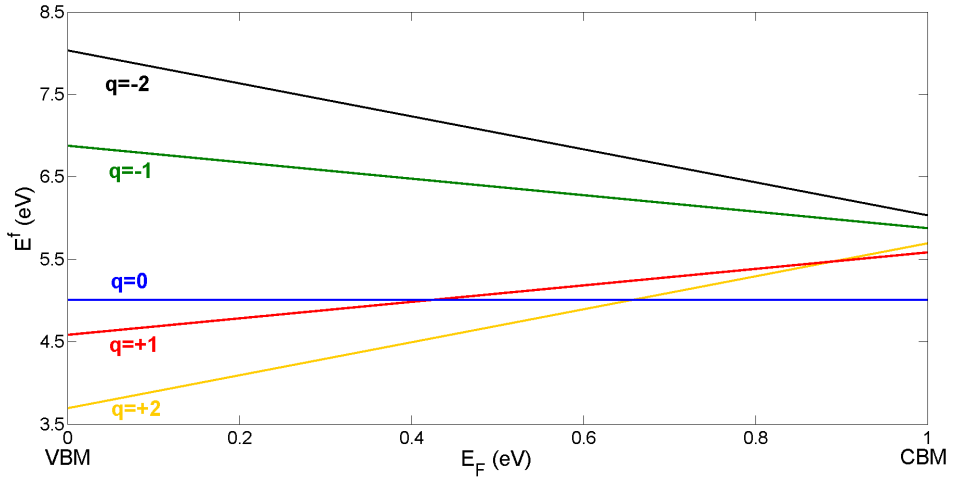

(a) CIS

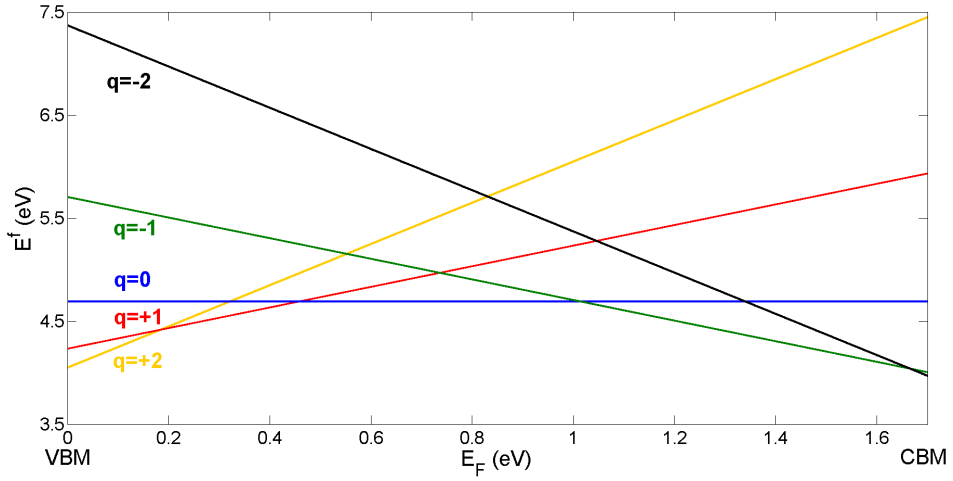

(b) CGS

FIGURE 5.15: *Formation energies E^f (eV) of the C_i defect in CIS and CGS as a function of the Fermi level E_F (eV) between the VBM and CBM.*

5.3.3.4 Chemical potential of carbon

Central in our discussion of C doping is the chemical potential of C. We have adopted C-rich conditions, using the chemical potential of the elemental solid, in this case graphite. The resulting chemical potential of C is $\mu_C = -11.31$ eV. So, owing to the stability of graphite, transferring C atoms from the reservoir to the system is quite hard. Since C atoms are added to the system, a term of +11.31 eV is included in the formation energy following Equation 5.1. This is the main reason the formation energy of all C impurity defects turns out to be rather high.

One may wonder whether it is correct to suppose a reservoir of graphite. In reality, the C atoms are part of organic molecules. Methanol is probably the most simple organic solvent used in the printing method [12]. It can readily be studied using the hybrid functional, enclosing it in a 'box', a supercell with an edge of 30 Å that is otherwise empty. In order to calculate the formation energy of methanol, CH_3OH, the total energy of graphite is to be taken into account. The total energies of the O_2 and H_2 molecules have to be included as well. For this computation, O_2 and H_2 are enclosed in boxes with edges measuring 30 Å. The total energy of O_2 is obtained in a spin-polarized calculation, since the triplet state with two unpaired electrons is the ground state. The theoretical result for the formation energy of methanol is thus:

$$\begin{aligned} \Delta H^f(CH_3OH) &= E_{tot}(CH_3OH) - \frac{E_{tot}(\text{graphite})}{\text{atom}} - \frac{1}{2}E_{tot}(O_2) - 2E_{tot}(H_2) \\ &= -2.71 \text{ eV} \ . \end{aligned} \tag{5.9}$$

An experimentally obtained value of the heat of formation is -238.4 kJ/mol [81]. This is equivalent to -2.47 eV per CH_3OH molecule, yielding a good agreement with the theoretical value. The growth conditions are not specified for the experimental value. Stability of the methanol molecule requires that $\Delta\mu_C \leq 0$. Consequently, the chemical potential μ_C ranges from $\mu_C^{graphite}$ in C-rich conditions to $\mu_C^{graphite} - 2.71$ eV in C-poor conditions. We find that the formation energies can shift upwards with +2.71 eV at most (in C-poor conditions, which are not plausible). We can conclude that a reservoir containing organic molecules (an analogous reasoning can be applied to other solvents) leads to an additional increase of the C impurity formation energy.

Presenting the results for the formation energies, we have assumed Cu-rich conditions for C_{Cu} and In/Ga-rich conditions in case of $C_{In/Ga}$. A correction for ~ 10 % Cu-deficiency leads to a slight downwards shift of the defect formation energies. We stress that this shift is uniform, meaning it is equal for all charge states of the same defect. Therefore, the transition levels and thus the conclusion regarding the type of conductivity are not altered. The likelihood of the formation of the defect is determined by the chemical potentials of the atoms that are exchanged with the reservoir. The formation of all C defects that we have studied, C_{Cu}, $C_{In/Ga}$ and C_i have high formation energies amounting to respectively $>\sim 3.5$ eV, $>\sim 5.0$ eV and $>\sim 3.5$ eV near the VBM and $>\sim 6.5$ eV, $>\sim 6.0$ eV and $>\sim 4.0$ eV near the CBM. This leads to the overall conclusion that the formation of C defects is unlikely. Hence, it can be expected that C is expelled outside of CIGS, to the grain boundaries or outside of the absorber layer. This conclusion has been supported in private communication with S. Siebentritt, professor in physics at the University of Luxembourg and specialised in solar cells based on chalcopyrites. Prof. Siebentritt has confirmed that in nonvacuum synthesis methods for CIGS, a layer of C is formed outside of the absorber layer.

Conclusion and outlook

Cu(In,Ga)Se_2 (CIGS) is an alloy of the *chalcopyrite* materials $CuInSe_2$ (CIS) and $CuGaSe_2$ (CGS) with body-centered tetragonal space group $I\bar{4}2d$ (No. 122). It is a direct band gap semiconductor with an absorption coefficient that exceeds that of crystalline Si by approximately 100 times. This is why CIGS is used as the absorber material in *thin film photovoltaic cells*, possibly on a flexible substrate. To date, *polycrystalline CIGS*-based cells hold the record efficiency in the category of thin film cells.

We have performed a first-principles study of CIGS, using *density functional theory* (DFT), in which we try to improve on previous results by means of a *hybrid functional*, more specifically the Heyd-Scuseria-Ernzerhof (HSE) functional. This type of functional, containing an amount of Hartree-Fock exchange interaction, helps to overcome the band gap problem in DFT. Indeed, band gaps of CIGS obtained using a standard DFT functional are close to zero, whereas the HSE functional yields values that are in good agreement with experiment. The equilibrium structure of compounds with an intermediate Ga-to-In ratio, viz. 25, 50 and 75 % as implemented in a 16-atom supercell (i.e. twice the primitive cell), are found to deviate slightly from the chalcopyrite structure. This results in a lowering of the symmetry. Nevertheless, the lattice parameters generally comply with Vegard's law and there is no tendency for phase segregation of CIS and CGS at room temperature.

Regarding the chemical bonds in CIGS, the projected DOS shows hybridization between Cu-3d and Se-4p states in the upper valence bands, leading to p-d repulsion. Furthermore, Bader charge analysis reveals that the chemical bonds bond are covalent rather than ionic. We have also calculated additional properties from the band structure. First, the band masses of charge carriers in the upper valence and lower conduction bands are well below the free electron mass and have limited anisotropy. Secondly, the onset of the imaginary part of the dielectric function confirms that the band gap in

CIGS is direct.

Next, we have studied the mutual band alignment of CIGS compounds with varying Ga-to-In ratio. Two main methods are compared, viz. (i) based on the *branch-point energy* (BPE) and (ii) based on a *slab calculation*. The main advantage of the former is that the BPE can be calculated from the bulk band structure. On the other hand, the slab calculation gives an absolute reference for the alignment, the vacuum level. The resulting alignment is of the *straddling* type, in which the offset of the conduction bands is considerably larger than that of the valence bands. This is natural, since the lower conduction bands predominantly consist of Ga-4s and In-5s states and they are thus directly affected by a change of the Ga-to-In ratio. The valence bands offsets of CIS and CGS, obtained from the BPE (calculated as a BZ average of the band structure) and from a slab calculation, differ by less than 0.1 eV. It demonstrates that the BPE is a useful concept for the alignment of band structures.

We have subsequently calculated the formation energy of a series of *point defects* in CIGS, implemented in a 64-atom supercell. We have demonstrated, by a comparison with results obtained in a 216-atom supercell, that the 64-atom supercell is sufficient for accurate calculations. To begin with, our computations show that Cu vacancies act as shallow acceptors, thus accounting for the p-type conductivity of CIGS absorbers. We have found that they are likely to be formed, especially under Cu-deficient growth conditions. Moreover, if the Fermi level is located near the CBM, Cu vacancies are deep-level traps that - due to their prevalence - prevent n-type conductivity, in particular in compounds with a high Ga-to-In ratio. Next, we have contributed to the open question of why Na doping is beneficial to the cell performance. A Na substitutional on a Cu site turns out to form spontaneously, yet it is not electrically active. This is why we have considered the formation of $NaInSe_2$ (NIS) at the grain boundaries. NIS has long been assumed to produce a *hole barrier*, resulting in type-inversion of the grain boundaries and reduced recombination. We find, however, that the alignment of NIS (at the grain boundary) and CIS (in the grain interior) is *straddling*. Consequently, it is not an effective hole barrier, but a barrier for *all* charge carriers. Based on the BPE, we have instead proposed that type inversion in CIGS may occur due to donor-like *surface states*. Provided NIS is not present in excess at the grain boundaries, the open circuit voltage of the cell may benefit from its large band gap.

Ultimately, we have studied C impurities, a quite novel topic, related to new nonvacuum growth methods based on nanoparticle inks. We have considered several

substitutionals and also an interstitial defect. We found that a C substitutional on a Cu site is a *shallow donor*, while C substitutionals on In/Ga sites lead to very *deep donor* levels. Interstitial C turns out to be both a really *deep donor and acceptor*. Moreover, all C impurities act as deep-level traps: the substitutionals for acceptor levels and the interstitial defect for levels of both types. They can thus *in principle* harm the p-type conductivity in CIGS. Yet, we observe that the formation energy of C defects is very high, even in C-rich conditions. Therefore, C defects are not likely to be formed in CIGS. We expect that C is *expelled* from the absorber in nonvacuum growth methods.

In this thesis, we have strived to present a thorough description of the CIGS absorber on an atomic level, in the framework of DFT. Of course, modelling a real (photovoltaic) device is complex and improvements can always be made. We wish to point out a few examples as an outlook. First, since DFT is formulated as a ground state theory, it cannot be used to describe *excitonic interaction*. Including this interaction of a bound electron-hole pair leads to a more accurate account of the optical properties. It can be realized in terms of the *Bethe-Salpeter equation* (e.g. within the GW approximation). Secondly, we have discussed the *grain boundaries* in polycrystalline CIGS on occasion, mainly in relation to the notion of a hole barrier. However, we have not modelled the grain boundaries directly. This is not an easy task, since there are many possible orientations and compositions that should be considered and since a large supercell is required. Thirdly, our defect calculations can be extended to *combinations of defects* (e.g. $2V_{Cu}^{-}$+In_{Cu}^{2+}), for which at least a 216-atom supercell is needed. Finally, the *kesterite* materials $Cu_2ZnSn(S,Se)_4$ (CZTS, CZTSe) are recently gaining technological interest. Currently, devices with kesterite absorber layers have not quite reached the efficiency of CIGS-based cells. First-principles calculations can play a role in the development of these devices.

Conclusie en vooruitzicht

$Cu(In,Ga)Se_2$ (CIGS) is een legering van $CuInSe_2$ (CIS) en $CuGaSe_2$ (CGS), chalcopyriet-materialen met ruimtegecentreerde tetragonale ruimtegroep $I\bar{4}2d$ (Nr. 122). CIGS is een halfgeleider met een directe bandkloof en als gevolg een absorptiecoëfficient, die ongeveer 100 keer groter is dan die van kristallijn Si. Dit verklaart waarom CIGS gebruikt wordt als absorptiemateriaal in *dunne-film fotovoltaïsche cellen*, eventueel op een flexibel substraat. Cellen met een absorptielaag van *polykristallijn CIGS* hebben hebben de hoogste efficiëntie binnen de categorie van dunne-film cellen.

We hebben een ab-initio studie van CIGS uitgevoerd, gebruik makend van *dichtheidsfunctionaaltheorie* (DFT). Hierbij hebben we getracht om met behulp van een hybride functionaal, meer bepaald de Heyd-Scuseria-Ernzerhof (HSE) functionaal, vooruitgang te boeken t.o.v. resultaten in de wetenschappelijke literatuur. Dit type van functionaal, dat een hoeveelheid Hartree-Fock exchange-interactie in rekening brengt, biedt een oplossing voor het bandkloofprobleem in DFT. De bandkloven van CIGS materialen beschreven m.b.v. een standaard-functionaal zijn ongeveer nul, maar m.b.v. van een hybride functionaal komen de bandkloven beter overeen met experimentele waarden. De evenwichtstructuur van CIGS met een intermediaire Ga-In verhouding, namelijk 25, 50 and 75 %, geïmplementeerd in een supercel van 16 atomen (d.i. tweemaal de primitieve cel), blijkt licht af te wijken van de chalcopyriet-structuur. Het gevolg is een verlaging van de symmetrie. Toch voldoen de roosterparameters in het algemeen aan de regel van Vegard en treedt er geen fasesegregatie op bij kamertemperatuur.

Op het vlak van de chemische binding, volgt uit de geprojecteerde DOS dat de Cu-3d en Se-4p toestanden in de bovenste valentiebanden gehybridiseerd zijn, wat leidt tot p-d repulsie. Verder leert een Bader-ladingsanalyse ons dat de bindingen meer een covalent dan een ionisch karakter hebben. We hebben ook enkele afgeleide grootheden

van de bandenstructuur berekend. Ten eerste, blijken de bandmassa's van de ladingsdragers in de bovenste valentie- en onderste conductiebanden systematisch kleiner te zijn dan de massa van het vrije elektron. Ze vertonen ook slechts een beperkte anisotropie. Ten tweede, wordt door de drempelwaarde van het imaginaire deel van de diëlektrische functie bevestigd dat de bandkloof van CIGS direct is.

Vervolgens hebben we de alignering onderzocht van de bandenstructuren van CIGS met een variabele Ga-In verhouding. In hoofdzaak worden twee methoden voor alignering vergeleken, namelijk (i) m.b.v. de *'branch-point' energie* (BPE) en (ii) m.b.v. de potentiaal in een *'slab'* (plaat). Het feit dat de BPE berekend kan worden uit louter de bandenstructuur in bulk, is het belangrijkste voordeel van de eerste methode. Langs de andere kant bevat een alignering m.b.v. een slab een absolute referentie, te weten het vacuüumniveau. Zo vinden we dat de alignering van CIGS van het 'straddling' (gespreide) type is. De stapgrootte tussen de conductieniveaus is veel groter dan die tussen de valentieniveaus. Dit kan als volgt begrepen worden. De onderste conductiebanden bestaan hoofdzakelijk uit Ga-4s en In-5s toestanden en worden dus rechtstreeks beïnvloed door de Ga-In verhouding. De stapgroottes tussen de valentieniveaus van CIS en CGS, bekomen met enerzijds de BPE-methode (berekend als gemiddelde van de bandenstructuur in de 1^{e} BZ) en anderzijds met de slab-methode, verschillen minder dan 0,1 eV. Dit toont in het geval van CIGS aan dat de BPE-methode bruikbaar is om bandenstructuren te aligneren.

We hebben ook een studie gemaakt van de vormingsenergie van een reeks van *puntdefecten* in CIGS, geïmplementeerd in een supercel van 64 atomen. We hebben gezien dat dit formaat van supercel volstaat, door te vergelijken met berekeningen die gebruik maken van een supercel van 216 atomen. Om te beginnen, tonen onze berekeningen dat Cu-vacatures functioneren als ondiepe acceptoren. Dit verklaart de p-type geleiding van CIGS absorptiematerialen. We vinden ook dat Cu-vacatures gevormd kunnen worden, in het bijzonder bij Cu-arme groeicondities. Bovendien kunnen de Cu-vacatures elektronen gedoneerd door andere defecten invangen, als het Fermi-niveau nabij het CBM ligt. Op die manier werken ze n-type geleiding tegen, vooral in CIGS die meer Ga dan In bevatten. Verder hebben we Na-onzuiverheden in CIGS beschouwd. Men weet uit experimenten dat deze een gunstig effect hebben op de efficiëntie van de fotovoltaïsche cellen, maar het mechanisme hierachter is niet duidelijk gekend. Uit onze berekeningen volgt dat een Cu→Na substitutioneel defect spontaan vormt, maar niet elektrisch actief is. Daarom hebben ook we vorming van $NaInSe_2$ (NIS) aan de korrelgrenzen bestudeerd. Het werd

verondersteld dat dit resulteert in een *barrière voor gaten*, die zorgt voor type-inversie van de korrelgrenzen en verminderde recombinatie. Wij hebben echter aangetoond dat de alignering van NIS (aan de korrelgrenzen) en CIS (in de korrels) van het *'straddling'* type is. Daaruit blijkt dat NIS geen effectieve barrière voor gaten vormt, maar een barrière voor *alle* ladingsdragers. Op basis van de BPE stellen we voor dat type-inversie in CIGS eerder een gevolg is van donor-achtige *oppervlaktetoestanden*. NIS zou - indien het niet in hoge mate aanwezig is aan de korrelgrenzen - door zijn grote bandkloof wel een gunstig effect kunnen hebben op de open-kring spanning van de cel.

Ten slotte hebben we C-onzuiverheden in CIGS bestudeerd. Dit onderwerp is vrijwel onbesproken in de wetenschappelijke literatuur, maar wel van belang voor nieuwe groeitechnieken die gebruik maken van een inkt van nanodeeltjes en geen vacuüm behoeven. We hebben verscheidene substitutionele defecten en ook een interstitieel defect onderzocht. We vonden dat het Cu→C substitutioneel defect een *ondiepe donor* is, terwijl het In/Ga→C defect leidt tot erg *diepe donor* niveaus. Interstitieel C blijkt een heel erg *diepe donor en acceptor* te zijn. Daarenboven kunnen C-defecten ladingen afkomstig van andere defecten invangen. Substitutionele C-defecten kunnen gaten invangen en interstitiële C-defecten beide ladingsdragers. Zo kunnen ze *in principe* de p-type geleiding in CIGS tenietdoen. We merken echter dat de vormingsenergie van alle C-defecten heel hoog is, zelfs bij C-rijke groeicondities. Daardoor komen C-defecten niet eenvoudig tot stand en kunnen we veronderstellen dat C uit de absorptielaag gestoten wordt in de nieuwe groeitechnieken.

We hebben ons in deze thesis tot doel gesteld een grondige beschrijving van CIGS absorptiematerialen te geven. Meer bepaald situeert deze beschrijving zich op een atomair niveau en wordt gebruik gemaakt van DFT. Natuurlijk is de modellering van een realistische fotovoltaïsche cel complex en kunnen er dus steeds verbeteringen worden aangebracht. We wensen enkele voorbeelden aan te stippen bij wijze van vooruitzicht. Ten eerste kunnen we in DFT geen *exciton-interactie* behandelen, aangezien DFT geformuleerd is voor grondtoestanden. Indien deze interactie in rekening wordt gebracht, kunnen de optische eigenschappen nauwkeuriger beschreven worden. Dit kan men verwezenlijken via de *Bethe-Salpeter vergelijking* (eventueel in de GW-benadering). Ten tweede hebben we de *korrelgrenzen* van polykristallijn CIGS nu en dan besproken, vooral in verband met de barrière voor gaten. We hebbben de korrelgrenzen echter niet rechtstreeks gemodelleerd. Dit is een complexe taak, aangezien er vele mogelijke oriëntaties

en samenstellingen bestaan en een grote supercel vereist is. Ten derde kunnen we onze defectberekeningen uitbreiden naar *combinaties van defecten* (bv. $2V_{Cu}^{-}+In_{Cu}^{2+}$), waarvoor een supercel van ten minste 216 atomen nodig is. Tot slot zijn *kesteriet*-materialen $Cu_2ZnSn(S,Se)_4$ (CZTS, CZTSe) recent technologische belangstelling aan het winnen. Heden hebben fotovoltaïsche cellen die kesterieten als absorbtiemateriaal bevatten helemaal nog niet de efficiëntie van CIGS-cellen kunnen evenaren. Ab-initio berekeningen kunnen een rol spelen in de verdere ontwikkeling van deze materialen.

Bibliography

[1] C. Camus. Spray ILGAR growth and Raman spectroscopy of $CuInSe_2$ thin films. *Doctoral dissertation, Freie Universität Berlin*, pages 1372–1377, 2008. URL http://www.diss.fu-berlin.de/diss/servlets/MCRFileNodeServlet/FUDISS_derivate_000000004628/.

[2] H. G. Grimm and A. Sommerfeld. Ueber den Zusammenhang des Abschlusses der Elektronengruppen im Atom mit den chemischen Valenzzahlen. *Zeitschrift für Physik*, 36:36–59, 1926.

[3] J. E. Jaffe and A. Zunger. Electronic structure of the ternary chalcopyrite semiconductors $CuAlS_2$, $CuGaS_2$, $CuInS_2$, $CuAlSe_2$, $CuGaSe_2$, and $CuInSe_2$. *Physical Review B*, 28(10):5822–5847, November 1983.

[4] S. J. Fonash. Solar cell device physics. *Elsevier Academic Press*, 2010.

[5] M. A. Green. Potential for low dimensional structures in photovoltaics. *Elsevier Materials Science and Engineering B*, 74:118–124, 2000.

[6] A. Luque and S. Hegedus. Handbook of photovoltaic science and engineering. *John Wiley & Sons*, 2011.

[7] W. Shockley and H. J. Queisser. Handbook of photovoltaic science and engineering. *Journal of Applied Physics*, 32(3):510–519, March 1961.

[8] U. P. Singh and S. P. Patra. Progress in polycrystalline thin-film $Cu(In,Ga)Se_2$ solar cells. *International Journal of Photoenergy*, June 2010.

[9] J. Poortmans and V. Arkhipov. Thin film solar cells fabrication, characterization and applications. *John Wiley & Sons*, 2010.

[10] S. Wagner et al. $CuInSe_2$/CdS heterojunction photovoltaic detectors. *Applied Physics Letters*, 25(8):434–435, 1974.

[11] A. N. Tiwari et al. Highly efficient Cu(In,Ga)Se_2 solar cells grown on flexible polymer films. *Nature Materials*, 10:857–861, September 2011.

[12] S. R. Kodigala. Thin films and nanostructures: Cu(In,Ga)Se_2 based thin film solar cells. *Academic Press*, 35, 2010.

[13] M. J. Romero et al. A comparative study of the defect point physics and luminescence of the Kesterites Cu_2ZnSnS_4 and $Cu_2ZnSnSe_4$ and Chalcopyrite Cu(In,Ga)Se_2. *Conference paper presented at the 2012 IEEE Photovoltaic Specialists Conference, Austin (Texas)*, June 2012.

[14] C. Persson and A. Zunger. Anomalous grain boundary physics in polycrystalline $CuInSe_2$: the existence of a hole barrier. *Physical Review Letters*, 91(26), December 2003.

[15] C.-S. Jiang et al. How grain boundaries in Cu(In,Ga)Se_2 thin films are charged: Revisit. *Applied Physics Letters*, 101(3), July 2012.

[16] U. P. Singh and S. P. Patra. Progress in polycrystalline thin-film Cu(In,Ga)Se_2 solar cells. *International Journal of Photoenergy*, June 2010.

[17] A. N. Tiwari et al. Non-vacuum methods for formation of Cu(In,Ga)$(Se,S)_2$ thin film photovoltaic absorbers. *Progress in Photovoltaics: Research and Applications*, 18:434–452, September 2009.

[18] T. Gödecke, T. Haalboom, and F. Ernst. Phase equilibria of Cu-In-Se . *Zeitschrift für Metallkunde*, 91(8):622–634, September 2000.

[19] I. L. Repins et al. Device characteristics of a 17.1 % efficient solar cell deposited by a non-vacuum printing method on flexible foil. *Photovoltaic Specialists Conference, IEEE*, June 2012.

[20] B. Falabretti and J. Robertson. Electronic structures and doping of SnO_2, $CuAlO_2$ and $CuInO_2$. *Journal of Applied Physics*, 102, December 2007.

[21] A. Schleife et al. Branch-point energies and band discontinuities of III-nitrides and III-II-oxides from quasiparticle band-structure calculations. *Applied Physics Letters*, 94, January 2009.

[22] S. B. Zhang, S.-H. Wei, A. Zunger, and H. Katayama-Yoshida. Defect physics of the $CuInSe_2$ chalcopyrite semiconductor. *Physical Review B*, 57(16):9642–9656, April 1997.

[23] Y.-J. Zhao, C. Persson, S. Lany, and A. Zunger. n-type doping of $CuInSe_2$ and $CuGaSe_2$. *Physical Review B*, 72, July 2005.

[24] S.-H. Wei, S. B. Zhang, and A. Zunger. Effects of Na on the electrical and structural properties of $CuInSe_2$. *Journal of Applied Physics*, 85(10):7214–7218, May 1999.

[25] M. Springborg. Methods of electronic structure calculations. *John Wiley & Sons*, 2000.

[26] H. Peelaers. An ab initio study of the electronic and dynamical properties of Si, Ge and Si/Ge nanowires. *Doctorial dissertation, University of Antwerp*, 2009.

[27] O. Leenaerts. An ab initio study of the adsorption of atoms and molecules graphene. *Doctorial dissertation, University of Antwerp*, 2010.

[28] S. Vercauteren. Ab initio studie van waterstof onzuiverheden in zink oxide. *Master's dissertation, University of Antwerp*, 2011.

[29] H. Dixit. First-principles electronic structure calculations of transparent conducting oxide materials. *Doctorial dissertation, University of Antwerp*, 2012.

[30] P. Hohenberg and W. Kohn. Inhomogeneous electron gas. *Physical Review*, 136 (3B):864–871, November 1964.

[31] W. Kohn and L. J. Sham. Inhomogeneous electron gas. *Physical Review*, 140(4A): 1133–1138, November 1965.

[32] D. M. Ceperley and B. J. Alder. Ground state of the electron gas by a stochastic method. *Physical Review Letters*, 45(7):566–569, August 1980.

[33] J. P. Perdew, K. Burke, and M. Ernzerhof. Generalized Gradient Approximation made simple. *Physical Review Letters*, 77(18):3865–3868, October 1996.

[34] L. J. Sham and L. Schlüter. Density-functional theory of the energy gap. *Physical Review Letters*, 51(20):1888–1891, November 1983.

[35] W. G. Aulbur, L. Jönsson, and J. W. Wilkins. Quasiparticle calculations in solids. *Elsevier, Solid State Physics*, 54, 1999.

[36] J. C. Slater. A simplification of the Hartree-Fock method. *Physical Review*, 81(3): 385–390, February 1951.

[37] A. D. Becke. A new mixing of Hartree-Fock and local density-functional theories. *Journal of Chemical Physics*, 98(2):1372–1377, October 1992.

[38] J. Heyd, G. E. Scuseria, and M. Ernzerhof. Hybrid functionals based on a screened Coulomb potential. *Journal of Chemical Physics*, 118(18):8207–8215, February 2003.

[39] G. Kresse and J. Furthmüller. Efficiency of ab-initio total energy calculations for metals and semiconductors using a plane-wave basis set. *Computational Materials Science*, 6:15–20, March 1996.

[40] H. J. Monkhorst and J. D. Pack. Special points for brillouin-zone integration. *Physical Review B*, 13(12):5188–5192, June 1976.

[41] P. E. Blöchl. Projector augmented-wave method. *Physical Review B*, 50(24):17953–17979, December 1994.

[42] G. Kresse, M. Marsman, and J. Furthmüller. Vasp the guide. *VASP manual*, April 2009. URL http://www.vasp.at/index.php/documentation.

[43] Gavin J. Pringle. Optimisation of VASP density functional theory (DFT)/Hartree-Fock (HF) hybrid functional code using mixed-mode parallelism. October 2012. URL http://www.hector.ac.uk/cse/distributedcse/reports/vasp02/vasp02.pdf.

[44] D. F. Shriver and P. W. Atkins. Inorganic Chemistry. *Oxford University Press*, 3, June 1999.

[45] B. Grzeta-Plenkovic et al. Crystal data for $AgGa_xIn_{1-x}Se_2$ and $CuGa_xIn_{1-x}Se_2$. *Journal of Applied Crystallography*, 13:311, 1980.

[46] M. Belhadj et al. Structural, electronic and optical calculations of $Cu(In,Ga)Se_2$ ternary chalcopyrites. *Physica Status Solidi B*, 241(11):2516–2528, 2004.

[47] Z.-H. Li et al. Molybdenum thin film deposited by in-line DC magnetron sputtering as a back contact for $Cu(In,Ga)Se_2$ solar cells. *Applied Surface Science*, 257(22): 9682–9688, 2011.

[48] C. D. R. Ludwig et al. Indium-Gallium segregation in Cu(In,Ga)Se_2: An ab initiobased Monte Carlo study. *Physical Review Letters*, 105:9682–9688, July 2010.

[49] S. Curtarolo and W. Setyawan. High-throughput electronic band structure calculations: Challenges and tools. *Computational Materials Science*, 49:299–312, 2010.

[50] T. Tinoco et al. Phase diagram and optical energy gaps for $CuIn_yGa_{1-y}Se_2$ alloys. *Physica Status Solidi A*, 124(2):247, March 1991.

[51] S.-H. Wei and A. Zunger. Band offsets and optical bowings of chalcopyrites and Zn-based II-VI alloys. *Journal of Applied Physics*, 78(6), June 1995.

[52] C. Kittel. Introduction to solid state physics. *John Wiley & Sons*, 8, 2005.

[53] C. Persson. Anisotropic hole-mass tensor of $CuIn_{1-x}Ga_x(S,Se)_2$: Presence of free carriers narrows the energy gap. *Applied Physics Letters*, 93, August 2008.

[54] J. C. Rife and R. N. Dexter. Optical properties of the chalcopyrite semiconductors $ZnGeP_2$, $ZnGeAs_2$, $CuGaS_2$, $CuAlS_2$, $CuInSe_2$, and $AgInSe_2$. *Physical Review B*, 16(10):4491–4500, November 1977.

[55] R. Bader et al. Virial field relationship for molecular charge distributions and the spatial partitioning of molecular properties. *Journal of Chemical Physics*, 56(7): 3320, 1972.

[56] L. Pauling. The nature of the chemical bond. *Cornell University Press*, 3, 1960.

[57] N. Ashcroft and N. Mermin. Solid state physics. *Harcourt College Publishers*, 1976.

[58] F. Wooten. Optical properties of solids. *Academic Press*, 1972.

[59] S.-H. Wei, S. B. Zhang, and A. Zunger. Effects of Ga addition to $CuInSe_2$ on its electronic, structural and defect properties. *Applied Physics Letters*, 72(24): 3199–3201, April 1998.

[60] M. I. Alonso et al. Optical functions and electronic structure of $CuInSe_2$, $CuGaSe_2$, $CuInS_2$ and $CuGaS_2$. *Physical Review B*, 63, January 2001.

[61] M. Prutton. Introduction to surface physics. *Oxford University Press*, 1994.

[62] J. Tersoff. Schottky barrier heights and the continuum of gap states. *Physical Review Letters*, 52(6):465–468, February 1984.

[63] J. Tersoff. Theory of semiconductor heterojunctions: the role of quantum dipoles. *Physical Review B*, 30(8):4874–4877, October 1984.

[64] R. E. Allen. Green's functions for surface physics. *Physical Review B*, 20(4):1454–1472, August 1979.

[65] D. Mourad et al. Determination of the valence band offset at cubic CdSe/ZnTe type II heterojunctions: A combined experimental and theoretical approach. *Cornell University Library (online)*. URL http://arxiv.org/pdf/1208.2188.pdf.

[66] F. Flores and C. Tejedor. Energy barriers and interface states at heterojunctions. *Journal of Physics C: Solid State Physics*, 12:731–749, 1979.

[67] P. Deák et al. Band lineup and charge carrier separation in mixed rutile-anatase systems. *The Journal of Physical Chemistry*, 115:3443–3446, February 2011.

[68] C. G. Van de Walle et al. Hybrid functional investigation of band gaps and band alignments for AlN, GaN, InN and IngaN. *The Journal of Chemical Physics*, 134, February 2011.

[69] W. Mönch. Semiconductor surfaces and interfaces. *Springer-Verlag*, 2002.

[70] Y.-J. Zhao, C. Persson, S. Lany, and A. Zunger. Why can $CuInSe_2$ be readily equilibrium-doped n-type but the wider-gap $CuInSe_2$ cannot? *Applied Physics Letters*, 85(24):5860–5862, December 2004.

[71] T. Maeda and T. Wada. First-principles calculations of defect formation energy in chalcopyrite-type $CuInSe_2$, $CuInSe_2$ and $CuAlSe_2$. *Journal of Physics and Chemistry of Solids*, 66:1924–1927, 2005.

[72] C. G. Van de Walle and J. Neugebauer. Universal alignment of hydrogen levels in semiconductors, insulators and solutions. *Letters to Nature*, 423:626–628, June 2003.

[73] S. B. Zhang and J. E. Northup. Chemical potential dependence of defect formation energies in GaAs: Application to Ga self-diffusion. *Physical Review Letters*, 67: 2339–2342, 1991.

[74] M. N. Amini et al. Hydrogen impurities and native defects in CdO. *Journal of Applied Physics*, 110, September 2011.

[75] H. Dixit et al. First-principles study of possible shallow donors in $ZnAl_2o_4$ spinel. *Physical Review B*, 87(17), May 2013.

[76] W. B. Pearson, P. Villars, and L. D. Calvert. Pearson's handbook of crystallographic data for intermetallic phases. *American Society for Metals*, 1985.

[77] A. S. Verma, S. Sharma, and V. K. Jindal. Inherent properties of ternary $A^N B^{2+N} C_2^{7-N}$ tetrahedral semiconductors. *International Journal of Modern Physics B*, 26(15), 2012.

[78] R. Saniz et al. A simplified approach to the band gap correction of defect formation energies: Al, Ga, and In-doped ZnO. *Journal of Physics and Chemistry of Solids*, 74:45–50, 2013.

[79] D. Rudmann. The effect of sodium on growth and properties of Cu(In,Ga)Se_2 thin films and solar cells . *Doctoral dissertation submitted to the Swiss Federal Institute of technology, Zürich*, 2004. URL http://e-collection.library.ethz.ch/eserv/eth:27376/eth-27376-02.pdf.

[80] R. Hoppe et al. Zur Kenntnis von $NaInS_2$ und $NaInSe_2$. *Zeitschrift für Anorganische and allgemeine Chemie*, 74:45–50, 2013.

[81] NIST. Methyl alcohol. *Webbook*. URL http://webbook.nist.gov/cgi/cbook.cgi?ID=C67561.